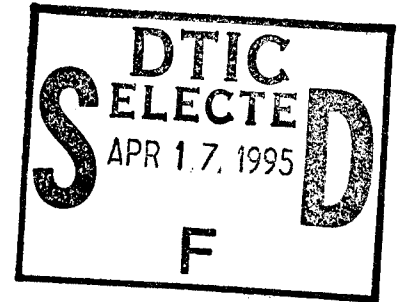# MATERIALS FOR ADAPTIVE STRUCTURAL ACOUSTIC CONTROL

Period February 1, 1994 to January 31, 1995

Annual Report

VOLUME IV

OFFICE OF NAVAL RESEARCH
Contract No.: N00014-92-J-1510

APPROVED FOR PUBLIC RELEASE — DISTRIBUTION UNLIMITED

L. Eric Cross

DTIC QUALITY INSPECTED 5

PENNSTATE

1 8 5 5

THE MATERIALS RESEARCH LABORATORY
UNIVERSITY PARK, PA

19950417 072

REPORT DOCUMENTATION PAGE

1. AGENCY USE ONLY (Leave blank)	2. REPORT DATE	3. REPORT TYPE AND DATES COVERED
	4/6/95	ANNUAL REPORT 02/1/94 TO 01/31/95

4. TITLE AND SUBTITLE

MATERIALS FOR ADAPTIVE STRUCTURAL ACOUSTIC CONTROL

5. FUNDING NUMBERS

6. AUTHOR(S)

L. ERIC CROSS

7. PERFORMING ORGANIZATION NAME(S) AND ADDRESS(ES)

MATERIALS RESEARCH LABORATORY
THE PENNSYLVANIA STATE UNIVERSITY
UNIVERSITY PARK, PA 16802

8. PERFORMING ORGANIZATION REPORT NUMBER

9. SPONSORING/MONITORING AGENCY NAME(S) AND ADDRESS(ES)

OFFICE OF NAVAL RESARCH
CODE 1513:NRJ
800 NORTH QUINCY STREET
ARLINGTON, VA 22217

GERALD T. SMITH
OFFICE OF NAVAL RESARCH RES. REP.
536 SOUTH CLARK STREET, RM 286
CHICAGO, ILLINOIS 60606-1588

10. SPONSORING/MONITORING AGENCY REPORT NUMBER

11. SUPPLEMENTARY NOTES

12a. DISTRIBUTION/AVAILABILITY STATEMENT

12b. DISTRIBUTION CODE

13. ABSTRACT (Maximum 200 words)

SEE FOLLOWING TWO PAGES

14. SUBJECT TERMS

15. NUMBER OF PAGES

16. PRICE CODE

17. SECURITY CLASSIFICATION OF REPORT	18. SECURITY CLASSIFICATION OF THIS PAGE	19. SECURITY CLASSIFICATION OF ABSTRACT	20. LIMITATION OF ABSTRACT

GENERAL INSTRUCTIONS FOR COMPLETING SF 298

The Report Documentation Page (RDP) is used in announcing and cataloging reports. It is important that this information be consistent with the rest of the report, particularly the cover and title page. Instructions for filling in each block of the form follow. It is important to *stay within the lines* to meet *optical scanning requirements*.

Block 1. Agency Use Only *(Leave blank)*.

Block 2. Report Date. Full publication date including day, month, and year, if available (e.g. 1 Jan 88). Must cite at least the year.

Block 3. Type of Report and Dates Covered. State whether report is interim, final, etc. If applicable, enter inclusive report dates (e.g. 10 Jun 87 - 30 Jun 88).

Block 4. Title and Subtitle. A title is taken from the part of the report that provides the most meaningful and complete information. When a report is prepared in more than one volume, repeat the primary title, add volume number, and include subtitle for the specific volume. On classified documents enter the title classification in parentheses.

Block 5. Funding Numbers. To include contract and grant numbers; may include program element number(s), project number(s), task number(s), and work unit number(s). Use the following labels:

C	- Contract	PR	- Project
G	- Grant	TA	- Task
PE	- Program Element	WU	- Work Unit Accession No.

Block 6. Author(s). Name(s) of person(s) responsible for writing the report, performing the research, or credited with the content of the report. If editor or compiler, this should follow the name(s).

Block 7. Performing Organization Name(s) and Address(es). Self-explanatory.

Block 8. Performing Organization Report Number. Enter the unique alphanumeric report number(s) assigned by the organization performing the report.

Block 9. Sponsoring/Monitoring Agency Name(s) and Address(es). Self-explanatory.

Block 10. Sponsoring/Monitoring Agency Report Number. *(If known)*

Block 11. Supplementary Notes. Enter information not included elsewhere such as: Prepared in cooperation with...; Trans. of...; To be published in.... When a report is revised, include a statement whether the new report supersedes or supplements the older report.

Block 12a. Distribution/Availability Statement. Denotes public availability or limitations. Cite any availability to the public. Enter additional limitations or special markings in all capitals (e.g. NOFORN, REL, ITAR).

DOD - See DoDD 5230.24, "Distribution Statements on Technical Documents."
DOE - See authorities.
NASA - See Handbook NHB 2200.2.
NTIS - Leave blank.

Block 12b. Distribution Code.

DOD - Leave blank.
DOE - Enter DOE distribution categories from the Standard Distribution for Unclassified Scientific and Technical Reports.
NASA - Leave blank.
NTIS - Leave blank.

Block 13. Abstract. Include a brief *(Maximum 200 words)* factual summary of the most significant information contained in the report.

Block 14. Subject Terms. Keywords or phrases identifying major subjects in the report.

Block 15. Number of Pages. Enter the total number of pages.

Block 16. Price Code. Enter appropriate price code *(NTIS only)*.

Blocks 17.-19. Security Classifications. Self-explanatory. Enter U.S. Security Classification in accordance with U.S. Security Regulations (i.e., UNCLASSIFIED). If form contains classified information, stamp classification on the top and bottom of the page.

Block 20. Limitation of Abstract. This block must be completed to assign a limitation to the abstract. Enter either UL (unlimited) or SAR (same as report). An entry in this block is necessary if the abstract is to be limited. If blank, the abstract is assumed to be unlimited.

ABSTRACT

The objectives of this ONR sponsored University Research Initiative (URI) entitled "Materials for Adaptive Structural Acoustic Control" concern both basic fundamental studies and highly applied development of the piezoelectric and electrostrictive ferroelectric ceramics which carry both the sensing and actuation functions for adaptive control. The report documents work over the third year of this five year program. For convenience and continuity, the activities are grouped under the headings" General Summary Papers, Materials Studies, Composite Sensors, Actuator Studies, Integration Issues, Processing Studies, Thin Film Ferroelectrics, and the Abstracts of graduating students on the program.

The first general papers illustrate the educational role undertaken by MRL faculty both in the basic understanding of ferroics, and in the philosophy of their application in 'smart' systems. It is interesting that through work pioneered on earlier ONR programs in MRL, it is now possible to measure both direct and converse electrostrictive response in simple solids, and to thus explore models to explain the signs and magnitudes of these striction constants. The relaxor ferroelectrics have been a topic of study for more than 30 years in the laboratory, but recent breakthroughs have revolutionized the level of understanding and opened a vista for further potential application of size (scale) effects in ferroics. Electrical control of shape memory has been achieved in a number of electro-ferroic solids, but full exploitation will need more complete understanding of both ferroelectric and ferroelastic:ferroelectric domain wall processes. Photostriction, the combination of photovoltaic and piezoelectric effects in ceramics promises an interesting range of new device possibilities.

In material studies, the elegant work on lanthanum modified lead titanate has now been fully written up, and the vital role of strain coupling in the onset of diffuse response underscored. New experimental methods have been applied to separating and measuring intrinsic and extrinsic components of response in PZT ceramics and to the measurement of microwave properties in these high K systems. Soft, intermediate, and hard modified lead zirconate and PZT composition have been under study for new and more interesting morphotropic phase boundaries which could be fabricated in single crystal form. Both optical birefringence and Raman studies are being used to explore domain and phase changes.

In sensing studies, the focus has been maintained upon flextensional (Moonie) structures and the enhanced performance which new end cap designs are affording. The polyvinylidene fluoride/trifluoethylene piezoelectrics are themselves an interesting composite system where the lower symmetry demands more complete characterization. The 1:3 rod and tube type composites have many performance advantages and trade-offs which will ensure wider scale application now that economical assembly techniques are at hand.

For actuation, the flextensional (Moonie) offers a number of advantages which merit further study. Both material and multilayer device related fatigue and destruction mechanisms are under study, and modes to control and alleviate microcracking and space change degradation are examined. More detailed studies of the photostriction effects and their control by doping effects in PZTs have also been accomplished.

Integration studies have continued to explore the components which must be co-processed in the smart material or adaptive assemblage. Examples are the thick film conductors in copper or silver/palladium, the 0:3 high density piezoelectric polymer composites and the filter functions required to eliminate cross talk in the wiring system.

Processing studies are essential to the fabrication of the very wide range of materials demanded by all elements of the program. Relaxor materials have formed the focus for many processing activities but more recently the needs for high strain actuation are refocusing interest on phase switching antiferroelectric:ferroelectric compositions in the high lead zirconate PLZTs and PSnZTs with mounting evidence for multiple ferroelectric phases appearing under high fields.

Thin film papers have been selected from the extensive work in MRL on ferroelectric films because of their relevance to transduction in piezoelectric or phase switching compositions.

MATERIALS FOR ADAPTIVE STRUCTURAL ACOUSTIC CONTROL

Period February 1, 1994 to January 31, 1995

Annual Report

VOLUME IV

OFFICE OF NAVAL RESEARCH
Contract No.: N00014-92-J-1510

APPROVED FOR PUBLIC RELEASE — DISTRIBUTION UNLIMITED

Accesion For		
NTIS CRA&I		☑
DTIC TAB		☐
Unannounced		☐
Justification		
By		
Distribution /		
Availability Codes		
Dist	Avail and / or Special	
A-1		

L. Eric Cross

PENNSTATE

1 8 5 5

THE MATERIALS RESEARCH LABORATORY
UNIVERSITY PARK, PA

TABLE OF CONTENTS

APPENDICES

VOLUME I

General Summary Papers

1. Newnham, R.E., S. Trolier-McKinstry and J.R. Giniewicz, "Piezoelectric, Pyroelectric and Ferroic Crystals, *J. Mater. Educ.* **15**, 189-223 (1993).

2. Newnham R.E., "Electroceramics in the 1990s and Beyond, *Euroceramics II*, Vol. 3, Deutsche Keramische Gesellschaft Köln, Germany, 1771-1782 (1994).

3. Newnham, R.E. and V. Sundar, "Anisotropy in Electrostriction and Elasticity," *J. Mat. Sci. Lett.* **13**, 799-801, Chapman and Hall, London, England (1994).

General Summary Papers (continued) –Volume I

4. Cross, L.E., "Relaxor Ferroelectrics: An Overview," *Ferroelectrics* **151**, 305-320 (1994).

5. Cross, L.E., Boundary Conditions for Shape Memory in Ceramic Material Systems, *J. Intelligent Material Systems on Structures* **6**, 55 (1994).

6. Uchino, K. and S.Y. Chu, "Photostriction and Its Applications," Proc. Amer. Ceram. Soc. Pac. Rim Conf., *Ferroic Materials*, 287-293 (1994).

7. Kumar, S., A.S. Bhalla and L.E. Cross, "Smart Ceramics for Broadband Vibration Control," *J. Intelligent Materials Systems and Structures* **5**(5), 673 (1994).

8. Kumar, S., A.S. Bhalla and L.E. Cross, "Smart Ferroelectrics for Acoustic and Vibration Control," *J. Intelligent Materials Systems and Structures* **5**(5), 678 (1994).

Materials Studies

9. Rossetti, G., L.E. Cross and J.P. Cline, "Structural Aspects of the Ferroelectric Phase Transition in Lanthanum-Substituted Lead Titanate," *J. of Mat. Sci.* **30**(1), 24-34 (1995).

10. Rossetti, G.A., Jr., M.A. Rodriguez, A. Navrotsky, L.E. Cross and R.E. Newnham, "Structure of the Defect Perovskite $[Pb_{0.85}La_{0.10}]TiO_3$ between 10 and 1023K," *J.Appl. Phys.***77**(4), 1683 (1994)

11. Zhang, Q.M., H. Wang, N. Kim and L.E. Cross, "Direct Evaluation of Domain-Wall and Intrinsic Contributions to the Dielectric and Piezoelectric Response and Their Temperature Dependence on Lead Zirconate-Titanate Ceramics," *J. Appl. Phys.* **75**(1), 454-9 (1994).

12. Li, Shaoping, A.S. Bhalla, R.E. Newnham, L.E. Cross and C.-Y. Huang, "90° Domain Reversal in $Pb(Zr_xTi_{1-x})O_3$ Ceramics," *J. Mater. Sci.* **29**(5), 1290-4 (1994).

13. Li, S., J. Sheen, S.-J. Jang, A.S. Bhalla, R.E. Newnham and L.E. Cross, "Modified Lumped Parameter Method for Measurements of Dielectric Susceptibility in Ferroelectrics," *Jpn. J. Appl. Phys.*, Part 1 **33**(6A), 3617-21 (1994).

14. Troilo, L.M., D. Damjanovic and R.E. Newnham, "Modified Lead Titanate Ceramics with a Relatively Large Dielectric Constant for Hydrophone Applications," *J. Am. Cer. Soc.* **77**(3), 857-59 (March 1994).

15. Subbarao, E.C., V. Srikanth, W. Cao and L.E. Cross, "Domain Switching and Microcracking During Poling of Lead Zirconate Titanate Ceramics," *Ferroelectrics* **145**, 771-781 (1993).

16. Jiang, Q.Y., E.C. Subbarao and L.E. Cross, "Dielectric Properties of Single Grain in PLZT Ferroelectric Ceramics," *Ferroelectrics Lett.* **17**, 41-46 (1994).

17. Wang, J.F., J. Gineiwicz and A.S. Bhalla, "Soft Piezoelectric (1-x)Pb(Sc$_{0.5}$Ta$_{0.5}$)O$_{3-x}$PbTiO$_3$ Ceramics with High Coupling Factors and Low Qm," *Ferroelectrics Lett.* **16**, 113-118 (1993).

18. Alberta, E.F., A.S. Bhalla and T. Takenaka, "The Complex Piezoelectric, Elastic, and Dielectric Coefficients for a Lead Zirconate-Based Ceramic Under Electrical Bias," *Ferroelectrics* **154**, 11 (1994).

VOLUME II

19. Alberta, E.F., A.S. Bhalla and T. Takenaka, "The Piezoelectric, Elastic and Dielectric Constants for Ceramics in the Solid Solution (x)PbZrO$_3$-(1-x-z)PbZn$_{1/3}$Nb$_{2/3}$O$_3$ - (z) PbTiO$_3$," *Ferroelectrics* (in press).

20. Alberta, E.F and A.S. Bhalla, "An Evaluation of Lead-Zirconate Based Ceramics For Use In Non-Volatile Ferroelectric Memory Devices," *Proceedings of the 9th Annual International Symposium on the Applications of Ferroelectrics* (1994).

21. Alberta, E.F. and A.S. Bhalla, "Dielectric and Piezoelectric Properties of Ceramics in the Lead Indium Niobate Lead Scandium Tantalate Solid Solution System," *Proceedings of the 9th Annual International Symposium on the Applications of Ferroelectrics* (1994).

22. Jin, B.-M., A.S. Bhalla, J.-B. Kim and J.-N. Kim, "Dielectric Response of Li$_{0.4}$K$_{0.6}$NbO$_3$ Crystal in the Frequency Domain," *J. Mat. Sci. Mat. Electronics* **4**, 225-228 (1993).

23. Jin, B.-M., A.S. Bhalla, B.-C. Choi and J.-N. Kim, "Dielectric Anomalies in Li$_{0.4}$K$_{0.6}$NbO$_3$ Crystals," *Physica Sta. Solidi.* **140**, 239-245 (1993).

24. Oh, K.Y., K. Uchino and L.E. Cross, "Optical Study of Domains in Ba(Ti,Sn)O$_3$ Ceramics," *J. Amer. Ceram. Soc.* **77**(11), 2809-16 (1994).

25. Idink, H., V. Srikanth, W.B. White and E.C. Subbarao, "Raman Study of Low Temperature Phase Transitions in Bismuth Titanate, Bi$_4$Ti$_3$O$_{12}$," *J. Appl. Phys.* **76**(3), 1819-1823 (1994).

Composite Sensors

26. Newnham, R.E. and K.A. Markowski, "Composite Sensors and Actuators," Submitted for Proceedings of the Japan-U.S. Workshop on Functional Fronts in Advanced Ceramics, Tsukuba, Japan, December 6-8, 1994.

27. Dogan, A., S. Yoshikawa, K. Uchino and R.E. Newnham, "The Effect of Geometry on the Characteristics of the Moonie Transducer and Reliability Issues," *Proceedings of the IEEE Ultrasonics Symposium* **2**, 935-939 (1994).

28. Xu, Q.C., A. Dogan, J. Tressler, S. Yoshikawa and R.E. Newnham, "Ceramic-Metal Composite Actuator," *Ferroelectrics Special Issue on Piezoelectric and Electrostrictive Actuators* **160** (1994).

Composite Sensors (continued) –Volume II

29. Onitsuka, K., A. Dogan, Q.C. Xu, S. Yoshikawa and R.E. Newnham, "Design Optimization for Metal-Ceramic Composite Actuator, 'Moonie'," *Ferroelectrics* **156**, 37-42 (1994).

30. Tressler, J.F., Q.C. Xu, S. Yoshikawa, K. Uchino and R.E. Newnham, "Composite Flextensional Transducers of Sensing and Actuation," *Ferroelectrics* **156**, 67-72 (August 1994).

31. Meyer, R., H. Weitzing, Q.C. Xu, Q.M. Zhang, R.E. Newnham and J.K. Cochran, "Lead Zirconate Hollow-Sphere Transducers," *J. Am. Ceram. Soc.* **77**(6), 1669-72 (1994).

32. Wang, H., Q.M. Zhang, L.E. Cross and A.O. Sykes, "Piezoelectric, Dielectric, and Elastic Properties of Poly (Vinylidene Fluoride/Trifluoroethylene)," *J. Appl. Phys.* **74**(5), 3394-3398 (1993).

33. Wang, H., Q.M. Zhang and L.E. Cross, "Piezoelectric Relaxation of P(VDF-TrFE) Copolymer," *Ferroelectrics* **159**, 218-286 (1994).

34. Zhang, Q.M., W. Cao, H. Wang and L.E. Cross., "Characterization of the Performance of 1-3 Type Piezocomposites for Low-Frequency Applications," *J. Appl. Phys.* **73**(3), 1403-1410 (1993).

35. Zhang, Q.M., H. Wang and L.E. Cross, "Piezoelectric Tubes and 1-3 Tubular Composites as Tunable Actuators and Sensors," *Proc. SPIE-Int. Soc. Opt. Eng. (1993)*, 1916 (Smart Materials), 244-54.

36. Zhang, Q.M., H. Wang and L.E. Cross, "Piezoelectric Tubes and Tubular Composites for Actuator and Sensor Applications," *J. Mater. Sci.* **28**(14), 3962-3968 (1993).

Actuator Studies

37. Newnham, R.E., A. Dogan, Q.C. Xu and S. Yoshikawa, "Flextensional 'Moonie' Actuators," *IEEE 1993 Ultrasonics Symposium Proc.,* Baltimore, Maryland, Vol. 1, 509-514 (Oct. 31-Nov. 3, 1993).

38. Dogan, A., Q. Xu, K. Onitsuka, S. Yoshikawa, K. Uchino and R.E. Newnham, "High Displacement Ceramic Metal Composite Actuators (Moonies)," *Ferroelectrics* **156**, 1 (1994).

39. Uchino, K., "Manufacturing Technology of Multilayered Transducers," *Proc. Amer. Ceram. Soc.* (in press).

40. Furuta, A. and K. Uchino, "Destruction Mechanism of Multilayer Ceramic Actuators: Case of Antiferroelectrics," *Ferroelectrics* **160**, 277-285 (1994).

41. Aburatani, H., S. Harada, K. Uchino, A. Furuta and Y. Fuda, "Destruction Mechanisms in Ceramic Multilayer Actuators," *Jpn. J. Appl. Phys.* **33**, 3091-3094 (1994).

Actuator Studies (continued) –Volume II

42. Uchino, K. and H. Aburatani, "Destruction Detection Techniques for Safety Piezoelectric Actuator Systems," *Proc. 2nd Int'l Conf. Intelligent Mater.*, pp. 1248-56 (1994).

VOLUME III

43. Takahashi, S., S. Hirose and K. Uchino, "Stability of PZT Piezoelectric Ceramics Under Vibration-Level Change," *J. Amer. Ceram. Soc.* **77**(9), 2429-32 (1994).

44. Jiang, Q.Y., E.C. Subbarao and L.E. Cross., "Effect of Composition and Temperature on Electric Fatigue of La-Doped Lead Zirconate Titanate Ceramics," *J. Appl. Phys.* **75**(11), 7433-7443 (1994).

45. Srikanth, V. and E.C. Subbarao, "Acoustic Emission Study of Phase Relations in Low Y_2O_3 Portions of ZrO_2-Y_2O_3 System," *J. Mater. Sci.* **29**, 3363-3371 (1994).

46. Chu, S.Y., Z. Ye and K. Uchino, "Impurity Doping Effect on Photostriction in PLZT Ceramics," *J. Adv. Performance Mater.* **1**, 129-143 (1994)..

47. Chu, S.Y., Z. Ye and K. Uchino, "Photovoltaic Effect for the Linearly Polarized Light in (Pb,La)(Zr,Ti)O_3 Ceramics," *Smart Mater. Struct.* **3**, 114-117 (1994).

48. Chu, S.Y., M.L. Mulvihill, Z. Ye and K. Uchino, "Bulk Photovoltaic Effect for the Linearly Polarized Light in $Pb(Zn_{1/3}Nb_{2/3})O_3$ Single Crystals," *Jpn. J. Appl. Phys.* **34** (Part 1, No. 2A) (1995).

49. Mulvihill, M.L., L.E. Cross and K. Uchino, "Low Temperature Dynamic Observation of Relaxor Ferroelectric Domain in Lead Zinc Niobate," *J. Amer. Ceram. Soc.* (in press).

50. Uchino, K., "Electrooptic Ceramics and Their Display Applications," *Ceramics International* (in press).

51. Lee, D., J. Yuk, N. Lee and K. Uchino, "Humidity-Sensitive Properties of Nb_2O_5-Doped Pb(Zr,Ti)O_3," *Sensor and Mater.* **5**(4), 231-240 (1994).

52. Lee, N.Y., N. Usuki, H. Aburatani, Y. Ito and K. Uchino, "Pb/Ti Ratio of RF-Magnetron Sputtered $PbTiO_3$ Thin Films," *Jpn. J. Appl. Phys.* (accepted).

Integration Issues

53. Dougherty, J.P. and Y. Chen, "Tailoring Materials for Smart Applications," Invited Paper, *Proc. 1994 Intl. Conf. on Intelligent Materials*, June 5-8, 1994, Williamsburg VA.

54. Hackenberger, W.S., T.R. Shrout, J.P. Dougherty and R.F. Speyer, "The Effect of Differential Shrinkage on the Sintering and Microstructural Development of Low-Temperature Co-Firable Multilayer Substrates," *Proc. SAMPE/ISHM 7th International Electronics Conference*, pp. 643-650, Parsippany, NJ, June 20-23, 1994

55.   Wang, S.F., J.P. Dougherty, W. Huebner, and J.G. Pepin, "Silver-Palladium Thick Film Conductors," published as the feature article in *Journal of the American Ceramic Society* 77(12), 3051-72 (December 1994).

56.   Sample, D.R., P.W. Brown and J.P. Dougherty, "The Microstructural Evolution of Copper Thick Films Observed by Environmental Scanning Microscopy," *J. American Ceramic Society* (in press).

VOLUME IV

57.   Fiallo, H.H., J.P. Dougherty, S.J. Jang, R.E. Newnham and L. Carpenter, "Transmission Properties of Metal-Semiconductor-Relaxor Microstrip Lines", *IEEE Trans. Microwave Theory & Techniques* 42(7), 1176-1182, (July 1994).

58.   Dougherty, J.P., M. Megherhi, and H.H. Fiallo, "Integrated Filters and Over Voltage Protection in Multilayer Ceramic Packaging Materials," *Proc. Eighth Cimtec World Ceramics Conference*, Florence, June 29-July 4, 1994.

Processing Studies

59.   Miller, D.V., C.A. Randall, A.S. Bhalla, R.E. Newnham and J.H. Adair, "Electrorheological Properties of BaTiO$_3$ Suspensions," *Ferroelectrics Lett.* 15, 141-151 (1993).

60.   Fielding, J.T., Jr., T.R. Shrout and S.J. Jang, "Increased Operating Temperature Range in La-Modified Pb(Mg$_{1/3}$Nb$_{2/3}$O$_3$-PbTiO$_3$ Relaxor Ferroelectric-Based Transducers," *Proc. 9th ISAF*, State College, PA (August 1994).

61.   Fielding, J.T., Jr., S.J. Jang and T.R. Shrout, "Field-Induced Piezoelectric Materials for 100 kHz-10 MHz Transducer Applications," *Proc. 9th ISAF*, State College, PA (August 1994).

62.   Brodeur, Russell P., Kamau wa Gachigi, Philip M. Pruna and Thomas R. Shrout, "Ultra-High Strain Ceramics with Multiple Field-Induced Phase Transitions," *J. Am. Ceram. Soc.* 77(11), 3042 (1994).

63.   Yoshikawa, S., N. Kim, T. Shrout, Q. Zhang, P. Moses and L.E. Cross, "Field-Induced Lead Zirconate Titanate Stannate Antiferroelectric-to-Ferroelectric Phase Switching Ceramics," *Proc. 9th ISAF*, State College, PA (August 1994).

64.   Gururaja et al., "Electrostrictive Ultrasonic Probe Having Expanded Operating Temperature Range," United States Patent, Patent Number: 5,345,139, Date of Patent: September 6, 1994.

65.   Yoon, K.H., Y.S. Cho, D.K. Kang, K. Uchino and K.Y. Oh, "Effect of Eutectic Lithium Sulphate-Sodium S   ,hate Flux on the Synthesis of Lead Magnesium Niobate," *Ferroelectrics* 1   255-264 (1994).

66.   Brooks, K.G., J. Chen, K.R. Udayakumar and L.E. Cross, "Electric Field Forced Phase Switching in La-Modified Lead Zirconate Titanate Stannate Thin Films," *J. Appl. Phys.* **75**(3), 1699-704 (1994).

67.   Ghosh, P.K., A.S. Bhalla and L.E. Cross, "Surface Morphology of r.f. Sputtered Bismuth Titanate Thin Films," *J. Materials Science* **29**, 4659-4662 (1994).

68.   Lee, N.Y., T. Sekine, Y. Ito and K. Uchino, "Deposition Profile of RF-Magnetron-Sputtered $BaTiO_3$ Thin Films," *Jpn. J. Appl. Phys.* **33** (Part 1, No. 3A), 1484-88 (1994).

Graduating Students in the Program

69.   Dogan, Aydin. PhD Thesis (Abstract), Materials Program. Flextensional "Moonie and Cymbal" Actuators. December 1994.

70.   Wang, Hong. PhD Thesis (Abstract), Materials Program. Electromechanical Effects in Polymeric Materials. August 1994.

71.   Tressler, James F. Master of Science (Abstract), Ceramic Science. Smart Ceramic-Metal Composites for Active Vibration Control. December 1993.

INTEGRATION ISSUES
(continued)

APPENDIX 57

Transmission Properties of Metal–Semiconductor–Relaxor Microstrip Lines

Héctor H. Fiallo, Joseph P. Dougherty, *Member, IEEE*, Sei-Joo Jang, Robert E. Newnham, and Lynn A. Carpenter, *Member, IEEE*

Abstract— The transmission characteristics of multilayer ferrite-high-K microstrip lines have been calculated by means of the parallel-plate waveguide approximation. The relaxation behavior of the dielectric permittivity and permeability have been taken into account by using the Debye and the Maxwell–Wagner relaxation models. The results demonstrate that these lines can be used as very small size delay lines and low-pass filters that can be tuned by adjusting the layer thickness ratio, the resistivity of the semiconductor layer, and the difference between the permittivity–permeability product of each layer.

I. INTRODUCTION

PLANAR Metal–Insulator–Semiconductor (MIS) transmission lines are used in the integrated circuit industry as delay lines [1], slow-mode transmission devices [2], pulse modulators [3], and other applications where the propagation constant is required to have a dispersive behavior. In this paper, the parallel-plate waveguide approximation used to calculate the transmission properties of MIS has been extended to calculate the transmission characteristics of metal–semiconductor–relaxor (MSR) microstrip lines. The final goal is to create the tools to fabricate very small size devices like delay lines and low-pass filters that can be incorporated into the packaging substrate.

Magnetic semiconductors (e.g., ferrites), and relaxor dielectrics (e.g., lead magnesium niobate) exhibit relaxation of their dielectromagnetic properties with frequency. The relaxation of the dielectric permittivity of the relaxor dielectric has been modeled with the Debye relaxation approximation. The relaxation of the permittivity of the semiconducting ferrites has been introduced by means of the Maxwell–Wagner relaxation model [4]. And finally, the magnetic relaxation of the ferrite has been approximated by a dual Debye relaxation model for frequencies below the low gigahertz range [6].

The transmission characteristics for MSR lines were obtained by solving the equations for a LSE (Longitudinal Surface Electric) mode of the parallel-plate waveguide equivalent as described by Guckel [5], and Hasegawa [1].

Our model was tested against published data for MIS since there are no data for MSR lines. The solutions obtained with this model agree within an error of less than 5% with the published data. The model was tested against experimental
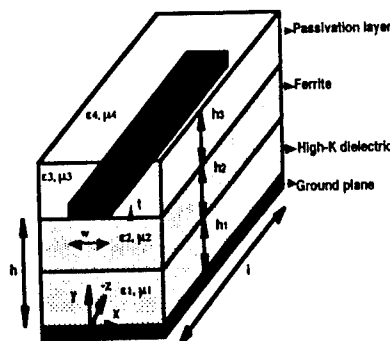
Fig. 1. Multilayer microstrip line modeled in this study. The figure shows the layer thicknesses, identification, and axes orientation. ϵ^* and μ^* are the complex relative permittivity and permeability, respectively.

data for MSR lines. The results show that the theoretical values agree within an error of less than 10%.

The response of the MSR lines is quite similar to the frequency response of MIS lines. At low frequencies a slow-wave mode predominates, and at high frequencies a quasi-TEM mode is dominant. The frequency response proved to be sensitive to the resistivity of the semiconductor material. The attenuation and characteristic impedance can be controlled with the geometry of the line, the resistivity of the semiconductor, and the dielectromagnetic properties of the materials used.

II. MODEL

The geometry that is of interest for this study is the one depicted in Fig. 1. This configuration has been chosen because it is close to the actual geometry for electronic packaging.

The modeling procedure can be described as follows: the first step in this model is to assume that at zero and optical frequencies the quasi-TEM approximation is valid as it has been demonstrated elsewhere in the literature [6]. The effective values of the permittivity and permeability can be calculated by using the variational approach devised by Yamashita [7]. The microstrip line is assumed to be completely filled with each of the substrates one at a time, and the effective values are calculated for the total substrate thickness. After finding the effective values for each material at zero and very high frequencies, these values are introduced into the relaxation models described before. The partial thicknesses are calculated from the optical limit of the relaxation models. These thickness values are used with the parallel-plate waveguide

model and the complex propagation constant and characteristic impedance are evaluated.

The quasi-TEM approximation to calculate the zero and optical effective values of the permittivity and permeability of each layer requires the solution of the electrostatic Poisson's equation and its magnetic analog. For the electrostatic case, the equation to solve is

$$\nabla^2\psi(x, y) = \frac{-\rho(x)\delta(y - h)}{\epsilon_0\epsilon_i} \tag{1}$$

where $\psi(x, y)$ is the electric potential, $\rho(x)$ is the charge density distribution, ϵ_0 is the free space permittivity, ϵ_i is the real part of the complex permittivity of the ith layer, h is the strip height $(h_1 + h_2)$, and $\delta(y - h)$ is the Dirac function to mimic the charge distribution at y equal to h.

For the magnetic case, restricting the current flow to the z direction, the equation to solve is

$$\nabla^2 A(x, y) = -\mu_i\mu_0 J(x, y)\delta(x, y - h) \tag{2}$$

where $A(x, y)$ is the magnetic vector potential in the xy plane, $J(x, y)$ is the current density, $\delta(x, y-h)$ is the Dirac function, μ_i is the real part of the complex magnetic permeability of the ith layer, and μ_0 is the free space permeability.

Solutions to (1) and (2), for the geometry given in Fig. 1, have been obtained by means of the variational method [6]. The effective permittivity can be evaluated as

$$\epsilon_{\text{eff}} = C_T/C_0 \tag{3}$$

where

$$\frac{1}{C_T} = \frac{1}{\pi Q^2}\int_0^\infty \rho(\beta)\psi(\beta, h)T(\beta)\, d\beta \tag{4}$$

Q is the strip charge, β is the spectral domain variable, and C_0 is the geometrical capacitance of the line, i.e., when the substrate is air.

The difference between this model and the one reported by Yamashita [7] is the spectral form of the electrostatic potential. The potential here is given by

$$\psi(b, h) = \rho(b)G(b, h) \tag{5}$$

where

$$G(\beta, h) =$$
$$\frac{[\epsilon_2\,\text{Coth}\,(\beta h_2) + \epsilon_1\,\text{Coth}\,(\beta h_1)][\epsilon_3\,\text{Coth}\,(\beta h_3) + \epsilon_4]}{|\beta|\{\epsilon_1\,\text{Coth}\,(\beta h_1)K_1(\beta, h) + K_2(\beta, h)\}} \tag{6}$$

and

$$K_1(\beta, h) = \epsilon_2[\epsilon_3\,\text{Coth}\,(\beta h_2)\,\text{Coth}\,(\beta h_3)$$
$$+ \epsilon_4\,\text{Coth}\,(\beta h_2)] + \epsilon_3[\epsilon_3 + \epsilon_4\,\text{Coth}\,(\beta h_3)]$$

$$K_2(\beta, h) = \epsilon_2\epsilon_3[\epsilon_2\,\text{Coth}\,(\beta h_3)$$
$$+ \epsilon_4\,\text{Coth}\,(\beta h_3)\,\text{Coth}\,(\beta h_2) + \epsilon_3\,\text{Coth}\,(\beta h_2)] + \epsilon_2^2\epsilon_4.$$

The variable $\rho(\beta)$ is the spectral form of the charge distribution as given by Yamashita [7].

The solution of the magnetostatic equation was carried out in an analogous way to the electrostatic case. The effective permeability was calculated as

$$u_{\text{eff}} = \frac{L}{L_0} \tag{7}$$

where L_0 is the geometrical inductance, i.e., the air-filled line. and

$$L = \frac{\mu_0}{\pi i^2}\int_0^\infty J^2(\beta)G_m(\beta, h)T(\beta)\, d\beta \tag{8}$$

where i is the strip current, $J(\beta)$ is the current distribution which was considered to have the same form as the charge distribution in the electrostatic case. Our Green's function is given by [6]

$$G_m(\beta, h) =$$
$$\frac{\mu_2\mu_3[\mu_1\,\text{Coth}\,(\beta h_2) + \mu_2\,\text{Coth}\,(\beta h_1)][\mu_4\,\text{Coth}\,(\beta h_3) + \mu_3]}{|\beta|\{\mu_2\,\text{Coth}\,(\beta h_1)K_{1m}(\beta, h) + K_{2m}(\beta, h)\}} \tag{9}$$

where

$$K_{1m}(\beta, h) = \mu_3\,\text{Coth}\,(\beta h_3)[\mu_4\,\text{Coth}\,(\beta h_2) + \mu_2]$$
$$+ \mu_3^2\,\text{Coth}\,(\beta h_2) + \mu_2\mu_4$$

$$K_{2m}(\beta, h) = \mu_1\{\mu_3[\mu_4\,\text{Coth}\,(\beta h_3) + \mu_2\,\text{Coth}\,(\beta h_3)$$
$$\cdot\,\text{Coth}\,(\beta h_2) + \mu_3] + \mu_2\mu_4\,\text{Coth}\,(\beta h_2)\}.$$

After calculating the effective dielectric permittivity and the effective permeability for each layer at zero and optical frequencies, the optical values are used to calculate the equivalent thicknesses of the substrate layers in the parallel-plate waveguide equivalent. The thicknesses are evaluated by solving the following equations:

$$\frac{h}{\epsilon_{\text{eff}}} = \frac{h_1}{\epsilon_{\text{eff}\,1}} + \frac{h_2}{\epsilon_{\text{eff}\,2}} \tag{10}$$

$$\mu_{\text{eff}}h = \mu_{\text{eff}\,1}h_1 + \mu_{\text{eff}\,2}h_2 \tag{11}$$

where ϵ_{eff} and μ_{eff} are the effective values of permittivity and permeability for the multilayer structure at optical frequencies. The variables $\epsilon_{\text{eff}\,1}$ and $\epsilon_{\text{eff}\,2}$ are the partial effective permittivities when the substrate is filled with either one of the materials, and $\mu_{\text{eff}\,1}$ and $\mu_{\text{eff}\,2}$ are the partial effective permeabilities when the substrate is filled with each one of the materials.

The next step is to insert the zero frequency partial effective permittivities and permeabilities in the relaxation model that best fits the real behavior of the substrate materials. For relaxor dielectrics at frequencies below the low gigahertz range, the Debye relaxation model can be used with a variation suggested by Cole *et al.* [8] to take into account the nonideal response of these materials, i.e., the Cole–Cole plot is not a real-axis-centered semicircle. The equations for this case are

$$\epsilon_1' = \epsilon_{\text{eff}\,i}(\infty) + \frac{[\epsilon_{\text{eff}\,i}(0) - \epsilon_{\text{eff}\,i}(\infty)][1 + (\omega\tau)^{1-\delta}\sin\phi]}{1 + 2(\omega\tau)^{1-\delta}\sin\phi + (\omega\tau)^{2(1-\delta)}} \tag{12}$$

$$\epsilon_1'' = \frac{[\epsilon_{\text{eff}\,i}(0) - \epsilon_{\text{eff}\,i}(\infty)](\omega\tau)^{1-\delta}\cos\phi}{1 + 2(\omega\tau)^{1-\delta}\sin\phi + (\omega\tau)} \tag{13}$$

where ϵ_i' is the real part of the frequency dependent permittivity of the ith layer $(i = 1, 2)$, and ϵ_i'' is the imaginary part. The variables $\epsilon_{\text{eff}\,i}(0)$ and $\epsilon_{\text{eff}\,i}(\infty)$ are the layer effective permittivity for zero and optical frequency respectively. ω is

the angular frequency, and τ is the relaxation time that has to be measured. The variables ϕ and δ are calculated from

$$\phi = \frac{\pi}{2}\delta \tag{14}$$

where ϕ is the angle that the radius of the nonideal Cole–Cole plot forms with the real axis [8].

The relaxation behavior of the permittivity of ferrite semiconductors is well approximated by the Maxwell–Wagner relaxation model. Since these materials exhibit a nonideal relaxation the adjustment introduced by the δ factor is applicable in this case. The real part of the permittivity in the Maxwell–Wagner model has the same form as for the Debye model. The imaginary part has to be corrected for conduction losses, and it is given by

$$\epsilon_i'' = \frac{[\epsilon_{\text{eff }i}(0) - \epsilon_{\text{eff }i}(\infty)](\omega\tau)^{1-\delta}\cos\phi}{1 + 2(\omega\tau)^{1-\delta}\sin\phi + (\omega\tau)^{2(1-\delta)}} + \frac{\sigma_i(0)}{\epsilon_0\omega} \tag{15}$$

where $\sigma_i(0)$ is the dc conductivity of the ith layer, ϵ_0 is the free space permittivity, and ω is the angular frequency.

The magnetic relaxation for frequencies under the low gigahertz range can be modeled by solving the dc and ac equations of an equivalent circuit obtained after applying the duality principle to the circuit used in the Debye relaxation model. Although this approximation does not show the low frequency relaxation present in the spectra of most ferrites, it is a good approximation for ferrites that have been diluted in a diamagnetic phase. [9] The equations to approximate the real and imaginary part of the permeability are [6]

$$\mu_i' = \frac{\mu_{\text{eff }i}(\infty)\mu_{\text{eff }i}(0)[\mu_{\text{eff }i}(\infty) + \omega^2\tau_m^2\mu_{\text{eff }i}(0)]}{\mu_{\text{eff }i}(0)\omega^2\tau_m^2 + \mu_{\text{eff }i}(\infty)} \tag{16}$$

$$\mu_i'' = \frac{[\mu_{\text{eff }i}(0) - \mu_{\text{eff }i}(\infty)]\mu_{\text{eff }i}(\infty)\mu_{\text{eff }i}(0)\omega\tau_m}{\mu_{\text{eff }i}(0)\omega^2\tau_m^2 + \mu_{\text{eff }i}(\infty)} \tag{17}$$

where $\mu_{\text{eff }i}(0)$ and $\mu_{\text{eff }i}(\infty)$ are the effective permeability of the ith layer calculated for zero and optical frequencies, respectively. The variable τ_m is the relaxation time of the material that must be measured. The relaxation model for the permeability at low frequencies can be modified in the same way as the relaxation model for the permittivity. This assumes that the Cole–Cole plot of the complex permeability is semicircle not centered on the real axis.

The solution of the complex propagation constant and the characteristic impedance for the parallel-plate waveguide equivalent requires the solution of the wave equation for a non-TEM mode. In fact the solution can be obtained by using the techniques for solving surface-wave modes. i.e., LSE, LSM modes. The LSE mode or TM to y mode has been solved in this case. The solution process can be found elsewhere in the literature [10], [11]. Starting from the eigenvalue characteristic equation and using the continuity condition at the interface the following equations can be found:

$$\gamma_{y1}^2 + \gamma_z^2 = -\omega^2\epsilon_0\mu_0\epsilon_1^*\mu_1^* \tag{18}$$

$$\gamma_{y2}^2 + \gamma_z^2 = -\omega^2\epsilon_0\mu_0\epsilon_2^*\mu_2^* \tag{19}$$
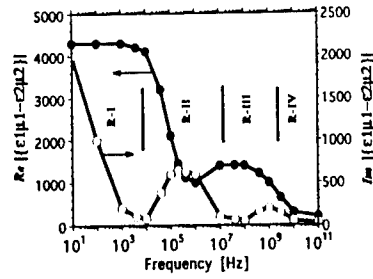

Fig. 2. Absolute value of the real and imaginary part of the permittivity–permeability product difference for a metal–semiconductor–relaxor microstrip line made of layers of Pb (Mg, Nb, Ti)O$_3$ and NiZnFe$_2$O$_4$.

$$\frac{\gamma_{y1}}{\epsilon_1^*}\text{Tanh}\,(\gamma_{y1}h_1) + \frac{\gamma_{y2}}{\epsilon_2^*}\text{Tanh}\,(\gamma_{y2}h_2) = 0 \tag{20}$$

where γ_{yi} is the ith propagation constant in the y direction for the TM-y mode, γ_z is the complex propagation constant in the z direction. ϵ_i^* and μ_i^* are the frequency dependent complex permittivity and permeability of the ith layer, respectively.

Equations (18) and (19) can be reduced to an eigenvalue equation for γ_{yi}, the equation to solve is

$$\gamma_{y1}^2 - \gamma_{y2}^2 + \omega^2\epsilon_0\mu_0(\epsilon_1^*\mu_1^* - \epsilon_2^*\mu_2^*) = 0. \tag{21}$$

The solutions are found by solving (20) and (21) simultaneously for each frequency. Although it is possible to find a complete solution for this system, the procedure is time consuming and sometimes does not converge to a solution. Instead, some meaningful approximations are possible based on the dielectromagnetic spectra of the permeability–permittivity product difference. Fig. 2 shows the permeability–permittivity product difference for a sample made of nickel zinc ferrite and high permittivity lead magnesium niobate. The spectrum can be divided in four different regions. Region I is limited $0 \leq f \leq \min[(\sigma_i/(\epsilon_i\epsilon_0)$ where the layer with the larger conductivity is lossy. Region II has a range $\min[(\sigma_i/(\epsilon_i\epsilon_0] \leq f \leq \min[1/\tau_i, 1/\tau_{mi}]$ where both layers are lossy. The range of region III is $\min[1/\tau_i, 1/\tau_{mi}] \leq f \leq \max[1/\tau_i, 1/\tau_{mi}]$ where the nonmagnetic layer is lossy. Finally, region IV is the region above $f \geq \max[1/\tau_i, 1/\tau_{mi}]$ where the field distribution depends on the dielectric permittivity of the layers as in the case of a low-loss-partially filled waveguide.

Region I: In this region one of the substrate layers is very lossy because of conduction losses and the other can be considered lossless. The lossy material will be the ferrite semiconductor, and the losses material will be the relaxor dielectric. The propagation constants have to show these characteristics. The propagation constant in the lossy material γ_{y2} has to be larger than the propagation constant in the lossless material because the propagation constant in the z direction, γ_z, is almost zero in the lossy layer. Equation (20) can be reduced to the following form:

$$\frac{\gamma_{y1}^2}{\epsilon_1^*}h_1 + \frac{\gamma_{y2}}{\epsilon_2^*}\left[\gamma_{y2}h_2 - \frac{(\gamma_{y2}h_2)^3}{3}\right] = 0 \tag{22}$$

where the hyperbolic tangent has been approximated to the first order for the lossless line and to the second order for the lossy layer.
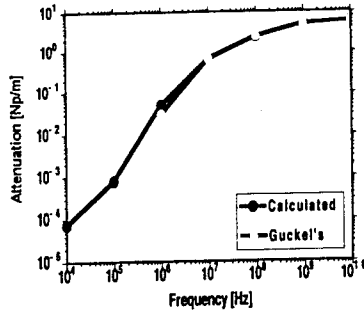
Fig. 3. Comparison of attenuation values in Np/m for a MIS microstrip line with the following parameters: $\epsilon_1 = 12$, $\epsilon_2 = 4.5$, $h_1 = 200$ μm, $h_2 = 0.5$ μm, $w = 1600$ μm. The conductivity of the second layer was 0.1 $[\Omega\text{-m}]^{-1}$.

Fig. 4. Comparison of wavelength ratios λ/λ_0 for the same MIS microstrip line described in Fig. 3.

Region II: After the conduction loss has decreased, the Debye or dipolar losses appear in both materials. The wave propagates through both materials. The latter means that at these frequencies the hyperbolic tangent has to be replaced by a polynomial approximation with more than one term. Equation (20) can be reduced to the following form:

$$\frac{\gamma_{y1}}{\epsilon_1^*}\left[\gamma_{y1}h_1 - \frac{(\gamma_{y1}h_1)^3}{3}\right] + \frac{\gamma_{y2}}{\epsilon_2^*}\left[\gamma_{y2}h_2 - \frac{(\gamma_{y2}h_2)^3}{3}\right] = 0. \tag{23}$$

Region III: The Debye losses in one of the materials (the one with the smallest relaxation time) have decreased together with the magnetic losses. In the structure of interest, the second layer becomes lossless, and the first layer is still lossy. The situation is opposite to the one analyzed in region one. The approximation for this region is given by

$$\frac{\gamma_{y1}}{\epsilon_1^*}\left[\gamma_{y1}h_1 - \frac{(\gamma_{y1}h_1)^3}{3}\right] + \frac{\gamma_{y2}^2}{\epsilon_2^*}h_2 = 0. \tag{24}$$

Region IV: This region resides within the gigahertz range. At these frequencies, it is difficult to approximate the hyperbolic tangent by a polynomial because the value of $\gamma_{yi}h_i$ can be larger than unity. For some cases, the following approximation to (20) gives meaningful results:

$$\frac{\gamma_{y1}}{\epsilon_1^*} + \frac{\gamma_{y2}}{\epsilon_2^*} + 0 \tag{25}$$

III. RESULTS

We have not found data in the literature for MSR microstrip lines to compare with our results. To ascertain whether or not our model gives useful results, the examples published by Guckel *et al.* [5] and Hasegawa *et al.* [1] for MIS microstrip lines were chosen as references. Figs. 3 and 4 show the results obtained from our model plotted against data obtained from Guckel's paper. It can be seen that the difference is less than 3% for the attenuation and the wave length ratio, also called the slow-wave factor. Figs. 5 and 6 show the results calculated from our model plotted against data published by Hasegawa. The values agree with a difference of less than 7%. The maximum difference was found in the wavelength ratio at high frequencies.

The reason for these differences is the fact that Hasegawa in his approximation assumed that the high frequency effective permittivity is the same as the optical value of the permittivity
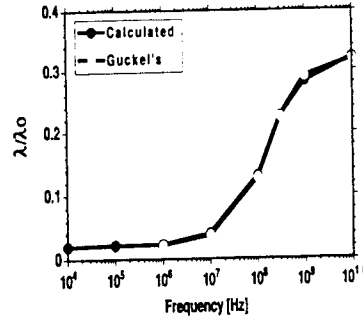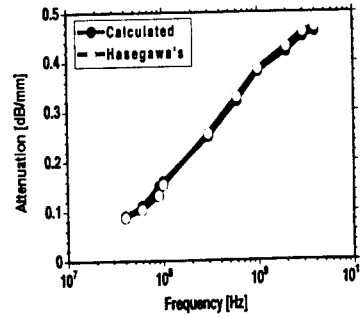

Fig. 5. Comparison of attenuation values in dB/m for a MIS microstrip line with the following parameters: $\epsilon_1 = 12$, $\epsilon_2 = 4.5$, $h_1 = 250$ μm, $h_2 = 1$ μm, $w = 1600$ μm. The conductivity of the second layer was 0.085 $[\Omega\text{-m}]^{-1}$.
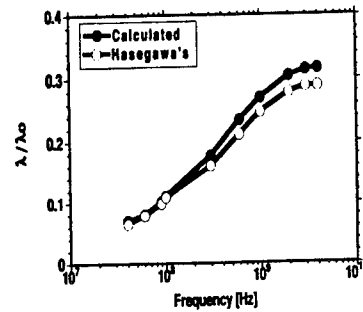

Fig. 6. Comparison of wavelength ratios λ/λ_0 for the same MIS microstrip line described in Fig. 5.

of the semiconductor substrate. In our model, the effective permittivity at high frequencies is smaller than the substrate permittivity because it was calculated using the variational permittivity. i.e., Hasegawa's $\epsilon_{Si} = 12$, our model $\epsilon_{eff\,Si} = 10$.

Samples of the structure of interest were prepared by gluing together layers of nickel zinc ferrite ($Ni_{1-x}Zn_xFe_2O_4$), and lead magnesium niobate ($PbMg_{1/3}Nb_{2/3}O_3$) relaxor ferroelectric. The adhesive was either epoxy resin or air dry silver paste. The dielectromagnetic characteristics and the thicknesses used as input for the model are given in Table I. Fig. 7 shows the calculated and measured values of attenuation in decibels for sample SH1. The errors are below 10% which means that for these parameters the approximation gives results that are reasonably accurate, especially if we consider that some attenuation factors have not been taken into account, e.g.,
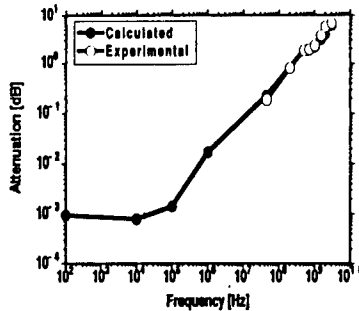
Fig. 7.   Comparison between experimental and predicted values of attenuation in decibels for sample SH1. See Table I for details.
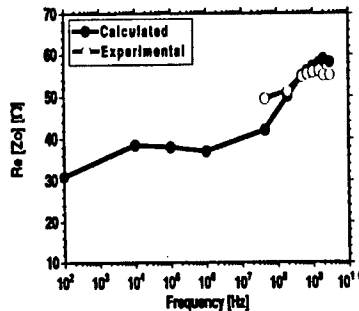

Fig. 8.   Comparison between experimental and predicted values of the real part of the characteristic impedance for sample SH1. See Table I for details.
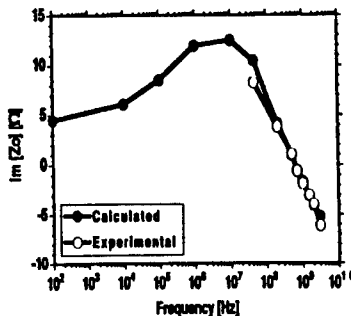

Fig. 9.   Comparison between experimental and predicted values of the imaginary part of the characteristic impedance for sample SH1. See Table I for details.

conductor losses, and radiation losses. Fig. 8 and 9 present the measured and calculated values of the real and imaginary parts of the characteristic impedance for sample SH1. It can be seen that the error is larger for frequencies in the gigahertz range. This discrepancy was expected since the approximation of the hyperbolic tangent fails in region IV.

The effect of changing the semiconductor resistivity and the layer thickness ratio was calculated. Fig. 10 shows the calculated attenuation in decibels for samples simulated with three different conductivities of the semiconducting ferrite: $2.34 \times 10^{-2} [\Omega\text{-m}]^{-1}$(SH2), $2.34 \times 10^{-5} [\Omega\text{-m}]^{-1}$(SH1), and $2.34 \times 10^{-8} [\Omega\text{-m}]^{-1}$(SH3). It can be seen that a change in the resistivity affects the response at low frequencies, which is understandable because the conduction losses appear in this frequency range. At high frequencies the response is the same

TABLE I
IDENTIFICATION AND PARAMETERS USED IN THE SIMULATIONS: ONLY SH1 WAS BOTH FABRICATED AND SIMULATED. EXAMPLES SH2, 3 WERE ONLY SIMULATED

EXAMPLES (*)	h_1 $\times 10^{-4}$ [m]	h_2 $\times 10^{-4}$ [m]	h_2/h_1	σ_1 $\times 10^{-7}$ $[\Omega\text{-m}]^{-1}$	σ_2 $\times 10^{-7}$ $[\Omega\text{-m}]^{-1}$
SH1	3.858	7.317	1.9	0.01	246.00
SH2	3.858	7.317	1.9	0.01	24600.00
SH3	3.858	7.317	1.9	0.01	2.46

(*) The following values were kept constant in both the samples and the simulations:

$\epsilon_1(0) = 10915$; $\epsilon_1(\infty) = 463.92$; $\epsilon_2(0) = 140$; $\epsilon_2(\infty) = 9.55$;
$\tau_1 = 10^{-9}$; $\tau_2 = 2 \times 10^{-7}$;
$\mu_1(0) = 1$; $\mu_1(\infty) = 1$; $\mu_2(0) = 9.475$; $\mu_2(\infty) = 1$;
$\tau_{m1} = 10^{-12}$; $\tau_{m2} = 3 \times 10^{-9}$
$w = 1.98$ mm; $l = 10.987$ mm
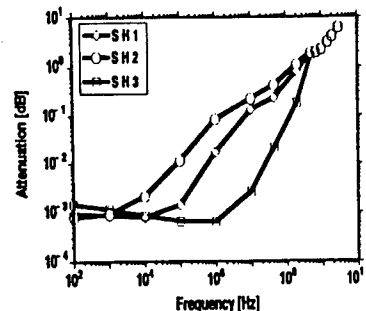w is the strip width and l is the line length.

Fig. 10.   Effect of the change in the conductivity of the semiconducting ferrite on the calculated attenuation of examples SH1, SH2, SH3. Notice the effect at low frequencies.
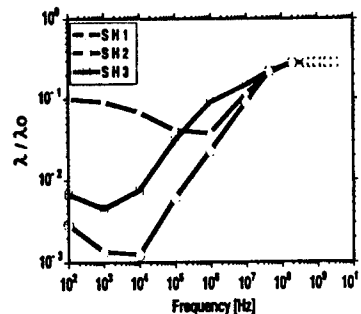

Fig. 11.   Effect of the change in the conductivity of the semiconducting ferrite on the calculated wavelength ratio of examples SH1, SH2, SH3. Notice the effect in the low frequencies.

for all three. The calculated slow-wave factors for samples SH1, SH2, and SH3 are shown in Fig. 11. It is possible to see that for conductivities close to $2.34 \times 10^{-5} [\Omega\text{-m}]^{-1}(\sigma_c)$ the slow-wave factor is almost independent of frequency. On the other hand, if the conductivity is very much lower or higher than σ_c the structure can be used as a delay line.

The calculated characteristic impedance was found to oscillate around the value 50 Ω if the conductivity was smaller than $2.34 \times 10^{-5} [\Omega\text{-m}]^{-1}$ for a frequency range between 10^2
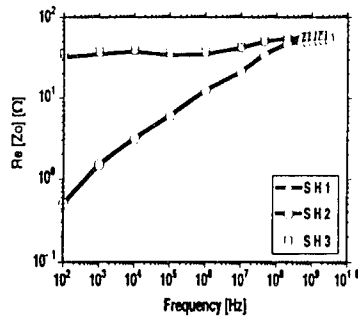
Fig. 12. Effect of the change in the conductivity of the semiconducting ferrite on the real part of the calculated characteristic impedance. Notice that the smaller the conductivity the flatter the response below 1 GHz.

to 10^9 Hz as shown in Fig. 12. In general, these figures suggest also that there may be a resistivity value that produces a minimum in the attenuation as found by Guckel [5] in his analysis of MIS. However, an explicit form of this minimum was not found. The behavior of the response of MSR lines for variations in the second layer resistivity can be used as a design criterion for choosing the materials in applications such as low-pass filters and delay lines.

Changing the thickness ratio had a minor effect unless the thickness of one of the layers was very thin $(h_2/h_1 < 0.5)$. The results suggested that a semiconducting layer is required but its thickness can be very small. This is important from the fabrication point of view.

The effect of changing the relaxation times was found to affect markedly the frequency response in regions II and III. The latter is understandable because the change in relaxation times means a change in the relation $\epsilon_1^* \mu_1^* - \epsilon_2^* \mu_2^*$. When this relation is close to zero the waveguide behaves as if were filled by a homogeneous material causing the TM$-y$ propagation to disappear [12]. The change in relaxation time. which can be achieved by modifying the materials physical properties, helps tune the attenuation maxima to the desired frequency. Following this, a third method can be developed to control the frequency response of MSR lines by utilizing materials whose difference in permittivity–permeability product is close to zero in the frequency range of interest.

IV. CONCLUSIONS

The parallel-plate waveguide approximation used for MIS along with the relaxation models for the dielectromagnetic properties of materials have been used to theoretically calculate the transmission characteristics of microstrip lines fabricated with layers of semiconducting ferrite and relaxor dielectrics.

The results were compared with published data and with experimental measurements. The published data for MIS lines was slightly different from the values calculated with our model. The difference can be explained by the mathematical treatment of the equation and the approximations involved. The experimental results for metal–semiconductor–relaxor lines showed that the model predicts the behavior accurately for frequencies up to the low gigahertz range. Above this range, the approximations used to obtain the solutions fail.

The results also showed that depending on three parameters; the conductivity of the semiconductor, the thickness ratio, and the difference in the permittivity–permability product, the frequency response can be tailored in a way that low-pass filters and delay lines of very small size can be fabricated with materials that are compatible with packaging technology. As this investigation proceeds, tables of suitable materials and their application are being produced. This will be the topic of a future publication.

REFERENCES

[1] H. Hasegawa, M. Furukawa, and H. Yanai, "Properties of Microstrip Lines on Si–SiO$_2$," IEEE Trans. Microwave Theory Tech., vol. MTT-19, pp. 869–881, Nov. 1971.
[2] H. Ogawa and T. Itoh, "Slow-wave characteristics of ferromagnetic-semiconductor microstrip line," IEEE Trans. Microwave Theory Tech., vol. MTT-34, pp. 1478–1482, Dec. 1986.
[3] Y. Quian and E. Yamashita, "Phase compensation and waveform reshaping of picosecond electrical pulses using dispersive microwave transmission lines," IEEE Trans. Microwave Theory Tech., vol. MTT-39, no. 6, pp. 924–929, June 1986.
[4] A. Von Hippel, Dielectrics and Waves. New York: Wiley, 1954, chs. 16 and 32.
[5] H. Guckel, P. Brennan, and I. Palócz, "A parallel-plate waveguide approximation to microminiaturized planar transmission lines for integrated circuits," IEEE Trans. Microwave Theory Tech., vol. MTT-15, pp. 468–476, Aug. 1967.
[6] H. Fiallo, "Multilayer ferrite-high-K dielectric 1 GHz low-pass filters," M.S. thesis, Pennsylvania State Univ., 1991.
[7] E. Yamashita, "Variational method for the analysis of microstrip-like transmission lines," IEEE Trans. Microwave Theory Tech., vol. MTT-16, pp. 529–535, Aug. 1968.
[8] K. S. Cole and R. H. Cole, "Dispersion and absorption in dielectrics," J. Chem. Phys., vol. 9, pp. 341–351, Apr. 1941.
[9] B. Lax and K. Button, Microwave Ferrites and Ferrimagnetics. New York: McGraw-Hill, 1962, ch. 10.
[10] R. E. Collin, Field Theory of Guided Waves, second ed. New York: IEEE Press, 1991, ch. 6
[11] S. Ramo, J. R. Winnery, and T. Van Duzer, Fields and Waves in Communication Electronics, second ed. New York: Wiley, 1984, ch. 8.
[12] R. F. Harrington, Time-Harmonic Electromagnetic Fields. New York: McGraw-Hill, 1961, ch. 4.
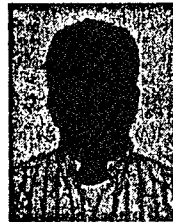
Héctor H. Fiallo was born in Ecuador, in September 12, 1962. In 1987, he received the electrical engineering Diploma with summa cum laude from the Escuela Politécnica Nacional in Quito, Ecuador. He joined the Solid State Science Department at The Pennsylvania State University in January 1990. In 1991, he received a Master of Science Degree in Solid State Science. Having fulfilled all the requirements, he received the Ph.D. degree in solid state science from Penn State in December 1993. Nowadays, he is working at the Applied Research Division, TDK Corporation, Jap..

He was granted a teaching assistance position at the Escuela Politécnica Nacional in 1986. In 1987, he became a lecturer in Network Analysis in the Electrical Engineering Department in the mentioned university. While being a faculty member, he also participated in the redesign and reconstruction of a Satellite Tracking Station in Ecuador, in 1989. In 1991, he was appointed as a research assistant at the Materials Research Laboratory. His research interests are the study of materials for electronic packaging applications: measuring, characterization, and modeling.

Fiallo has been awarded the Adean Peace Scholarship in 1990, and the Organization of American States scholars in 1992. Mr. Fiallo has given several talks at professional meetings. He has also written several technical articles that have been published in the specialized journals.

Joseph P. Dougherty received the B.E.E. degree from Villanova University and was elected a member of Eta Kappa Nu. He received the M.S.E.E. and Ph.D. degrees from Penn State University.

He is Associate Professor of Materials and Director, Center for Dielectric Studies at the Pennsylvania State University, State College, PA. From 1973 to 1979, he was a research scientist at Philips Laboratories in Briarcliff Manor, New York including 1 1/2 years at Philips' Central Research Labs in the Netherlands. He then joined Gulton Industries as Director of Engineering for the Piezoelectric Division and later for Electronic Products in the Electro-Voice division. Five years prior to joining Penn State in 1988, he formed Advanced Materials Technologies, a consulting firm specializing in electronic ceramics. He holds three patents and has co-authored more than 40 papers and parts of five books.

Dr. Dougherty is a member of the IEEE UFFC Society, the UFFC Committee on Ferroelectrics, and the CHMT Society. He is a co-author of the IEEE Standard on Ferroelectric Definitions and an Associate Editor of the UFFC TRANSACTIONS. He is a Fellow of the American Ceramic Society and a member of the ACerS Electronics Division Steering Committee and has been co-chair of the Government Liaison Committee's technical subcommittee. He is also a member of ISHM and ASM.

Sei-Joo Jang received the B.S. degree (cum laude) in electrical engineering from Sogang University in 1973, the M.S. degree in physics from Boston College, and the Ph.D. degree in solid state science from Penn State University in 1979.

He is an Associate Professor of Materials and Senior Research Associate at The Pennsylvania State University, State College, PA. From 1979 to 1983, he was a member of research staff at AT&T Bell Laboratories. In 1983, he joined Penn State University. His research interest in the fields of dielectrics and piezoelectrics are: relaxor materials for capacitors; electrostrictive materials and piezoelectric materials for actuators and transducers; microwave measurements and materials. He is also interest in optical properties of materials: multi- and single-mode fibers; fibers for sensors; electro-optics; optical characterizations and properties. His interest in devices embraces the study of: actuators, micro-positioners, motors, microwave-beam reflectors, -lens, -phase shifters, bimorphs, hydrophones, high temperature transducers (for NDT), piezoelectric devices, pyroelectric sensors, and tactile sensors. He has authored and co-authored more than 75 papers.

Dr. Jang is a member of the American Ceramic Society, the National Institute of Ceramics Engineers, the Optical Society of America, and the ISHM. He has received the 1979 Xerox Research Award, and the 1982 Honorary Mention from the Bell System Best Paper Selection Committee. He is also listed in *American Men and Women of Science*.

Lynn A. Carpenter (M'72) was born in Cushing, OK, on April 25, 1943. He received the B.S. degree in physics from Oklahoma State University in 1964 and the M.S. and Ph.D. degrees in Physics from the University of Illinois at Urbana Champaign in 1966 and 1971.

He is an Associate Professor of Electrical Engineering at the Pennsylvania State University, University Park, PA. His research interest in microwave and radar systems includes work on MMIC design and test and CAD applications of amplifiers, mixers, and oscillators. He recently was on sabbatical at the Applied Physics Laboratory, Johns Hopkins University in the Space Department working on MMIC and dielectric resonator oscillators. He has help develop several CAD programs such as RESOMICS by Murata Erie, State College and CASCADE by Amplifonix.
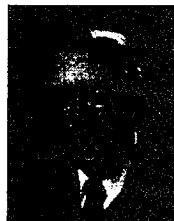
Robert E. Newnham received the B.S. degree in mathematics from Hartwick College, the M.S. degree in Physics from Colorado State University, the Ph.D. degree in physics and mineralogy from Penn State University, and the Ph.D. degree in crystallography from Cambridge University.

He is Alcoa Professor of Solid State Science at the Materials Research Laboratory of the Pennsylvania State University. He served as Chairman of the program for 18 years. He is also affiliated with the Ceramic Science Section of the Materials Science and Engineering Department where he teaches courses in crystal chemistry, crystal physics, and electroceramics. Prior to joining the Penn State faculty, he taught at M.I.T. where he was a staff member of the Laboratory for Insulation Research. His research interests are in structure–property relations, electroceramics, and composite materials for electronic applications. Recently elected to the National Academy of Engineering, he is the author of four books, more than 300 research papers.

Dr. Newnham is now serving as co-editor of the *Journal of the American Ceramic Society*. He is past president of the American Crystallographic Association, and Distinguished Lecturer for the Ultrasonics, Ferroelectrics, and Frequency Control Section of IEEE. He has served as Program Chairman for the International Symposium on Applications of Ferroelectrics (ISAF) and as Secretary of the International Meeting on Ferroelectrics (IMF-5). He has been an invited speaker at many meetings, especially those concerned with composite transducers and smart materials. In 1990 he was elected Ceramic Educator of the Year by the Ceramic Education Council, and in 1991 received the John Jeppson Medal for "Distinguished, creative and inspiring contributions to ceramic science, technology and education in the area of electronic ceramic materials." In 1992, he received the First International Ceramics Prize from the Academy of Ceramics "for distinguished, creative and exceptional interdisciplinary contributions to the advancement of ceramic science and culture, especially in composite electroceramics, including intelligent ceramics."

APPENDIX 58

Integrated Filters and Overvoltage Protection in Multilayer Ceramic Packaging Materials

J. P. Dougherty, H.H. Fiallo, and M.H. Megherhi

Center for Dielectric Studies, Intercollege Materials Research Laboratory
Pennsylvania State University , University Park, PA 16802

1. INTRODUCTION

Multilayer ceramic interconnects can provide some of the highest packaging densities possible for high performance digital systems. Multifunction multilayer ceramic packages have been investigated as a method of providing both high speed performance and high circuit density.[1,2,3] In order to improve performance, recent materials research has focused on the integration of decoupling capacitors in high dielectric constant layers that can be low temperature cofired with the interconnect layers.[1]

As electronic system interaction becomes common, two parameters become more important, overvoltage protection and electromagnetic noise (EMI) suppression. To address the first point, we now report on the cofired integration of a zinc oxide based varistor with a low fire multilayer capacitor system.

The EMI problems are often solved by the use of low pass filters. By incorporating semiconducting ferrite layers with relaxor ferroelectric capacitor layers, we have been able to model and make multilayer metal-semiconductor-relaxor microstrip lines in a packaging amenable configuration. These microstrip lines can function as 1 GHz low pass filters for EMI protection.

Both the overvoltage layers and the filter layers would typically be placed in the lower layers of a multilayer package, near the input-output pins. This would allow fabrication by cofire, tape transfer or thick film techniques. The proximity to the I/O pins also prevents the interfering electrical signals from getting near to the signal layers of the package.
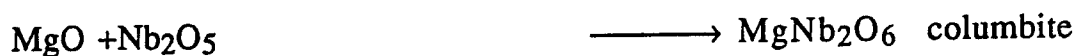
Relaxor ferroelectrics were selected over barium titanate as the dielectric material of choice for both applications [4]. In the overvoltage application, the

PMN based materials can have their firing temperature modified to match ZnO. For the filter needs, the microwave relaxation properties enhanced the device performance.

2. OVERVOLTAGE PROTECTION

Layers of tape cast PMN based relaxor ferroelectric were cofired with layers of conventional Bi doped ZnO. The tape casting and firing methods were the same as those described by Megheri et.al.[1]. There are two key enabling technologies: (1) the Columbite precursor method for preparing fine particle size phase pure perovskite powder[5], (2) the addition if $LiNO_3$ as a sintering aid to lower the sintering temperature below 1000°C.

The chemical reactions involved in the precursor method are:

$$MgO + Nb_2O_5 \longrightarrow MgNb_2O_6 \quad \text{columbite}$$

$$93\ Mg_{1/3}Nb_{2/3}O_2 + .07TiO_2 + PbO \longrightarrow PMN\text{-}7\ PT \quad \text{perovskite}$$

The flow chart for the relaxor preparation is:
1. Batch Materials (MgO and Nb_2O_5)
2. Mill in Ethyl Alcohol (24 hours)
3. Pan Dry (100°C, 24 hours)
4. Calcine (1100°C, 4 hours) XRD to insure phase purity
5. Batch Rest of Materials (PbO and TiO_2)
6. Mill in Ethyl Alcohol (24 hours)
7. Dry and Calcine ((100°C , 24 hours) , (700°C , 4 hours))
8. XRD to insure phase pure Lead Magnesium Niobate-Lead Titanate (PMN-PT)
9. Four wt. percent $LiNO_3$ added as a sintering aid

A pair of tape cast layers of ZnO were sandwiched in a symmetric structure between a pair of PMN-PT layers on top and bottom. (Figure 1a) . The buried electrodes were 70 % Pd - 30% Ag; the structure was cofired in air at 950°C for one hour.
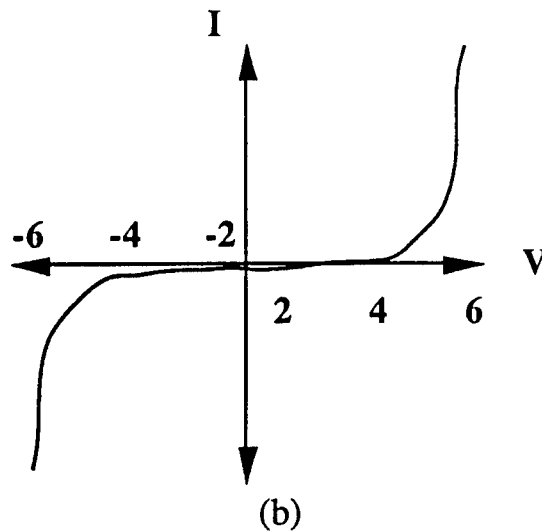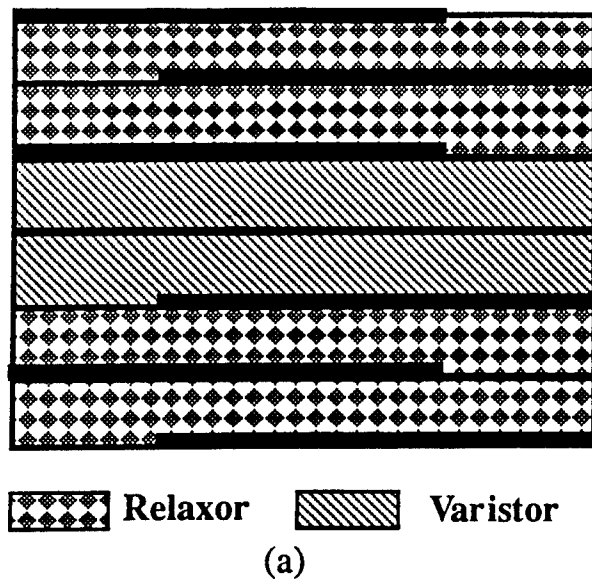
Relaxor   Varistor

(a)   (b)

Figure 1.   (a) Varistor structure and (b) graph of electrical data.

3. INTEGRATED FILTER

Low pass filters can be built into a package by controlling the wave propagation in metal-semiconductor-relaxor microstrip lines.   The microstrip line structure is selected because it is a naturally occurring structure in packages.   Figure 3 shows the placement of the microstrip line in the package and the details of the structure.

The transmission characteristics of the multilayer ferrite-high-K microstrip lines have been calculated by means of the parallel-plate waveguide approximation.   The detailed mathematics of the modeling of the transmission characteristics of metal-semiconductor-relaxor microstrip lines are given in Fiallo 1993[6] and Fiallo et. al.[7]; a summary is given below.

The solution of the complex propagation constant and the characteristic impedance for the parallel-plate waveguide equivalent requires the solution of the wave equation for a non-TEM mode.   In fact, the solution can be obtained by using the techniques for solving surface-wave modes, i.e., LSE, LSM modes.   The LSE mode or TM to y mode has been solved in this case.   The solutions for these types of modes can be found elsewhere in the literature[8,9].   The solution starts with the eigenvalue characteristic equations for each layer, which are given by:
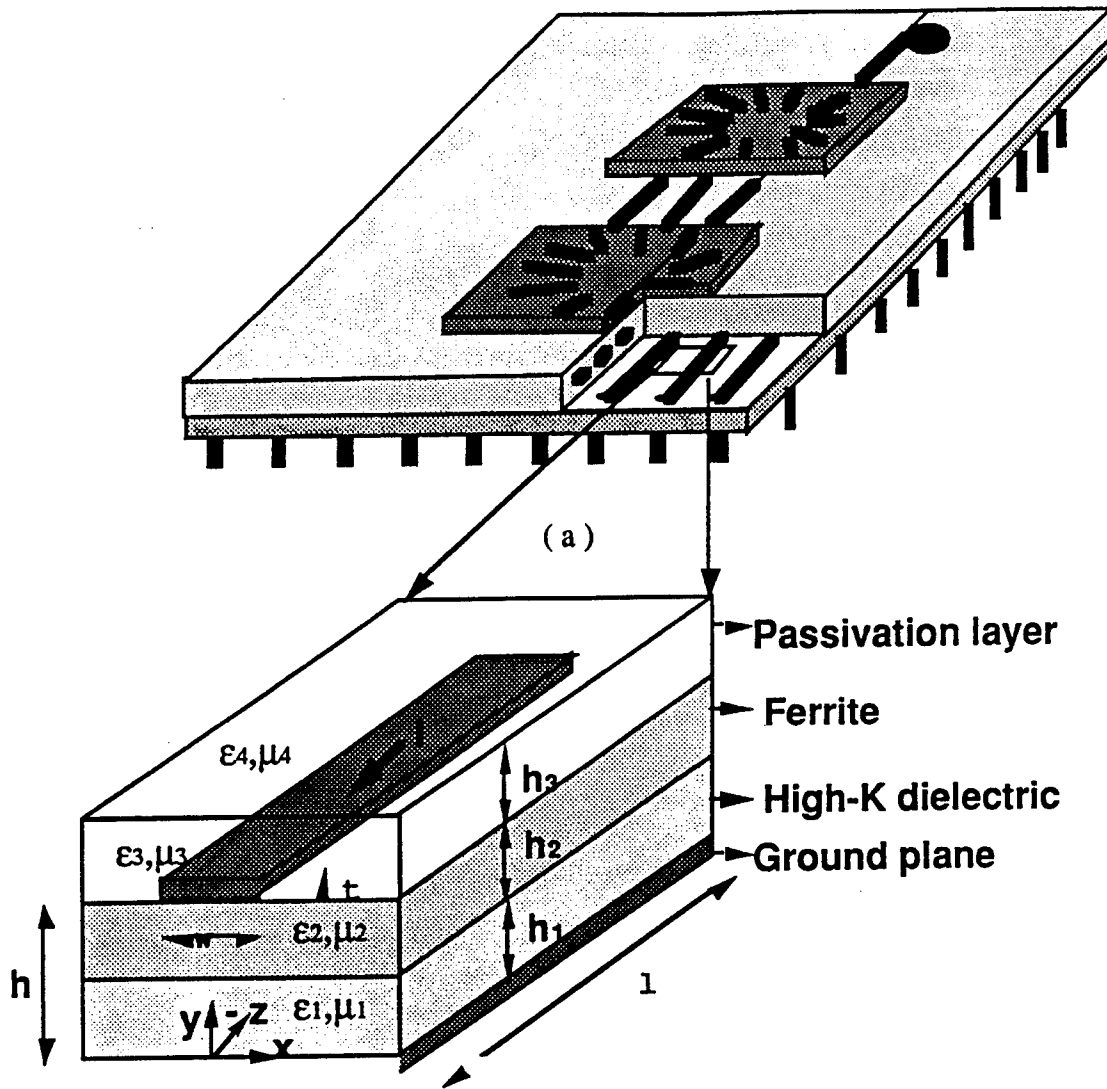
Figure 3 (a) Placement of the multilayer filter in the package, (b) the region treated as a multilayer microstrip line. Notice the layer thicknesses, identification, and axes orientation. $\varepsilon*$ and $\mu*$ are the complex relative permittivity and permeability respectively.

$$\gamma_{y_1}^2 + \gamma_z^2 = -\omega^2 \varepsilon_o \mu_o \varepsilon_1^* \mu_1^* \tag{1}$$

$$\gamma_{y_2}^2 + \gamma_z^2 = -\omega^2 \varepsilon_o \mu_o \varepsilon_2^* \mu_2^* \tag{2}$$

$$\frac{\gamma_{y_1}}{\varepsilon_1^*} \tanh(\gamma_{y_1} h_1) + \frac{\gamma_{y_2}}{\varepsilon_2^*} \tanh(\gamma_{y_2} h_2) = 0 \tag{3}$$

where eq. 3 is the continuity condition at the interface and γ_{yi} is the i-th propagation constant in the y direction for the TM-y mode, γ_z is the

complex propagation constant in the z direction. ε_i^* and μ_i^* are the frequency dependent complex permittivity and permeability of the i-th layer respectively. The axis orientation is shown in figure 3.

Equations 1 and 2 can be reduced to an eigenvalue equation for γ_{yi}, the equation to solve is:

$$\gamma_{y1}^2 - \gamma_{y2}^2 + \omega^2 \varepsilon_o \mu_o (\varepsilon_1^* \mu_1^* - \varepsilon_2^* \mu_2^*) = 0 \qquad (4)$$

The last term of the left hand side of this equation represents the propagation constant of the structure. It can be seen that the propagation constant is not a function of the geometry of the sample[10]. It depends on the dielectromagnetic properties of the layer materials. The relaxation behavior of the dielectric permittivity and permeability have been taken into account by using Cole-Cole and Maxwell-Wagner relaxation models derived from experimental measurements of the permittivity and permeability.

The solutions for the propagation constant γ_z are found by solving equations 3 and 4 simultaneously for each frequency. Although it is possible to find a complete solution for this system, the procedure is time consuming and sometimes does not always converge to a solution. Instead, some meaningful approximations are possible based on the analysis the dielectromagnetic spectra of the permeability-permittivity product difference of a pair of materials. Figure 4 shows the permeability-permittivity product difference for a multilayer microstrip line made with layers of nickel zinc ferrite ($Ni_{0.6}Zn_{0.4}Fe_2O_4$) and high permittivity lead magnesium niobate (Pb $Mg_{1/3}$ $Nb_{2/3}$ O_3). Notice that the imaginary part has been plotted as a loss tangent divided by the wavelength in the material. The wavelength is taken into account by using the loss per unit length which is closer to the units of the attenuation in the propagation constant.

The spectrum shows three distinctive regions . Region I where the ferrite acts as a lossy electrode and the wave propagates in the dielectric. Region I is the passband for the filter. Region II is dominated by the relaxation spectra of the materials; the wave propagates with loss in both materials creating a band edge for the filter. Region III is beyond the

relaxation frequency of the relaxor ferroelectric; the wave propagates with very high losses in the ferrite layer. This is the cutoff region of the filter.
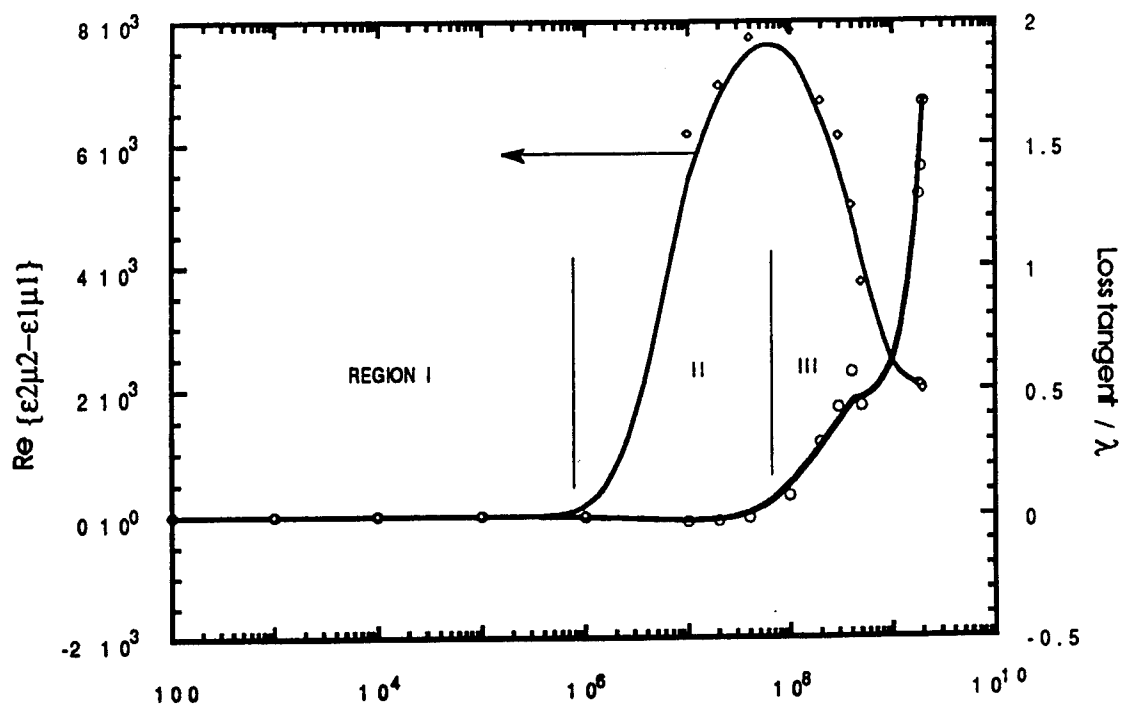

Figure 4   Real part and loss tangent per unit wavelength of the permittivity-permeability product difference for a metal-semiconductor-relaxor microstrip line made of layers of $Pb(Mg_{1/3}Nb_{2/3})O_3$ and $Ni_{0.6}Zn_{0.4}Fe_2O_4$.

From these results we see that the ferrite material defines the cutoff frequency or bandwidth region of the filter, while the relaxor material defines the frequency sensitivity of the imaginary part of propagation constant, i.e., the characteristic impedance, and the harmonic distortion.

4. EXPERIMENTAL DATA

Samples of the structure of interest were prepared by gluing together layers of nickel zinc ferrite ($Ni_{0.6}Zn_{0.4}Fe_2O_4$), and lead magnesium niobate ($PbMg_{1/3}Nb_{2/3}O_3$) relaxor ferroelectric. The layers were tape cast and sintered using the same methods as for the overvoltage protection

multilayers. The adhesive was either epoxy resin or air dry silver paste. The dielectromagnetic characteristics and the thicknesses used as input for the model are given in the figure caption.
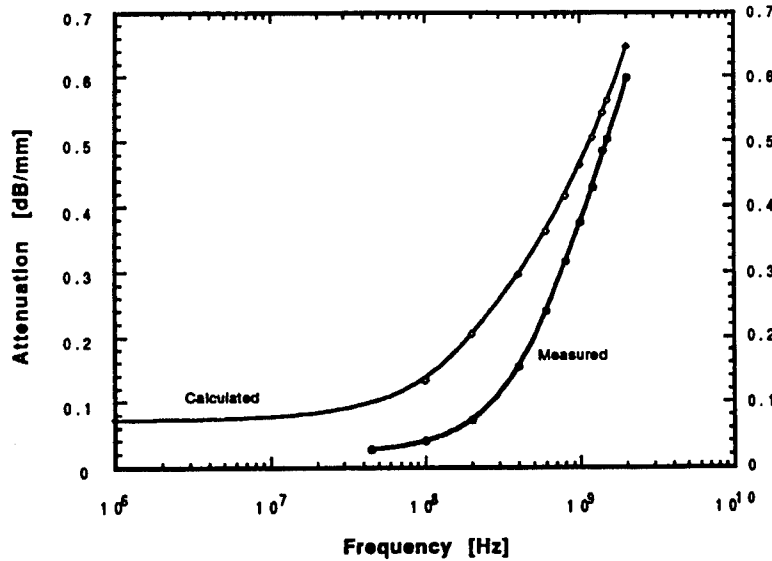

Figure 5. Experimental and measured values of attenuation (given in dB/mm) for a $Ni_{0.6} Zn_{0.4} Fe_2 O_4$ and $Pb Mg_{1/3} Nb_{2/3} O_3$ sample with dimensions: h1=100 mm, h2 = 500 mm, w = 1000 mm. The following values were kept constant for both the samples and the simulations: $\epsilon1(0)=9532.3$; $\epsilon1(\infty) = 1029.3$; $\epsilon2(0) = 263.1$; $\epsilon2(\infty) = 15.96$; $\sigma1 = 0.01 \times 10^{-7}$ Ω-m)-1; $\sigma2 = 246.00 \times 10^{-7}$ $(\Omega$-m)-1; t1 = 8.162 10^{-10}; t2 = 1.59 $\times10^{-8}$; m1(0) = 1; m1(∞) = 1 ; m2(0) = 985.00 ; m2(∞) = 5.78 ; tm1 = 10^{-12}; tm2 =1.591 $\times10^{-9}$.

It can be seen that the calculated and experimental values are below 10% in the high frequency region but larger than 20% at low frequencies. The large error in the low frequency side is probably due to the fabrication method which creates a layer(epoxy) that was not accounted for in the calculations. In any case, it is important to notice that the shape of the low-pass filter characteristic is very similar in the two traces. The data suggest that the model gives results that are reasonably accurate especially if we consider that some attenuation factors have not been taken into account, i.e., conductor losses, and radiation losses. The results demonstrate that these lines can be used as very small size delay lines and

low-pass filters that can be tuned by adjusting the layer thickness ratio, the resistivity of the semiconductor layer, and the difference between the permittivity-permeability product of each layer.

REFERENCES

1. M.H. Megherhi, J.P. Dougherty, G.O. Dayton, and R.E. Newnham, "Electrical properties of co-fired high and low dielectric constant multilayer package materials," Proceedings of ISAF'90, Seventh International Symposium on the Applications of Ferroelectrics, IEEE Press (Nov 1991)

2. Shimada, Y., Y. Yamashita, and H. Takamizawa, "Low Dielectric Constant Multilayer Glass-Ceramic Substrate with Ag-Pd Wiring for VLSI Package," IEEE Trans. Hybrids, Manuf. Tech., 11 [1], p. 163 (1988).

3. Shimida Y., K. Utsumi, T. Ikeda, and S. Nagasako, "Monolithic Multi-Components Ceramic (MMC) Substrates," Proceedings of international Microelectronics Conference, Tokyo, Japan, 227-234 (1984).

4. T.R. Shrout and J.P. Dougherty, "Lead Based $Pb(B_1B_2)O_3$ Relaxors vs $BaTiO_3$ Dielectrics for Multilayer Capacitors," Ceramic Transactions, Ceramic Dielectrics: Composition, Processing, and Properties, American Ceramic Society, Columbus, OH, 8: 3-19 (1990).

5. S.L. Swartz and T.R. Shrout, "Fabrication of Perovskite Lead Magnesium Niobate," Mat. Res. Bull. 17:1245-1250 (1982).

6. Fiallo, Hector H., Ph.D. Thesis, "Multilayer Metal-Semiconductor-Relaxor Microstrip Line Low-Pass Filters for Communication and Wireless Electronic Applications: Design, Materials Selection, and Characterization," The Pennsylvania State University

7. Fiallo, H.H., J.P. Dougherty, S.J. Jang, R.E. Newnham, and L. Carpenter, IEEE Trans., Microwave Theory & Tech., July 1994.

8. Collin, R. E., Field Theory of Guided Waves, second ed., IEEE Press, 1991, Ch. 6.

9. Ramo, S., J. R. Winnery, and T. Van Duzer, Fields and Waves in Communication Electronics, second ed. Wiley, 1984, Ch. 8.

10. Bogar, Jerry H., and Emerson M. Reyner, "Miniature Low-Pass EMI Filters", Proceedings of the IEEE, Vol. 67, No. 1, Jan. 1979, pp. 159-163

PROCESSING STUDIES

APPENDIX 59

ELECTRORHEOLOGICAL PROPERTIES OF BaTiO3 SUSPENSIONS

DAVID V. MILLER*, CLIVE A. RANDALL, AMAR S. BHALLA,
ROBERT E. NEWNHAM and JAMES H. ADAIR**

Materials Research Laboratory, The Pennsylvania State University

ABSTRACT

Electrorheological (ER) fluids based on a silicone oil matrix with a high dielectric constant particulate component, $BaTiO_3$, were evaluated. Particle size effects were examined with a commercial $BaTiO_3$ (0.35µm in size) and a hydrothermally prepared $BaTiO_3$ powder with an average particle size of 0.07µm. The commercial powder exhibited an ER response to DC fields, but above a critical field strength rheological properties dropped off drastically. The relative magnitude of yield stresses, at field levels below the critical field strength, are comparable with current literature values. Hydrothermally prepared $BaTiO_3$ powder exhibited minimal ER response to applied DC fields.

Optical microscope studies of dilute suspensions (~1-2 volume percent) were used to correlate fibril formation with ER measurements. Under applied DC fields, turbulent flow dominated above 6.25kV/cm and ER properties diminished. Increased frequency led to an increase in the degree of fibril formation with a maximum level occurring around 60Hz.

In response to AC fields, both types of $BaTiO_3$ powders showed a strong frequency dependence. Maximum shear stress for a given field strength resulted at about 60Hz. Optical microscopy showed an increase in fibril formation with increased AC field strength (60Hz). Turbulent flow did not appear with increased AC field (60Hz) at all field strengths evaluated ($\leq$20kV/cm). All suspensions exhibited a linear relationship between yield stress and the square of applied electric field, which is characteristic of dipole-dipole interactions.

* Current Address: Loral Vought Systems, Dallas, TX
** Current Address: Materials Science and Engineering, University of Florida, Gainesville, FL

141

1.0 INTRODUCTION

ER fluids have long been of interest to the automotive industry especially for potential applications as fluid clutches and engine mounts[1-6]. At present, however, ER fluids are limited by insufficient yield stresses, suspension stability, reproducibility as a function of time and temperature, and power consumption considerations. In a recent theoretical paper, Davis pointed out that high dielectric constant particles may be a solution to some of these limitations[7]. Previous theoretical models for ER fluids are based on dipole-dipole electrostatic theory in which the attractive force between adjacent particles, subjected to an electric field, is given by[8-11]:

$$F \ = \ \frac{24a^6\varepsilon_o E^2}{R^4} \ \frac{K_f(K_p - K_f)^2}{(K_p + 2K_f)^2} \tag{1}$$

where,

a = equivalent particle radius (m)
r = particle separation distance (m)
ε_o = permittivity of free space
E = electric field (V/m)
K_f = dielectric constant of matrix phase
K_p = dielectric constant of suspended particulates

This model explains the relationship between yield stress and E^2, but more recent work shows that the dependence of yield stress (τ_y) on dielectric constant differences between the particle and fluid components are not following equation (1)[7,12,13].

Based on these observations, the design of new ER fluids with high dielectric constant particles warrants further investigation. This study characterizes fibril formation and yield stress behavior of an ER fluid containing $BaTiO_3$ particles in silicone oil. $BaTiO_3$ was chosen for its high dielectric constant, and silicone oil was used because of its high electrical breakdown strength. Dynamic yield stress values were determined by extrapolation of shear stress to zero shear rate with constant applied field. The relative magnitude of yield stress for $BaTiO_3$ systems is shown to be higher than that predicted by dipole-dipole theory[12].

2.0 EXPERIMENTAL PROCEDURES

2.1 Electrorheological (ER) Measurements

The two $BaTiO_3$ materials evaluated differed in preparation technique and particle size. One system is a coprecipitated, calcined $BaTiO_3$‡ with a mean particle size of

‡ Grade HPB, TAM Ceramics, Niagara Falls, NY

0.35μm. The other $BaTiO_3$ powder was produced by hydrothermal synthesis (designated as BTH8) and possessed a mean particle size of 700Å[14]. Solid loadings, in silicone oil[*#], for the two systems were established from zero field limitations of the viscometer. The useful solid loadings for the commercial powder and BTH8 were determined to be 27 and 12.5 volume percent, respectively.

ER measurements were performed in a modified commercial viscometer[†] on suspensions consisting of $BaTiO_3$ powder and silicone oil using several different loadings. The magnitude and frequency of the applied electric field was controlled with a power supply[□] and an AC signal generator[±]. Shear rates were varied from 93-4.65sec^{-1}. DC field response and upper field limitations were measured at various loadings for two different powders. AC field response was determined up to 18.75kV/cm and frequencies ranging from 10Hz-1kHz for the same suspensions evaluated under DC conditions. An operating frequency of 60Hz was determined optimum for both particle sizes examined, and was used in all AC measurements.

2.2 Optical Microscopy Observations

Fibril formation under applied DC and AC fields was observed using an optical microscope. Suspensions were diluted to 1-2 volume percent solids and loaded in a sample cell. The sample cell was connected to the same power supply and AC signal generator used for ER measurements.

After loading a suspension into the sample cell, a pre-selected field was applied, and response of the suspension was observed with a microscope. The response was monitored on a video recorder for later viewing. Fibril formation was observed under both DC and AC fields as a function of frequency.

3.0 Results and Discussion

3.1 ER Measurements

3.1.1 Zero Field Viscosity

Figure 1 is a plot of shear stress (Pa) as a function of shear rate (sec^{-1}) for TAM HPB/silicone oil suspensions at various solids loadings. These data show a steady increase in zero field viscosity with increased solids loading at all shear rates. Pure silicone oil (50mPa·sec) and the 10 volume percent TAM HPB suspension display results characteristic of Newtonian fluids with

---

[*#] SF 96/50 Thomas Scientific

[+] Brookfield Engineering Labs, Inc., Stoughton, MA

[□] TREK, Model 620A, Medina, NY

[±] Racal-Dana, High Voltage Sweep Generator - F47, Anaheim, CA
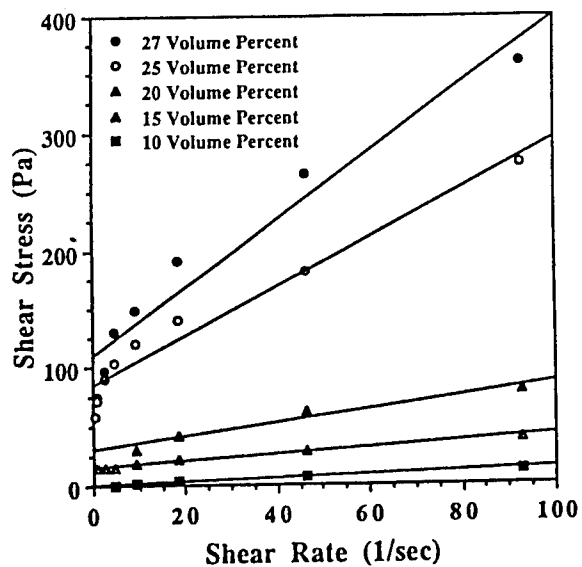
[◊] Zeiss Axioskop, Thornwood, NY

Figure 1 - Shear stress as a function of shear rate for TAM HPB/silicone oil suspensions.
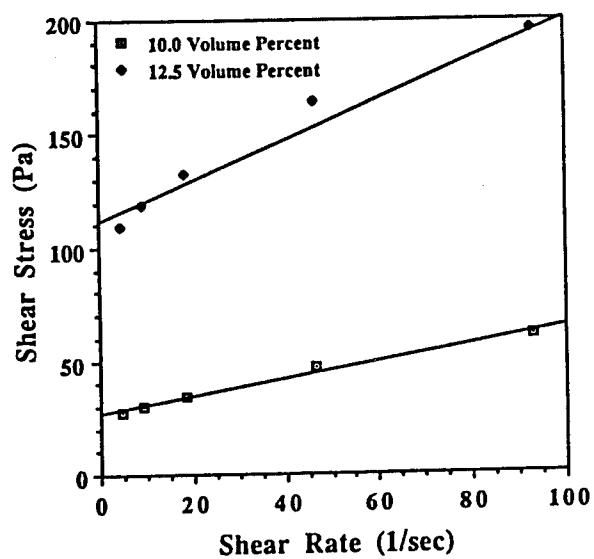

Figure 2 - Shear stress as a function of shear rate for BTH8/silicone oil suspensions.

constant viscosity as a function of shear rate. In contrast, suspensions with solids loadings ≥15 volume percent exhibited Bingham behavior with a finite yield stress (τ_y) and shear thinning behavior.

Figure 2 shows viscosity as a function of shear stress (Pa) for silicone oil with 10 and 12.5 volume percent BTH8. These data demonstrate that at both solid loadings, there is a large zero field viscosity. This is expected because BTH8 has a much higher surface area than TAM HPB and agglomeration is high at low solids loadings. The curves show that BTH8/silicone oil suspensions at these solids loadings possess Bingham behavior. BTH8/silicone oil suspensions up to 12.5 volume percent solids were examined. Above this loading level, the zero field viscosity was too high to measure rheological behavior.

3.1.2 ER Response with DC Fields

Figure 3 shows a linear relationship between τ_y and the square of applied DC field (V/cm) at solids loadings from 10 to 25 volume percent. All TAM HPB/silicone oil suspensions demonstrated a well defined ER effect, but a limit for the applied DC field was observed (6.25kV/cm). Above this limit there was a rapid decrease in viscosity back to the zero field level. Suspensions prepared from the hydrothermally prepared powder (BTH8) exhibited a weak ER effect with applied DC field, and the viscosity decreased rapidly at field strengths above 4kV/cm. The underlying reasons for this limiting field behavior will be discussed in detail with respect to the optical microscopy observations.

3.1.3 ER Response as a Function of Applied Field Frequency

Figure 4 shows a typical frequency response of TAM HPB and BTH8 suspensions in silicone oil (k=2.8). Frequencies were varied from 10Hz-1kHz to establish an optimal frequency for all solids loadings. Optimum frequency varied from 20-100Hz, depending on the powder utilized and operating field. With an operating frequency greater than the optimum frequency, it was difficult to create coherent fibrils between the electrodes. With low frequency AC fields, results similar to applied DC fields were obtained and a maximum applied field strength observed. From these data it was determined that 60Hz should be used in all AC measurements, because maximum viscosity levels were observed around this frequency for all suspensions. Prior work on BaTiO₃ suspensions showed frequency dependent ER response in solvents with high dielectric constant (k=12) and high conductivity[12]. Apparent yield stress increased with increasing frequency, and reached a maximum above 10^3 Hz.

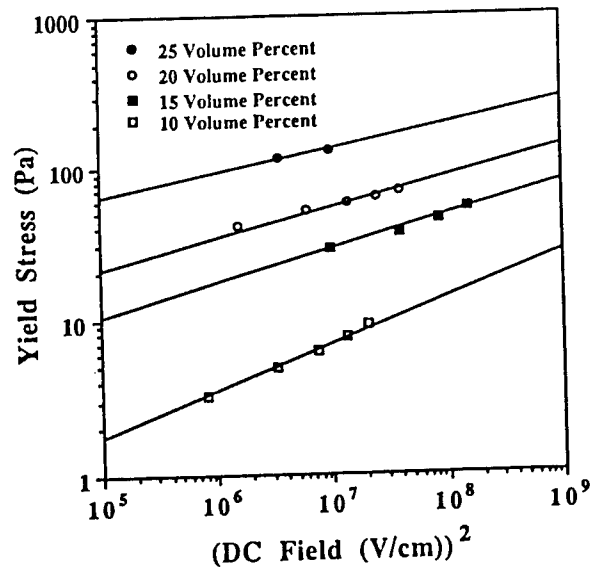Figure 3 - Yield stress as a function of the square of applied DC field for TAM
HPB/ silicone oil suspensions

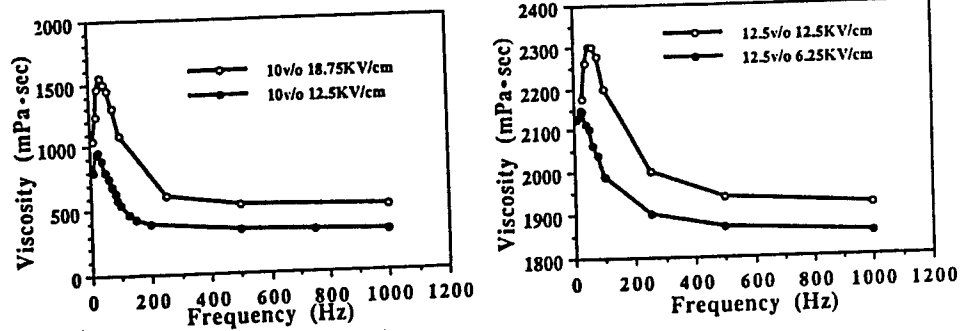(a)   (b)

Figure 4 - Viscosity as a function of frequency (Hz) for silicone oil suspensions
with (a) 10 volume percent TAM HPB and (b) 12.5 volume percent
BTH8.

3.1.4 ER Response with Applied AC Field (60 Hz)

Yield stress plotted as a function of E^2 (figure 5) reveals the linear relationship typical of ER fluids. The relative magnitude of yield stress measured here is in good agreement with previous work on $BaTiO_3$/dodecane ER fluids evaluated at 400Hz[12]. The yield stresses are greater than those predicted by equation (1), but less than the finite element model developed by Davis[7]. Reasons for these disparities are not fully understood at this time.

3.1.5 Particle Size Effects

Figure 6 shows the AC response for BTH8/silicone oil suspensions at two different solid loadings. These results show a trend similar to the commercial powder suspensions of equal solid loadings, but yield stress magnitudes are not as great. These results follow dipole-dipole theory predictions that a decreased particle size will result in a reduced yield stress. This indicates that nanosized particles are not of any particular advantage for enhancing ER properties such as yield stress. Thus, even though nanosized particles may be beneficial to hinder particle settling, if well dispersed, they do not lead to enhanced ER properties in the $BaTiO_3$/silicone oil system.
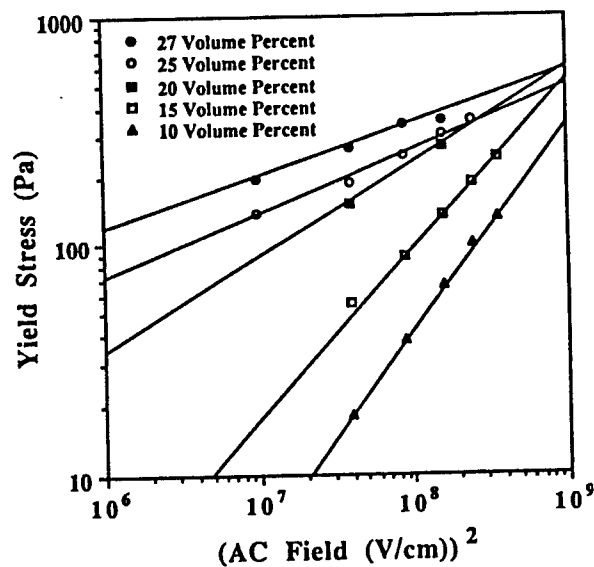

Figure 5 - Yield stress as a function of the square of applied AC field (60 Hz) for TAM HPB/silicone oil suspensions.
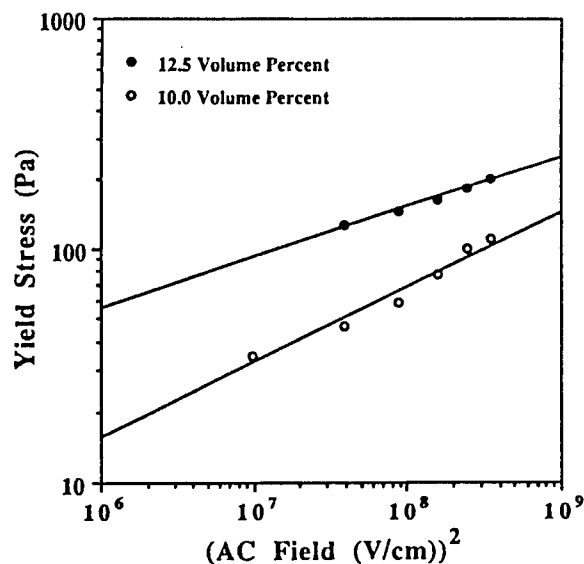
Figure 6 - Yield stress as a function of the square of applied AC field (60 Hz)
for BTH8/silicone oil suspensions.

3.1.6   Field Effects on Fibril Formation

Optical microscopy observations were consistent with the ER measurements. At 1-2 volume percent loadings it was possible to view particles in suspension and observe the changes with field. It has been shown that solid loading, in the $BaTiO_3$/silicone oil system, does not affect the optimum frequency[15]. This supports the contention that results from these direct observations correspond qualitatively with rheological measurements.

With zero applied field, a random distribution of particles existed with no alignment between electrodes. Increasing the applied DC field, led to an increase in the number and size of fibrils formed between the electrodes (figure 7). When the applied field exceeded 6.25kV/cm, turbulent flow of particles in the suspension was observed (figure 8). The reason for the observed turbulent motion is not fully understood. Possibilities include thermal overturn, and competition between electrophoretic motion and electrically induced forces between adjacent particles.

When an AC field (60Hz) was applied to the low volume loaded suspensions, fibrils formed a network between the electrodes. No particle motion between the electrodes was observed as with applied DC fields. The fibrils persisted at all AC fields examined ($\leq$20KV/cm). The fibril networks tend to coarsen at high fields, and this explains why the viscosity increased continuously.
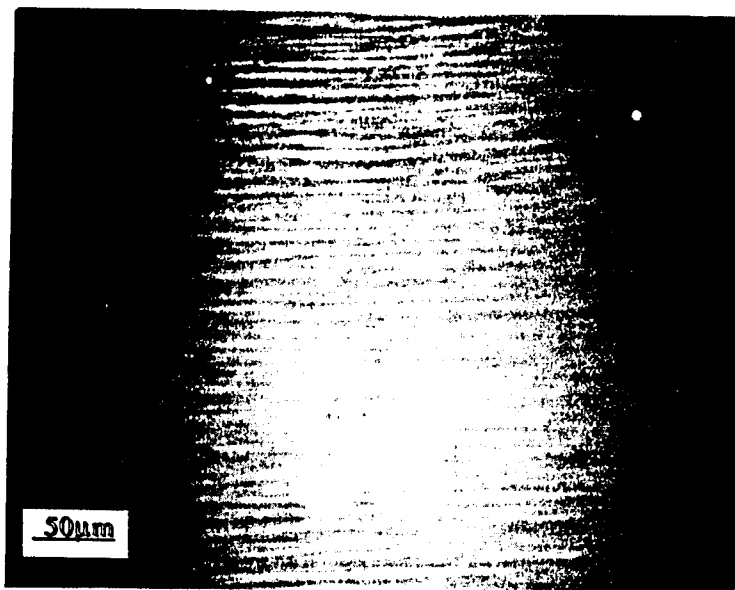
Figure 7 - Optical microscope picture of a TAM HPB/silicone oil suspension
with a 5kV/cm applied DC field.

Removal of the electric field released the fibrils from the electrodes and the
chains slowly dispersed. Agglomerates remained behind when the field was
removed, thus, increasing the zero field viscosity by increasing the number of
particle-particle contacts. Zero field viscosity returned to the original value as the
agglomerated fibril chains dispersed in solution.

Varying the frequency of the applied AC field led to noticeable changes in fibril
formation. At 10kV/cm and low frequencies ($\leq$10Hz), the suspension behaved in a
manner similar to the DC field behavior (figure 8), and turbulent flow prevailed at
high field strengths. At frequencies ranging from 20-70Hz, fibrils formed easily
and were prevalent with increased fields. At high frequencies ($\geq$100Hz), fibrils
were present but were not as well assembled as those produced at 60Hz.

4.0   CONCLUSIONS

BaTiO$_3$ makes a potentially useful component to ER fluids. Yield stresses were
measured under both DC and AC field conditions, typically showing an E^2
dependence on field strength. The maximum yield stresses were found to be a
function of the applied frequency - with the optimum effect near 60Hz for BaTiO$_3$
in silicone oil. Particle size played an important role in the observed properties.
Decreased particle size resulted in a reduced ER effect. The effect of particle size on
ER properties follows the trend predicted from dipole-dipole theory.

Optical microscopy results correlated fibril formation and ER measurements. At high field strengths (>6.25kV/cm), DC or low AC bias (<10Hz), turbulent flow upset fibril formation and reduced the associated ER properties. Fibrils created under an applied AC field (60Hz) did not experience turbulent flow (<20kV/cm).
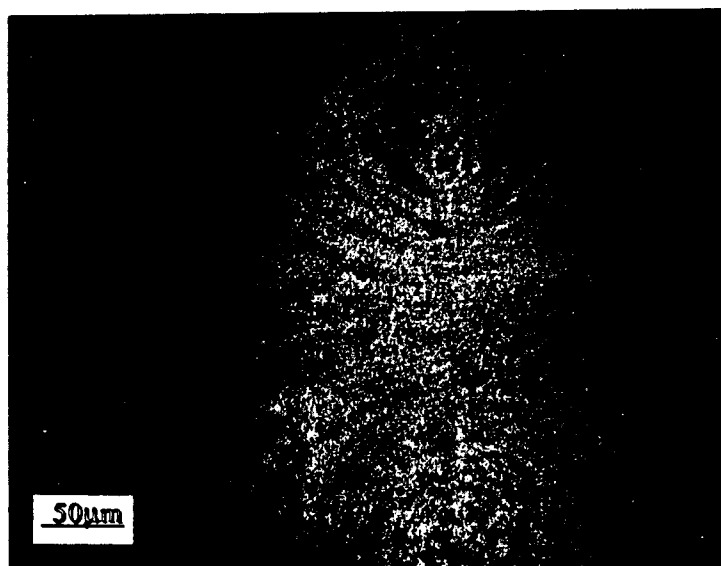

Figure 8 - Optical microscope picture of a TAM HPB/silicone oil suspension with a 10kV/cm applied DC field.

REFERENCES

1. J. D. Carlson, A. F. Sprecher, and H. Conrad (editors), <u>Electrorheological Fluids</u>, Proceedings of the Second International Conference on ER Fluids, Technomic Publishers, Lancaster, PA (1990).

2. D. Scott and J. Yamaguchi, <u>Inter. View.</u>, <u>91</u> [11] 61-66 (1983).

3. M. Bernuchon, <u>Society of Automotive Engineers Technical Paper No. 840259</u> (1984).

4. M. Clark, <u>Society of Automotive Engineers Technical Paper No. 851650</u> (1985).

5. R. Shoureshi, P. L. Graf, and T. L. Houston,<u>Society of Automotive Engineers Technical Paper No. 860549</u> (1986).

6. T. G. Duclos, D. A. Hodgson, and J. D. Carlson, U.S. Patent No. 4,733,758 (1988).

7. L. C. Davis, <u>Appl. Phys. Lett.</u>, <u>60</u> [3] 319-321 (1992).

8. A. R. von Hippel, <u>Dielectrics and Waves</u>, John Wiley and Sons, pg. 39 (1954).

9. H. A. Pohl, <u>J. Appl. Phys.</u>, <u>22</u> [7] 869-71 (1951).

10. H. A. Pohl, <u>J. Appl. Phys.</u>, <u>29</u> [8] 1182-9 (1958).

11. H. A. Pohl and J. P. Schwar, <u>J. Appl. Phys.</u>, <u>30</u> [1] 69-73 (1959).

12. T. Garino, D. Adolf and B. Hance, <u>Electrorheological Fluids</u>, Proceedings of the Third International Conference on ER Fluids, R. Tao (editor), World Scientific Publishers, 167-174 (1991).

13. L. F. Evans, I. H. Harness, P. R. Kermode, and J. E. Stangroom, <u>Electrorheological Fluids</u>, Proceedings of the Third International Conference on ER Fluids, R. Tao (editor), World Scientific Publishers, 154-166 (1991).

14. D.V. Miller, C.A. Randall, A.S. Bhalla and J.H. Adair, to be published.

15. C. Bowen, A.S. Bhalla, R.E. Newnham and C.A. Randall, to be published.

APPENDIX 60

Increased Operating Temperature Range In La-Modified $Pb(Mg_{1/3}Nb_{2/3})O_3$-$PbTiO_3$ Relaxor Ferroelectric-Based Transducers

J. T. Fielding, Jr., T. R. Shrout, and S. J. Jang

Materials Research Laboratory, The Pennsylvania State University, University Park, PA 16802

Abstract-The large E- field induced strains and electromechanical coupling in PMN-based relaxors have been utilized in actuator and transducer applications. The effect of La^{3+} modifications on the field-dependent dielectric and piezoelectric properties was investigated for several (1-x)PMN-(x)PT compositions with transition regions near room temperature. The effect of La^{3+} modifications, increasing the width of the micro-macro polar transition range (ΔT), defined as the difference between the temperature of maximum permittivity (T_{max}) and the depolarization temperature(T_d), results in a broader temperature range for obtaining large induced electromechanical coupling factors with negligible hysteresis.

INTRODUCTION

Electrostrictive materials have been extensively investigated for actuator applications. [1] There has been recent interest in utilizing the field-induced piezoelectric effect in electrostrictive materials for transducer applications such as biomedical imaging.[2] Several families of perovskite-based electrostrictors have been investigated as potential candidates for high frequency transducer applications.[3]

One of the advantages of using certain classes of electrostrictors, such as relaxors, is the anhysteretic strain-field response. This behavior is observed in normal ferroelectrics at temperatures greater than T_c or in relaxors at greater than the depolarization temperature, T_d. The breadth of the micro-macro transition region (ΔT), the difference between the temperatures of dielectric maxima (T_{max}) and depolarization (T_d), indicates a much broader operating temperature range for potential devices. Additionally, the field dependence of the dielectric, piezoelectric and elastic properties allows the tuning of the electromechanical coupling k_{ij} and mechanical Q. Also, the induced electromechanical coupling vanishes upon removal of the electric field, reducing spurious noise, which is important in several transducer applications.

The primary criteria, to induce a large piezoelectric effect, can be achieved by selecting materials in which a large polarization can be produced by the application of an external electric field. The piezoelectric charge coefficient d_{ijk} is defined as follows:

$$d_{ijk} = 2 \chi_{mk} \varepsilon_o Q_{ijmn} P_n \qquad \text{(Eqn. 1)}$$

where χ_{mk}, Q_{ijmn}, and P_n are the dielectric susceptibility, electrostrictive coefficient and total polarization, respectively. Other desirable performance criteria for selecting materials for transducer applications include reproducible piezoelectric coefficients, low losses, rapid response time and a wide operating temperature range.

The relaxor ferroelectric lead magnesium niobate-lead titanate $(1-x)Pb(Mg_{1/3}Nb_{2/3})O_3$-$(x)PbTiO_3$ (PMN-PT) is interesting due to the large polarizations and maximum permittivities, broad anomaly in the dielectric response, and anhysteretic strain-electric field behavior available over a broad range of temperatures reported.

The effects of La_2O_3 and $PbTiO_3$ modifications on the dielectric properties have been previously reported. [4,5,6] The temperature of the dielectric maxima, T_{max}, was reduced approximately 25°C/atom% La. The micro- to macro-polar transition region, ΔT, was observed to increase with increasing La^{3+} additions. The permittivity was also reduced. These effects were thought to be related to an increase in non-stoichiometric ordering of Mg and Nb cations. [4,5]

Additions of PT resulted in a gradual disappearance of non-stoichiometric cation ordering near the morphotropic phase boundary (MPB).[6] The sharpness of the dielectric anomaly, transition temperature T_{max} and depolarization temperature T_d increase with increasing PT content. The maximum dielectric permittivity K_{max} was observed to increase with increasing PT content up to values of x~0.30-0.33, achieving levels >30,000 (@ 1 kHz).[7] The maximum dielectric loss is ~0.10 at 1 kHz and decreases rapidly to values $\leq$ 0.01 at temperatures >T_{max}. ΔT were observed to decrease with increasing PT content, exhibiting a sharp dielectric transition for values of x>0.33 and indicating a change in the relaxor nature with increasing additions of a normal ferroelectric.

In this study, several compositions in each of the families were processed. The field dependent dielectric, piezoelectric and elastic properties were evaluated at frequencies between 100 kHz and 5 MHz and at temperatures in the various polarization regimes of interest.

EXPERIMENTAL

(1-x)PMN-(x)PT powders with 0 and 1 atom% La modifications were prepared using reagent grade oxides. The columbite precursor method was utilized to maximize pyrochlore formation.[9] Batches were formulated and mixed using vibratory milling using deionized H_2O and ammonium polyelectrolyte dispersant. After drying, powders were crushed, using mortar and pestle, and calcined for 4 hours at 700°C. X-ray diffraction analysis was used to ensure proper phase formation. Pyrochlore content measured using XRD was less than 3%. To break up aggregates and reduce particle size, compositions were milled overnight in deionized H_2O with dispersant and dried. 3 wt% acrylic binder (Rohm and Haas Acryloid B-7) was added and powder was sieved -80 mesh prior to uniaxial pressing. Disks with 1.27 and 2.54 cm diameters were pressed at 150 MPa. Binder was removed by heating at 3°C/min. to 300°C and 5°C/min. to 550°C.

Disks were sintered on Pt foil in high density Al_2O_3 crucibles for 2 hours at 1150-1200 °C using a $PbZrO_3$ source powder for controlling PbO volatility. Weight loss and geometric densities were calculated. Specimens were precision lapped to 0.5 mm thickness to produce a dilatational thickness mode resonance ~4.5-5 MHz.

Dielectric property measurements included characterization of the field and temperature dependence of the relative dielectric permittivity and dielectric loss, performed over the frequency range from 0.1 kHz to 100 kHz using capacitance bridges (HP 4274 and 4275) and from 1 to >5 MHz using complex impedance data obtained from an impedance analyzer (HP3577A). Additionally, the polarization versus electric field behavior was examined and compared between families, using P vs. E measurements at several temperatures performed using a Sawyer-Tower circuit. Measurements of the pyroelectric current as a function of temperature was performed using the static Byer-Roundy technique to determine the pyroelectric coefficient, remanent polarization levels and effects of external electric fields on the depolarization temperature T_d in relaxor and normal ferroelectrics.

High frequency field-induced electromechanical coupling factor were obtained from measurements of the series (f_s) and parallel (f_p) resonances, performed using a HP3577A network analyzer with HP35677A S-parameter test set configured for a one-port input reflection technique. Typical applied d.c. bias levels used for the measurements were between 1 and 15 kV/cm. The radial coupling

factor k_p was calculated using a polynomial curve fitting equation.[18]. The dilatational thickness mode coupling factor k_t was calculated using the following equation: [18]

$$k_t^2 = \frac{\pi}{2} \frac{f_s}{f_p} TAN \frac{\pi}{2} \frac{(f_s - f_p)}{f_p} \quad \text{(Eqn. 2)}$$

Several temperature regions were selected for measurement, depending on the material family. For relaxor ferroelectrics, resonance measurements were made over a range from the micro-polar region ($T>T_{max}$) to well below the depolarization temperature T_d.

RESULTS AND DISCUSSION

Dielectric Properties

Large small signal permittivities were observed in unmodified and La-modified PMN-PT compositions. The low frequency dielectric constant and polarization behavior is shown for a 0.90PMN-0.10PT composition in Figure 1a. The temperature dependence of the permittivity and loss for several 1 atom% La-modified compositions is shown in Figure 1b. Values for K_{max} (@ 1 kHz) were 27-36,000 for the PMN compositions investigated. At temperatures above T_{max}, all the families exhibited low losses at 1 kHz. A summary of the dielectric properties for the various families investigated is presented in Table I.

Large polarizations were measured for the Pb-based relaxor families. The micro-macro transition region, ΔT, was 25-45 °C for the PMN-PT relaxor families. The pyroelectric response for several 1 atom% La-modified compositions is shown in Figure 2. The effect of La additions on P and ΔT for varying PT contents is shown in Figure 3. La additions reduced the polarization and increased the micro-macro transition region for the PT contents evaluated.
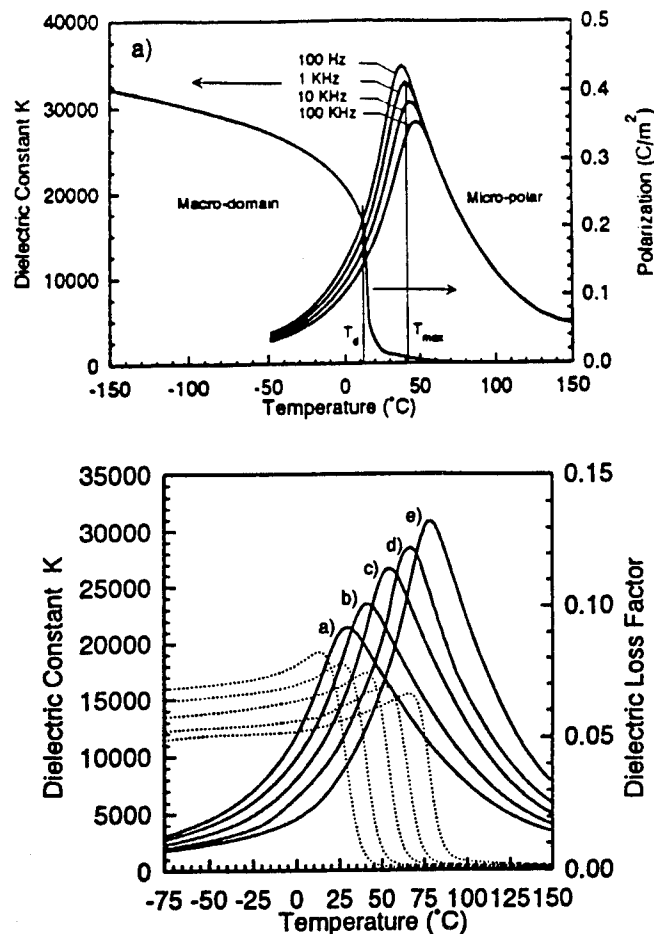

Figure 1. a)Polarization and dielectric constant as function of temperature for 0.90PMN-0.10PT. b) Dielectric constant and loss factor for 1 atom% La-modified (1-x)PMN-(x)PT compositions with x=a) 0.125;b) 0.15;c) 0.175;d) 0.20;e) 0.225.

Table I. Summary of dielectric measurements for several PMN-PT and 1 mol% La compositions.

| x=	1 kHz T_{max} (°C)	1 kHz K_{max}	1 kHz D.F. max.	(@	100 kHz K_{max}	100 kHz D.F. T>Tmax	1 MHz K_{max} 0 kV/cm	1 MHz K_{max} 10 kVcm	1 MHz D.F. T>T$_{max}$	5 MHz K_{max} 0 kV/cm	5 MHz K_{max} 10 kV/cm	5 MHz D.F. T>T$_{max}$
	w/ 0 mole% La$_2$O$_3$											
0.10	40	32,800	0.092	28	28,280	<0.003	26,600	8,700	<0.004	25,200	8,500	<0.005
0.125	52	32,100	0.073	35	28,230	<0.003	26,800	9,000	<0.003	25,600	8,650	<0.004
0.15	68	36,530	0.063	50	32,890	<0.003	30,800	8,500	<0.003	29,600	8,300	<0.004
	w/ 1 mole% La$_2$O$_3$											
0.125	30	21,430	0.082	12	18,930	<0.006	17,650	8,750	<0.006	16,500	7,600	<0.008
0.15	41	23520	0.078	27	20,760	<0.005	19,450	9,100	<0.005	18,300	8,400	<0.008
0.175	55	26,670	0.074	40	23,430	<0.005	23,500	9,450	<0.005	21,700	8,900	<0.008
0.20	66	28,550	0.069	53	25,380	<0.004	24,600	9,800	<0.005	22,300	9,160	<0.007
0.225	78	30,860	0.066	65	27,170	<0.004	26,400	10,100	<0.005	24,100	9,300	<0.007
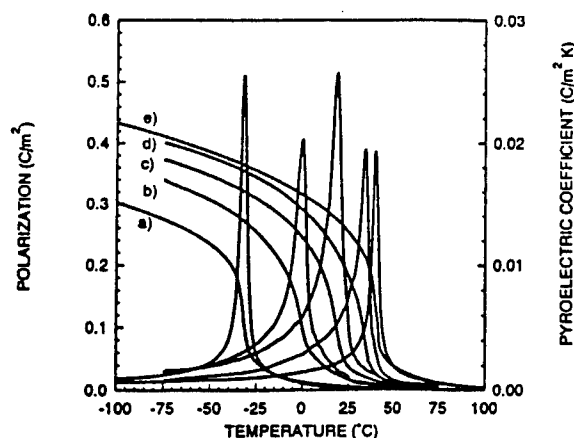
Figure 2. Pyroelectric coefficient and polarization for 1 atom% La-modified (1-x)PMN-(x)PT compositions with x=a) 0.125;b) 0.15;c) 0.175;d) 0.20;e) 0.225.
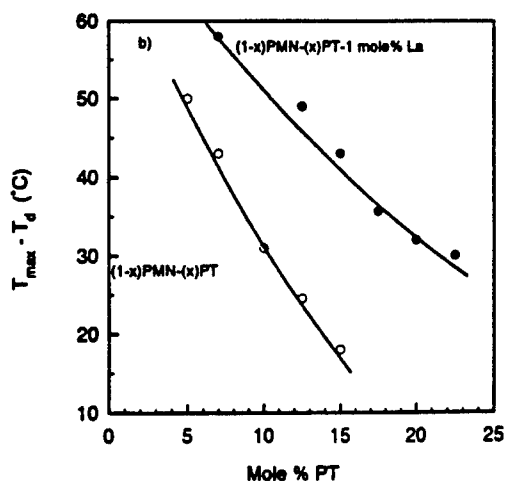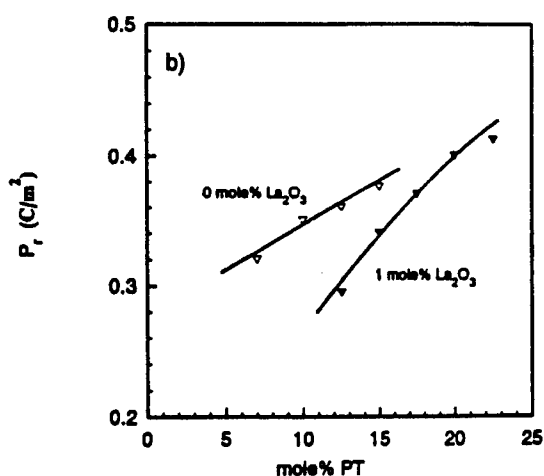
Electromechanical Properties

Large field-induced coupling factors were obtained for PMN-PT compositions evaluated. The field dependence of the coupling factor for a 0.85PMN-0.15PT-1%La specimen at two temperatures, 50°C (T~T$_{max}$), and 75°C(T>T$_{max}$), is shown in Figure 4. There was no remanent k$_t$ observed after field removal for temperatures >T$_d$. The E-field dependence of k$_t$ correlates fairly well with P$_{ind}$ behavior at the measurement temperatures.

The temperature dependence of the field-induced thickness coupling factor k$_t$ is shown in Figure 5 for 0.875PMN-0.125PT and 0.85PMN-0.15PT-1%La at several d.c. bias levels. The La-modified compositions were able to maintain larger electromechanical effect at higher temperatures for comparable E-field levels. The temperature range for inducing large k$_t$'s without remanence was increased due to the downward shift of T$_d$ with 1 atom% La additions. The induced k$_t$ values at 10 kV/cm field levels and remanent k$_t$, normalized to T$_{max}$, for the x= 0.125 and 0.15-1%La compositions, shown in Figure 6, illustrate the effect of La additions.

Figure 3. Effect of PT on polarization and ΔT for 0 and 1 %La modified PMN-PT ceramics.
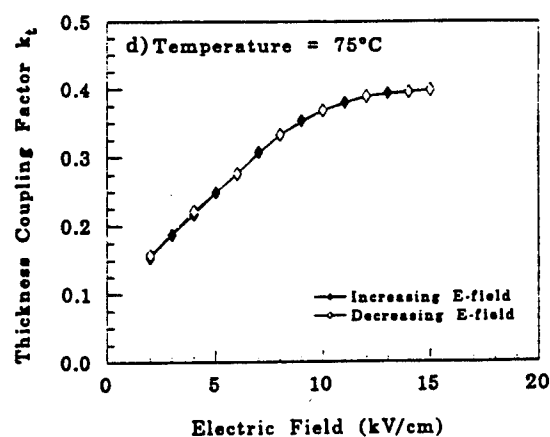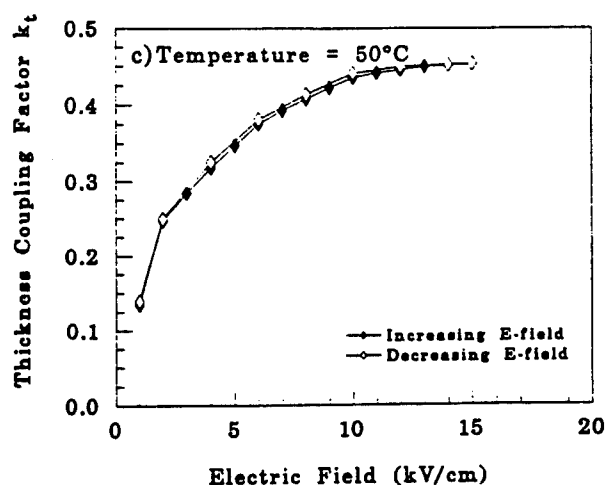

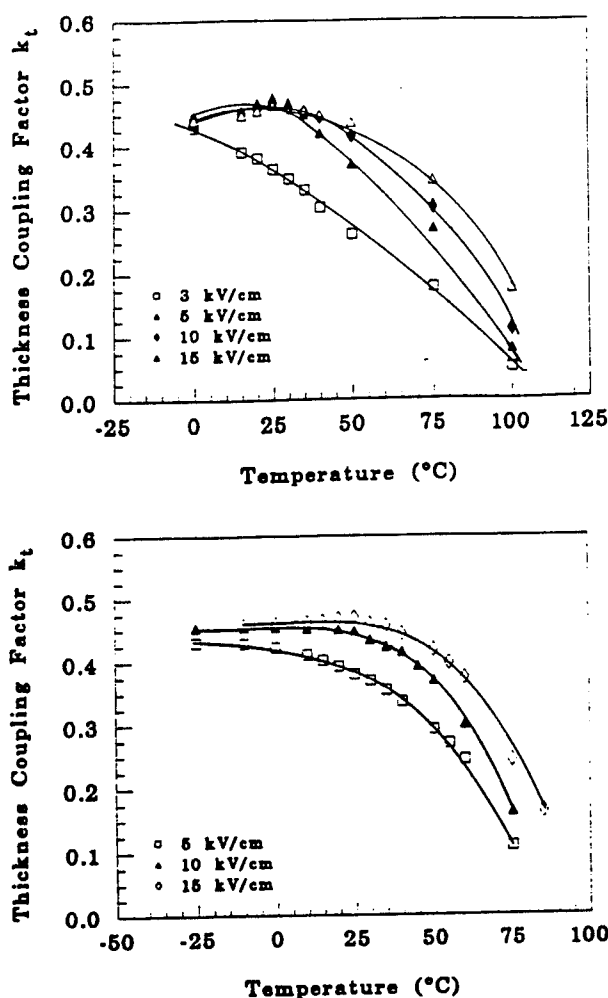Figure 4. Field-dependence of induced thickness coupling factor k$_t$ for temperatures a) 50°C and b) 75°C.

Figure 5. Temperature dependence of induced k_t at several field levels for a) 0.875PMN-0.125PT and b) 0..85PMN-0.15PT-1%La specimen.
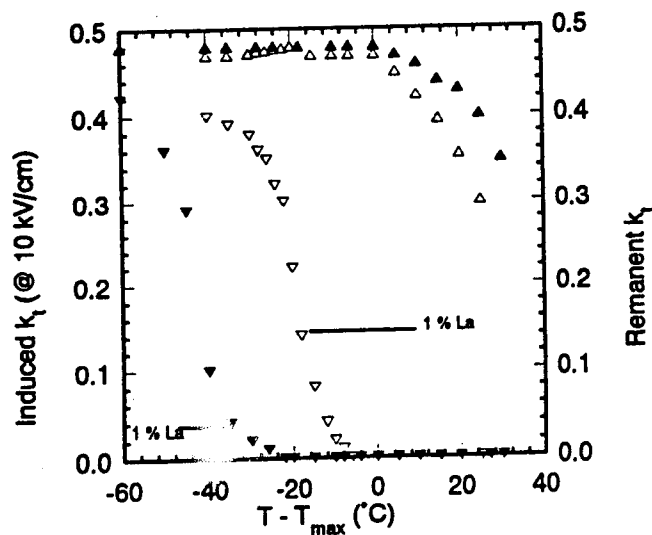
CONCLUSIONS

The effect of La additions to increase the width of the micro-macro transition region in PMN-PT relaxors was investigated. The range for achieving large induced polarizations and electromechanical coupling factors (k_t's 0.47-0.50) increased with 1 atom% La^{3+} additions. The large, tunable k_t values obtained were comparable to those of conventional poled piezoceramics such as PZT.

PMN-PT relaxors offer large K's, low losses, and adjustable induced piezoelectric and elastic properties. However, the strong frequency dependence of the dielectric properties of relaxors may reduce the other advantages in some fixed frequency transducer applications.

REFERENCES

[1] K. Uchino, "Electrostrictive Actuators: Materials and Applications," *Am. Ceram. Bull.*, 65 [4], pp. 647-652 (1986).

[2] H. Takeuchi, H. Masuzawa, and C. Nakaya, "Relaxor Ferroelectric Transducers," *Proceedings of 1990 Ultrasonics Symposium*, 697 (1990).

[3] J. T. Fielding, Jr., "Field-Induced Piezoelectric Materials for High Frequency Transducer Applications," Ph.D. Thesis, The Pennsylvania State University, (1993).

[4] N. Kim, "The Role of Lanthanum Modification on the Fabrication and Properties of Lead Magnesum Niobate-Lead Titanate Ceramics," M.S. Thesis, The Pennsylvania State University (1990).

[5] J. Chen and M. Harmer, "Ordering Structure and Dielectric Properties of Undoped and La/Na doped $Pb(Mg_{1/3}Nb_{2/3})O_3$ Ceramics," *J. Am. Ceram. Soc.*, 72, 593 (1989).

[6] A. D. Hilton

[7] S. W. Choi, T. R. Shrout, S. J. Jang and A. S. Bhalla, "Dielectric and Pyroelectric Properties in the PMN:PT System," *Ferroelectrics*, 100, 29 (1989).

[8] IEEE Standard on Piezoelectricity, ANSI/IEEE Std 176-1978, The Institute of Electrical and Electronic Engineers, Inc., New York (1978).

[9] S. L. Swartz and T. R. Shrout, "Fabrication of Perovskite Lead Magnesium Niobate," *Mat. Res. Bull.*, 17, 1245-1250 (1982).

Figure 6. Induced (@ 10 kV/cm) and remanent k_t values as function of temperature for (1-x)PMN-(x)PT samples with x=0.125 and x=0.15-1%La.

APPENDIX 61

Field-Induced Piezoelectric Materials For 100 kHz-10 MHz Transducer Applications

J. T. Fielding, Jr., S. J. Jang, and T. R. Shrout
Materials Research Laboratory
The Pennsylvania State University, University Park, PA 16802

Abstract- Several electrostrictive materials were investigated as candidates for high frequency transducer applications. Families investigated included $(1-x)Pb(Mg_{1/3}Nb_{2/3})O_3-(x)PbTiO_3$ and PLZT relaxors, and Sr- and Sn- substituted $BaTiO_3$ normal ferroelectrics. The field dependent dielectric, piezoelectric and elastic properties were characterized at frequencies between 100 kHz and 5 MHz. The large magnitude and E-field tunability of the electromechanical and elastic properties observed in several of the materials may present opportunities for several new transducer applications, such as biomedical imaging and non-destructive evaluation.

INTRODUCTION

The usage of piezoelectric ceramics for transducer and actuator applications has increased rapidly in the past decade. Currently, conventional piezoceramics are employed in many mature applications, such as sonar, welding and buzzers. Several families of electrostrictive materials have been investigated for emerging actuator and transducer applications such as micro-positioning and biomedical imaging.[1,2] Desirable performance criteria for selecting materials for transducer applications include large and reproducible induced piezoelectric coefficients, low losses, rapid response time and a wide operating temperature range

The primary criteria, to induce a large piezoelectric effect, can be achieved by selecting materials in which a large polarization can be produced by the application of an external electric field. The piezoelectric charge coefficient d_{ijk} is defined as follows:

$$d_{ijk} = 2 \chi_{mk} \varepsilon_0 Q_{ijmn} P_n \qquad \text{(Eqn. 1)}$$

where χ_{mk}, Q_{ijmn}, and P_n are the dielectric susceptibility, electrostrictive coefficient and total polarization, respectively.

Electrostrictive materials offer several other advantages over piezoceramics for transducer applications. These are compared in Table I.[3,4] The field dependence of the dielectric, piezoelectric and elastic properties allows the tuning of the electromechanical coupling k_{ij} and mechanical Q. Also, the induced electromechanical coupling vanishes upon removal of the electric field, reducing spurious noise, which is important in several transducer applications.

Several material families, solid-solution forming systems having prototype perovskite structures in the paraelectric phase, have been selected as potential candidates for electrostrictive transducer applications. The polarization change mechanisms and general electric field-polarization relations have been classified elsewhere by Cross.[5] Sr substituted barium titanate $(Ba_{1-x}Sr_x)TiO_3$ normal ferroelectrics were selected for several reasons: larger phase transition; larger values of K_{max} compared to $BaTiO_3$; the ability to controllably shift the Curie temperature T_c downwards; and the extensive investigation of the piezoelectric and electrostrictive effects in $BaTiO_3$.[6] Values for the field-induced coupling factors k_{33} and k_p were ~0.5 and 0.3, respectively, at temperatures near T_c.

Sn-substituted barium titanate $Ba(Sn_xTi_{1-x})O_3$ ferroelectrics exhibit "pinching" of the phase stability regions of the rhombohedral, orthorhombic, tetragonal and cubic phases, produced by compositional heterogeneity.[7] Large permittivities ($K_{max} > 25,000$ at 1 kHz) have been reported along with a linear strain-electric field response and large induced piezoelectric coefficient (d_{33} ~650-750 pC/N) at lower E-field levels ($< 5kV/cm$).[8]

Table I. Comparison of selected properties between piezoelectric and electrostrictive materials [3]

Parameter	Piezoelectric	Electrostrictive (Relaxor-based)
Strain/Field dependence	Linear	Non-linear
Field-induced strains	>0.1%	> 0.1%
Hysteresis	Larger (5-30%)	Minimal (< 5%)
Switching speed (μs)	Slower (1->10)	Faster (0.1-10)
Transition temperature (i.e., operating range)	Higher T_{max}	Lower T_{max}
Frequency dependence	Small	Larger
Dielectric Properties	K_{max} 1,000-4,000	K_{max} 15,000-30,000
Electromech. props.	Large, rel. E-field independent	Large, Adjustable $P_{ind}, d_{ij}, k_{ij} \Rightarrow f(E, \omega)$
Aging (%/time decade)	Large (0.5-2.5)	Smaller (0-0.5)

Two relaxor ferroelectric families, lead magnesium niobate-lead titanate $(1-x)Pb(Mg_{1/3}Nb_{2/3})O_3-(x)PbTiO_3$ (PMN-PT) and La-doped lead zirconate-titanate $Pb_{1-x}La_x(Zr_{1-y} Ti_y)_{1-x/4}O_3$ (hereafter referred to as PLZT) were selected due to the large polarizations and maximum permittivities, broad anomaly in the dielectric response, and anhysteretic strain-electric field behavior available over a broad range of temperatures reported.[9] The breadth of the micro- to macro-polar transition region, described by $\Delta T = T_{max} - T_d$, gives an indication of the operating temperature range for potential devices.

In PMN, the transition temperature T_{max} and depolarization temperature T_d increase with increasing PT content.[10] The maximum dielectric permittivity K_{max} was observed to increase with increasing PT content up to values of x~0.30-0.33, achieving levels >30,000 (@ 1 kHz).[10] The maximum dielectric loss is ~0.10 at 1 kHz and decreases rapidly to values ≤ 0.01 at temperatures >T_{max}. The diffuseness of the transition and ΔT were observed to decrease with increasing PT content, exhibiting a sharp dielectric transition for values of x>0.33. These observed effects indicate a change in the relaxor nature with increasing additions of a normal ferroelectric.

Large and adjustable E-field induced piezoelectric coefficients in PMN-PT ceramics at lower frequencies (i.e., < 200 kHz) have been previously reported.[11] At the higher frequencies of interest in this study, Takeuchi reported field-induced thickness coupling factor k_t values of 0.45 for 0.91PMN-0.09PT ceramic specimens, measured at 7.5 MHz.[2]

PLZT compositions near the MPB have been extensively studied for electrooptic applications.[12] The broad dielectric transition, large permittivities (K_{max}'s ~4,000-11,000), and large polarizations (>30 $\mu C/cm^2$) indicate the potential for a large field-induced piezoelectric effect over a broad temperature range. With increasing La content, K_{max} decreases, the transition broadens, and T_{max} and T_d are shifted to lower temperatures. Of interest for actuator and transducer applications, anhysteretic field-induced strains ~2-5.4 x10^{-3} have been reported by several investigators for x/65/35 compositions with x=0.07-0.11.[12]

In this study, several compositions in each of the families were processed. The field dependent dielectric, piezoelectric and elastic properties were evaluated at frequencies between 100 kHz and 5 MHz and at temperatures in the various polarization regimes of interest.

Powders were prepared using reagent grade oxides and processed using conventional mixed oxide techniques described elsewhere.[3] Batches with the following compositions were processed: $(Ba_{1-x}Sr_x)TiO_3$ with x=0.175, 0.20, 0.25, 0.30; $Ba(Ti_{1-x}Sn_x)O_3$ with x=0.10, 0.13; (1-x)PMN-(x)PT with x=0.07, 0.10, 0.125, 0.15; PLZT x/65/35 with x=8, 9, 9.5, 10 and 11%. For PMN-PT powders, the columbite precursor method was utilized to maximize perovskite formation.[13] PMN-PT and PLZT compositions were calcined for 4 hours at 700°C and 875°C, respectively. BST and BTSn compositions were calcined at 1225-1275°C for 4 hours. X-ray diffraction analysis was used to ensure proper phase formation. For PMN-PT specimens, pyrochlore content measured using XRD was less than 3%. Disks with 1.27 and 2.54 cm diameters were pressed at 150 MPa.

PMN-PT and PLZT disks were sintered for 2 hours at 1150-1200 °C and 1275 °C, respectively. BST and BTSn discs were sintered on ZrO_2 setters at 1350-1375 °C for 2-4 hours. Weight loss and geometric densities were calculated. Specimens were precision lapped to 0.5 mm thickness to produce a dilatational thickness mode resonance ~4.5-5 MHz. Au was sputtered, thickness ~1500Å ,on the major faces for electrodes.

Dielectric property measurements included characterization of the field and temperature dependence of the relative dielectric permittivity and dielectric loss, performed over the frequency range from 0.1 kHz to 100 kHz using capacitance bridges (HP 4274 and 4275) and from 1 to >5 MHz using complex impedance data obtained from an impedance analyzer (HP3577A). In addition, the polarization versus electric field and pyroelectric behavior were examined and compared between families, using a Sawyer-Tower circuit, and the static Byer-Roundy technique, respectively.

High frequency field-induced electromechanical coupling factor were obtained from measurements of the series (f_s) and parallel (f_p) resonances, performed using a HP3577A network analyzer with HP35677A S-parameter test set configured for a one-port input reflection technique. Typical applied d.c. bias levels used for the measurements were between 1 and 15 kV/cm. The radial coupling factor k_p was calculated using a polynomial curve fitting equation.[14]. The dilatational thickness mode coupling factor k_t was calculated using the following equation: [14]

$$k_t^2 = \frac{\pi}{2} \frac{f_s}{f_p} TAN \frac{\pi}{2} \frac{(f_s - f_p)}{f_p} \quad \text{(Eqn. 2)}$$

The effect of applied electric field on the elastic properties of representative specimens from the various material families were examined at several temperatures. Using information obtained from the resonance measurements combined with physical measurements, the frequency constant, elastic compliance s_{11}^E and stiffness c_{33}^D coefficients, and mechanical quality factor Q_m were calculated.

Several temperature regions were selected for measurement, depending on the material family. For the normal and "pinched" ferroelectric compositions, temperatures were selected in the span $T_c \pm 30°C$. For relaxor ferroelectrics, resonance measurements were made over a range from the micro-polar region (T>T_{max}) to well below the depolarization temperature T_d.

RESULTS AND DISCUSSION

Dielectric Properties

A summary of the dielectric properties for the various families investigated is presented in Table II. Larger polarizations were measured for the Pb-based relaxor families. Values of P_{ind} decreased rapidly for temperature > T_c in the $BaTiO_3$ based families.

The highest small signal permittivities were observed in PMN and BTSn compositions. The low frequency dielectric constant and polarization behavior is shown for a 0.90PMN-0.10PT composition in Figure 1a. The micro-macro transition region, ΔT, was 25-45 and 100-140 °C for the PMN-PT and PLZT relaxor families, respectively. Values for K_{max} (@ 1 kHz) were 27-36,000 for the PMN and 5,300-11,000 for the PLZT compositions investigated. The low frequency dielectric constant and polarization behavior for a $Ba_{0.70}Sr_{0.30}TiO_3$ composition is shown in Figure 1b. For the BST and BTSn compositions, maximum values of K were 18-20,000 and 26-32,000, respectively. At temperatures above T_{max}, all the families exhibited low losses at 1 kHz. However, at 1 MHz, the dielectric loss increased to ~0.01 for the PLZT relaxor compositions. Minimal frequency dispersion was observed in the $BaTiO_3$-based families as compared to the PMN and PLZT relaxors.

A large field dependence of the permittivity was exhibited by all but the PLZT families. Values of K_{max} at 1 MHz and 10 kV/cm applied field for the BST/BTSn and PMN-PT familes were ~4,000-5,500 and 8,500-10,500 respectively.

Electromechanical Properties

Large field-induced coupling factors were obtained for the material families investigated. A summary of the electromechanical properties is shown in Table III. Maximum k_t values for the PMN-PT and PLZT families were 0.48 and 0.50, respectively. The field dependence of the coupling factor and polarization for a 0.90PMN-0.10PT specimen at two temperatures, 50°C (T~T_{max}), and 75°C(T>T_{max}), is shown in Figure 2. There was no remanent k_t observed after field removal for temperatures >T_d. The E-field dependence of k_t correlates fairly well with P_{ind} behavior at the measurement temperatures.

Table II. Summary of dielectric properties for compositions evaluated

Material Type	P_{max} ($\mu C/cm^2$)	K_{max}	K_{max} @1 MHz	K_{max} @ 1 MHz E=10kV/cm	D. F. max.	ΔT (°C)	Transition Behavior	K Field Depend.
Relaxor I (1-x)PMN-(x)PT	28-35	Large (28-36,000)	24,000	8,800	0.08	20-30	Broad (dispersive)	Moderate
Relaxor II PLZT	30-40	Moderate (6-10,000)	9,000	8,500	0.10	100-140	Very broad (dispersive)	Minimal
Normal $(Ba_{1-x}Sr_x)TiO_3$	16-19	Moderate (15-20,000)	16,400	5,400	0.05	0	Very narrow	Strong
"Pinched" $Ba(Ti_{1-x}Sn_x)O_3$	18-21	Large (28-35,000)	29,000	(7,000)	0.1	0	Very narrow	Strong

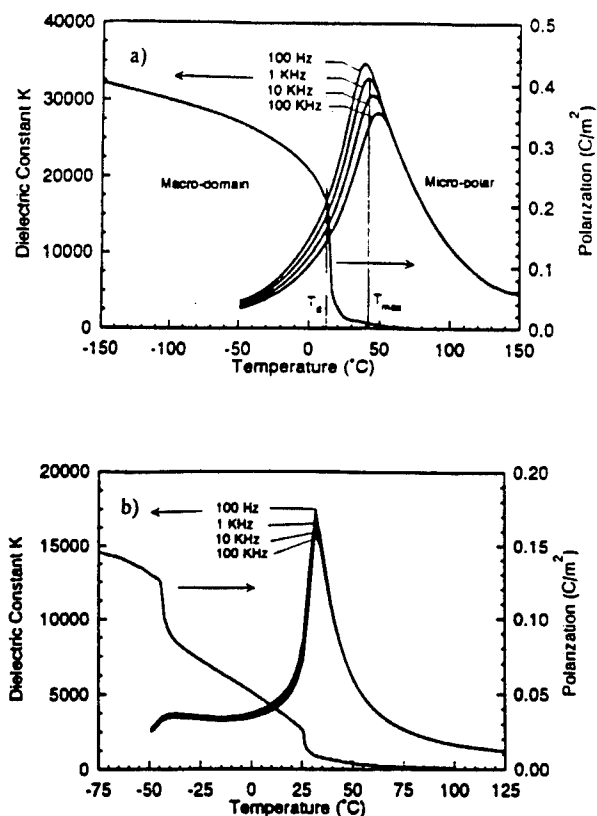Figure 1. Polarization and dielectric constant as function of
temperature for a) 0.90PMN-0.10PT relaxor and b)
$Ba_{0.70}Sr_{0.30}TiO_3$ normal ferroelectrics.

Large values of k_t (~0.50) were obtained for several of the
BST compositions. However, as shown in Figure 3, values for the k_t
decrease rapidly for temperatures greater than a few degrees above T_c.
At temperatures below T_c, significant remanent k_t values were
measured due to macro-domain switching. The relaxor compositions,
with a broad micro-macro transition region, exhibited significantly
wider temperature region for obtaining large induced k_t's without
hysteresis.
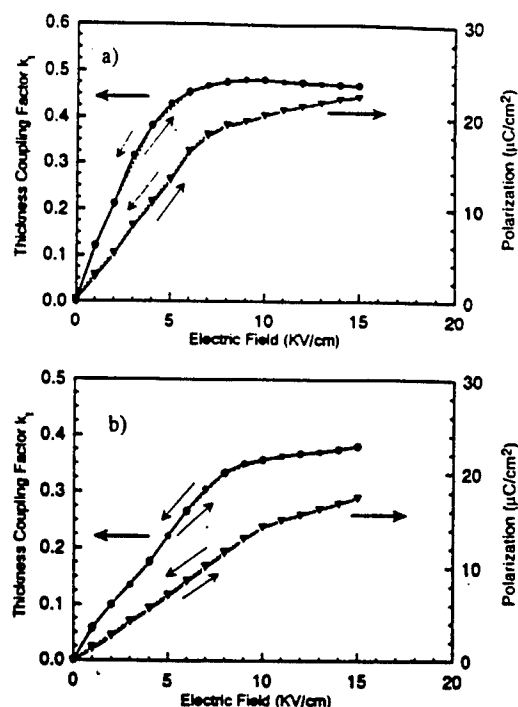
Figure 2. Field-induced thickness coupling factor k_t for a composition
at a) 50°C ($T \sim T_{max}$) and b) 75°C ($T > T_{max}$).

Table III. Summary of field-induced electromechanical properties for material families investigated

Material Type	Example	k_t max.	k_p max.	E_{sat} (kV/cm)	Temp. Range	Q_m	N_t (Hz-m)	C_{33}^D (x10^{10} N/m^2)
Relaxor I	(1-x)PMN-(x)PT	0.48	0.40	3-5	Broad	80	2,000	17-18
Relaxor II	PLZT	0.50	0.35	>5	Broad	50	2,100	16-19
Normal	$(Ba_{1-x}Sr_x)TiO_3$	0.50	0.30	4-6	Narrow	250	2,300	20-21
"Pinched"	$Ba(Ti_{1-x}Sn_x)O_3$	0.43	0.27	4-6	Narrow	280	2,500	21-23
Piezoceramic	PZT-5H	0.5	0.67	—	Narrow	65	1,950	15

The elastic coefficients exhibited a softenening around T_{max} and subsequent stiffening with increasing temperatures. A stiffening of the elastic coefficients was observed with increasing field at all measurement temperatures, with a reduced field dependence corresponding to the switching and saturation of the polarization at temperatures $\leq T_{max}$. Values for c_{33}^D and s_{11}^E were comparable to those of the respective piezoceramics in the $BaTiO_3$, PMN-PT and PLZT families.

Several observed characteristics are of interest in transducer applications. Due to the external electric field, the k_t/k_p anisotropy is significantly larger than observed in conventional $BaTiO_3$- and PZT-based piezoceramics. The mechanical quality factor, Q_m, also was field-dependent. In PMN-PT compositions, Q_m was adjustable in the range 80-220. This would be of interest as a dynamic/internal mechanism for adjusting damping/bandwidth in transducers.

CONCLUSIONS

A large field-induced piezoelectric effect was measured in several of the families evaluated, with values of k_t ~0.50. The temperature range for obtaining large electromechanical properties without hysteresis can be related to the underlying polarization mechanism. The relaxors exhibit a much broader temperature region than the $BaTiO_3$-based normal ferroelectrics, where significant P_{ind} can be achieved only a few degrees above T_c. PMN-PT relaxors offer large K's, low losses, and adjustable induced piezoelectric and elastic properties. However, the strong frequency dependence of the dielectric properties of relaxors may reduce the other advantages in some fixed frequency, tunable transducer applications.

Figure 3. Field-induced thickness coupling factor k_t for a $Ba_{0.70}Sr_{0.30}TiO_3$ composition at a) 40°C $(T>T_c)$ and b) 60°C $(T>T_c)$.

REFERENCES

[1] K. Uchino, "Electrostrictive Actuators: Materials and Applications," *Am. Ceram. Bull.*, 65 [4], pp. 647-652 (1986).

[2] H. Takeuchi, H. Masuzawa, and C. Nakaya, "Relaxor Ferroelectric Transducers," *Proceedings of 1990 Ultrasonics Symposium*, 697 (1990).

[3] J. T. Fielding, Jr., "Field-Induced Piezoelectric Materials for High Frequency Transducer Applications," Ph.D. Thesis, The Pennsylvania State University, (1993).

[4] W. Y. Pan, "Ferroelectric Type Materials for Actuator Applications," Ph.D. Thesis, The Pennsylvania State University (1988).

[5] L. E. Cross, "Piezoelectric and Electrostrictive Sensors and Actuators for Adaptive Structures and Smart Materials," *Proc. AME 110th Annual Mtg.*, San Francisco (1989).

[6] E. Fatuzzo, and W. J. Merz, *Ferroelectricity*, 104-147, John Wiley and Sons, New York (1967).

[7] K. Toyoda, T. Kato and Y. Sakabe, "Re-examination of the Phase Transitions in $BaTiO_3$-based Solid Solutions," *Ferroelectrics*, 108, 227-232 (1990).

[8] J. von Cieminski, H. T. Langhammer and H. P. Abricht, "Peculiar Electromechanical Properties of Some Ba(Ti, Sn)O_3 Ceramics," *phys. stat. sol.*, (a) 120, 285-293 (1990).

[9] S. J. Jang, K. Uchino, S. Nomura and L. E. Cross, "Electrostrictive Behavior of Lead Magnesium Niobate Based Ceramic Dielectrics," *Ferroelectrics*, 27, 31-34 (1982).

[10] S. W. Choi, T. R. Shrout, S. J. Jang and A. S. Bhalla,"Dielectric and Pyroelectric Properties in the PMN:PT System," *Ferroelectrics*, 100, 29 (1989).

[11] J. Kuwata, K. Uchino, and S. Nomura, "Electrostrictive Coefficients of $Pb(Mg_{1/3}Nb_{2/3})O_3$ Ceramics," *Jap. Jnl. of App. Phys.*, 19 [11], 2099-2103 (1980).

[12] G. H. Haertling and C. E. Land, "Hot-Pressed (Pb,La)(Zr,Ti)O_3 Ferroelectric Ceramics for Electrooptic Applications," *J. Am. Ceram. Soc.*, 54 [1], pp. 1-11 (1971).

[13] S. L. Swartz and T. R. Shrout, "Fabrication of Perovskite Lead Magnesium Niobate," *Mat. Res. Bull.*, 17, 1245-1250 (1982).

[14] IEEE Standard on Piezoelectricity, ANSI/IEEE Std 176-1978, The Institute of Electrical and Electronic Engineers, Inc., New York (1978).
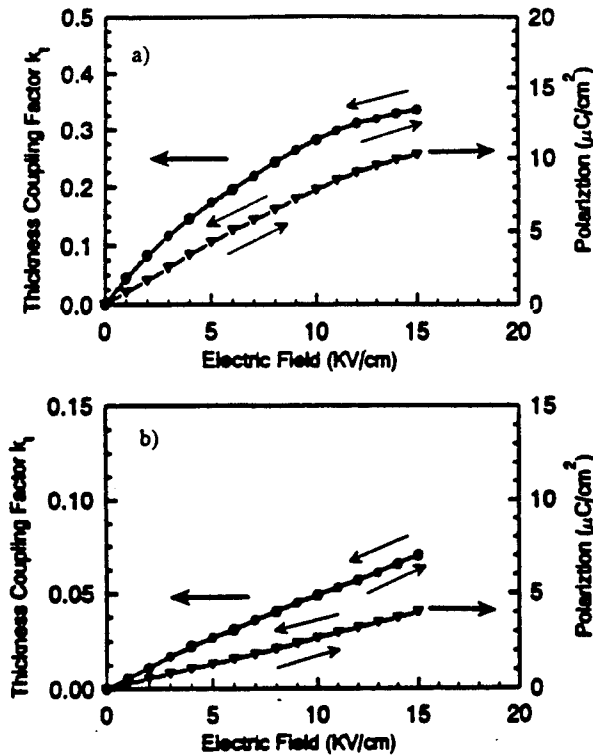
APPENDIX 62

Ultra-High Strain Ceramics with Multiple Field-Induced Phase Transitions

Russell P. Brodeur,* Kamau wa Gachigi,* Philip M. Pruna,* and Thomas R. Shrout*

Materials Research Laboratory, The Pennsylvania State University, University Park, Pennsylvania 16802

The induced polarization and longitudinal strain behavior of lanthanum- and titanium-modified antiferroelectric lead zirconate ceramics were measured as functions of electric field as high as 30 kV/mm (300 kV/cm). Two field-induced phase transitions were observed, both in polarization and strain. Polarization and strain levels greater than 0.5 C/m^2 and 0.75%, respectively, were achieved in this materials family.

I. Introduction

WITH continuing ferroelectric ceramic component miniaturization, the impact of "scale" in relation to the underlying physical phenomena becomes increasingly important. This becomes particularly evident for capacitors and/or actuators in which active layer thicknesses on the order of 5–10 μm can be achieved in multilayer structures via tape casting technology,[1-3] and less than 1 μm using various thin film techniques.[4,5] For such devices, in which the external boundary condition is applied voltage, dielectric materials can see electric fields in excess of 10 kV/mm. The impact of such high fields on ferroics was investigated by Fesenko:[6,7] it was reported that single crystals of the antiferroelectric PbZrO$_3$ undergo as many as three phase transitions (antiferroelectric → ferroelectric(I) → ferroelectric(II) → ferroelectric(III)) with increasing electric fields on the order of 20–40 kV/mm.

It was the aim of this work to examine the effects of ultrahigh fields on modified PbZrO$_3$ ceramics, with particular regard to the polarization and strain behavior associated with multiple ferroic phase transitions.

II. Experimental Procedure

In order to fabricate bulk ceramics capable of withstanding high electric fields, the base composition, Pb(Zr$_{0.95}$Ti$_{0.05}$)O$_3$, was modified with 2, 4, and 6 at.% La^{3+} to inhibit grain growth and enhance densification. These compositions are denoted PLZT 2/95/5, 4/95/5, and 6/95/5, respectively. Disk-shaped ceramic samples, approximately 5 mm in diameter by 0.5 mm thick, were sintered at 1200°–1350°C for 1 h in air. Densification, and thus dielectric breakdown strength, was enhanced (95%$_{theor}$ → >99%$_{theor}$) through hot isostatic pressing (1200°C for 1 h at 3 ksi (~20.7 MPa) in air) after sintering. The samples were lapped to thicknesses on the order of 100–150 μm, finishing with 1-μm diamond paste. The polished surfaces were electroded with sputtered gold, and air-dry silver was applied to the electrodes to ensure good electrical contact.

Low-field characterization included dielectric permittivity and loss as functions of frequency (0.1–100 kHz) and temperature (−50°–250°C). High-field measurements included polarization and strain hysteresis using a modified Sawyer Tower system and linear variable displacement transducer (LVDT) strain apparatus. Electric fields as high as 30 kV/mm were achieved using an amplified triangular waveform at 0.1 Hz.

III. Results and Discussion

As seen in Fig. 1, PLZT 2/95/5, 4/95/5, and 6/95/5 exhibit permittivity maxima at 213°, 216°, and 208°C, respectively, similar to the FE–AFE (ferroelectric–antiferroelectric) transition in pure PbZr$_{0.95}$Ti$_{0.05}$O$_3$ (235°C).[8] Additionally, the permittivity maximum decreases (from ≈4500 to ≈1000) and becomes more diffuse with increasing La-modification. The secondary permittivity peak also becomes more diffuse and its temperature maximum is a strong function of La content, ranging from 89°C for PLZT 2/95/5 to below room temperature for 6/95/5. The room-temperature permittivity increases with La-modification, due to broadening and flattening effects. For all compositions, room-temperature dielectric loss was <0.015 at 100 kHz, reflecting homogeneously densified ceramics.

As seen in Fig. 2(a), PLZT 2/95/5 exhibited the highest level of induced polarization at 20 kV/mm (>0.50 C/m^2) and greatest switching field hysteresis in the FE-II phase. On increasing field, this composition appears to switch directly from AFE to FE-II at ≈14 kV/mm, whereas on decreasing field it switches first from FE-II to FE-I at ≈8 kV/mm, followed by a more diffuse transition from FE-I to AFE, centered at ≈3.5 kV/mm. This observed polarization hysteresis behavior is very similar in appearance to the 25°C hysteresis data reported by Fesenko[7] for single-crystal PbZrO$_3$, namely

$$\text{AFE} \xrightarrow[21\ kV/mm]{} \text{FE-I} \xrightarrow[35\ kV/mm]{} \text{FE-II} \xrightarrow[40\ kV/mm]{} \text{FE-III}$$
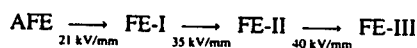
but naturally smoothed due to polycrystallinity. The switching fields are also decreased relative to PbZrO$_3$, due to the 5 at.% Ti-modification. Strain levels approaching 0.8% were achieved at 20 kV/mm, as presented in Fig. 2(b). Additional characterization in terms of temperature behavior and structural determination by XRD is still needed to confirm the associated structural phase changes.
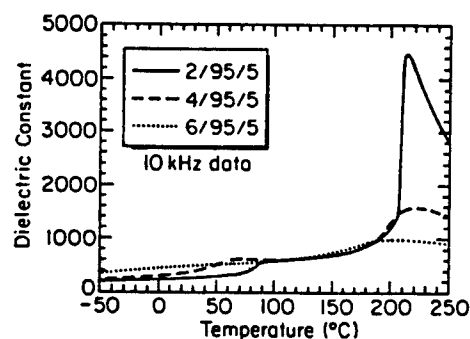
Fig. 1. Dielectric temperature behavior for PLZT x/95/5 (x = 2,4,6) at 10 kHz.
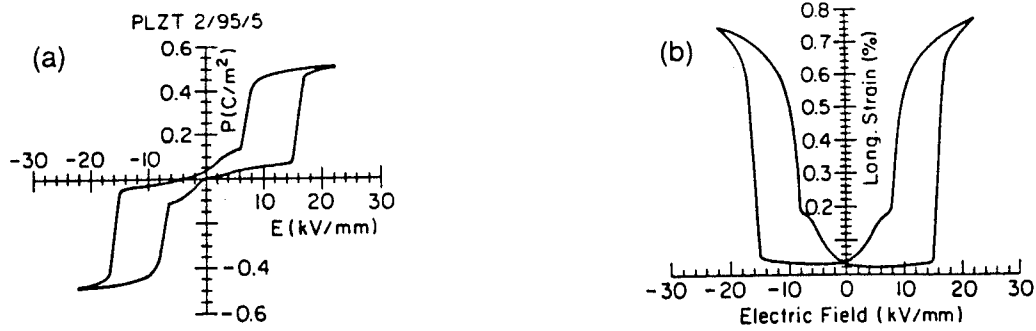
Fig. 2. Room-temperature electric field-induced (a) polarization and (b) longitudinal strain in PLZT 2/95/5.

On increasing the La^{3+} content to 4% (PLZT 4/95/5), high levels of P_{ind} (>0.50 C/m²) were also obtained, although the required fields were increased to ≈30 kV/mm, as seen in Fig. 3(a). Unlike PLZT 2/95/5, two distinct transitions are clearly visible on increasing field. The first (AFE to FE-I) occurs at ≈15 kV/mm, and the second (FE-I to FE-II) is induced at ≈18 kV/mm. With decreasing field, the FE-II to FE-I transition occurs at ≈15 kV/mm, while the FE-I to AFE transition is further broadened (compared with PLZT 2/95/5), but remains centered around ≈3 kV/mm. The maximum strain achieved for this material was 0.77% at 30 kV/mm, as presented in Fig. 3(b). This strain level is comparable to 2/95/5; however, the field required is much greater (30 kV/mm vs 20 kV/mm). Additionally, the level of hysteresis in the FE-II phase is substantially reduced. Using switching field hysteresis $(E_{s(inc)} - E_{s(dec)})$ for comparison, the levels are 3 and 6 kV/mm for PLZT 4/95/5 and 2/95/5, respectively.

Analogous to the dielectric behavior, Fig. 4(a) illustrates the effects of further La^{3+} increase (PLZT 6/95/5), resulting in a markedly diffuse, single phase transition at ≈20 kV/mm, with correspondingly reduced P_{ind} levels (0.4 C/m² at 25 kV/mm). Since the phase transition occurs at approximately the same field as the FE-I to FE-II in the other two compositions, it is probably a transition from AFE to FE-II. In accord with PLZT 4/95/5, the switching field hysteresis is further reduced to ≈1 kV/mm for this composition. As seen in Fig. 4(b), the strain levels are also correspondingly lower, showing no sign of saturation, even at 24 kV/mm.

Of particular significance in this work were the maximum levels of induced polarization (>0.5 C/m²) and strain (≈0.8%) achieved. The additive effect of multiple phase transformations was evident in these data, both in polarization and longitudinal strain. Maximum applied field levels were limited by electrical breakdown. To date, it has not been possible to apply greater
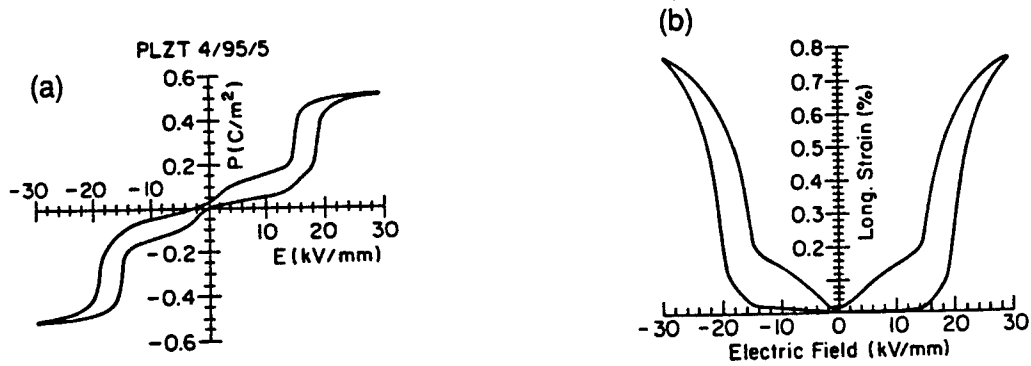

Fig. 3. Room-temperature electric field-induced (a) polarization and (b) longitudinal strain in PLZT 4/95/5.
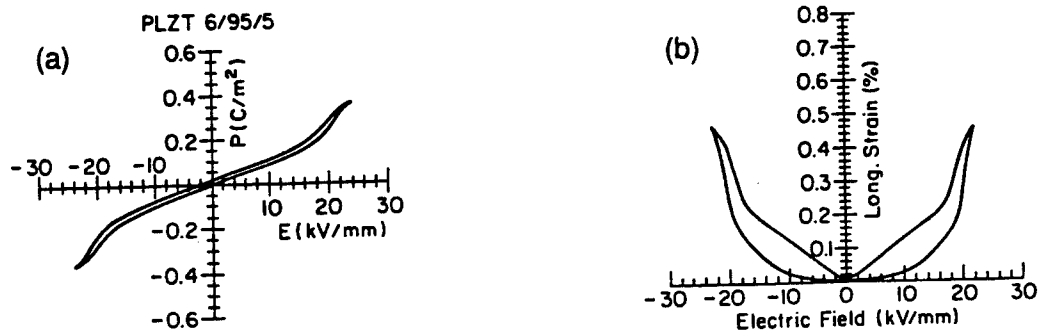

Fig. 4. Room-temperature electric field-induced (a) polarization and (b) longitudinal strain in PLZT 6/95/5.

than ≈20 kV/mm to PLZT 2/95/5 or ≈25 kV/mm to 6/95/5. Improvements in ceramic processing may lead to increased field stability and, ultimately, larger induced polarization and strain levels.

References

[1]M. Yonezawa, K. Utsumi, A. Ochi, and T. Mori, "Research and Development of Relaxor Ceramics at NEC"; pp. 159–64 in Proceedings of 7th IEEE International Symposium on Applications of Ferroelectrics. IEEE, New York, 1990.

[2]D. Hennings, M. Klee, and R. Waser, "Advanced Dielectrics: Bulk Ceramics and Thin Films," *Adv. Mater. (Weinheim, Fed. Repub. Ger.)*, **3**, 334–40 (1990).

[3]G. H. Maher, "MLC Capacitors with 6 Microns Active Dielectric and X7R Electrical Characteristics"; presented at the 91st Annual Meeting of the American Ceramic Society, Indianapolis, IN, April 24, 1989 (Paper No. 14-SVII-89).

[4]D. E. Dausch and G. H. Haertling, "Bulk vs. Thin Film PLZT Ferroelectrics"; pp. 297–300 in Proceedings of 8th IEEE International Symposium on the Application of Ferroelectrics. IEEE, New York, 1992.

[5]J. Chen, K. R. Udayakumar, and L. E. Cross, "Microwave Assisted Low Temperature Solid Phase Crystallization of Ferroelectric Thin Films"; see Ref. 4, pp. 313–16.

[6]O. E. Fesenko and V. G. Smotrakov, "Optic and Dielectric Study of Lead Zirconate Crystals," *Ferroelectrics*, **12**, 211–13 (1976).

[7]O. E. Fesenko, R. V. Kolesova, and Yu. G. Sindeyev, "The Structural Phase Transitions in Lead Zirconate in Super-High Electric Fields," *Ferroelectrics*, **20**, 177 (1978).

[8]B. Jaffe, W. R. Cook, Jr., and H. Jaffe, *Piezoelectric Ceramics*, p. 136. Academic Press, New York, 1971.

APPENDIX 63

FIELD-INDUCED LEAD ZIRCONATE TITANATE STANNATE ANTIFERROELECTRIC-TO-FERROELECTRIC PHASE SWITCHING CERAMICS

Shoko Yoshikawa, Namchul Kim, Thomas Shrout,
Qiming Zhang, Paul Moses, and L. Eric Cross
Materials Research Laboratory
The Pennsylvania State University
University Park, PA 16802

ABSTRACT

The electric field induced antiferroelectric-to-ferroelectric phase transition of lead zirconate titanate stannate ceramics was investigated by means of dielectric, polarization, and strain hysteresis measurements. Compositions of varying titanium and tin within the general formula $(Pb_{0.98}La_{0.02})(Zr_{0.66}Ti_{0.11-x}Sn_{0.23+x})O_3$, located in the tetragonal antiferroelectric phase field and near the ferroelectric rhombohedral boundary were prepared. As the applied electric field increased, a sudden increase in both longitudinal and transverse strain was observed with a corresponding change in dielectric constant, loss, and polarization, indicating the transition from antiferroelectric to ferroelectric phase. The longitudinal strain increased continuously into the ferroelectric phase, whereas the transverse strain became negative after the phase change. By defining the phase change field from polarization and high field dielectric constant and loss measurements, the longitudinal strains associated with the phase change for all of the compositions were less than 0.2%. For some compositions, however, the longitudinal strain increased to levels greater than 0.5% with increasing applied field. Owing to the relatively small decrease in transverse strain in the ferroelectric region, the volume strain continued to increase even after antiferroelectric to ferroelectric phase change.

1. INTRODUCTION

Modified lead zirconate titanate stannate based ceramics have been studied extensively over the past several decades for potential applications such as charge storage capacitors[1,2] and high-strain transducers/actuators[3-6]. Previously, studies[2-6] have reported longitudinal strains on the order of 0.2 to 0.8%, believed to be associated with the strains associated with the antiferroelectric (AFE)-to-ferroelectric (FE) phase transformation. However, inconsistencies in the reported strain values among the researchers may be related to experimental issues, such as at what E-field the phase switching was completed. In this study, therefore, five tetragonal $(Pb_{0.97}La_{0.02})(Zr_{0.66}Ti_{0.11-x}Sn_{0.23+x})O_3$ antiferroelectric ceramics were prepared and field-induced polarization and strains (longitudinal and transverse) were measured through the AFE-to-FE switching and up to three times the switching field, in hopes of better understanding this phenomena.

Detail sample preparation and characterization methods including dielectric and electric field induced strain are described in this paper along with the discussion of the results.
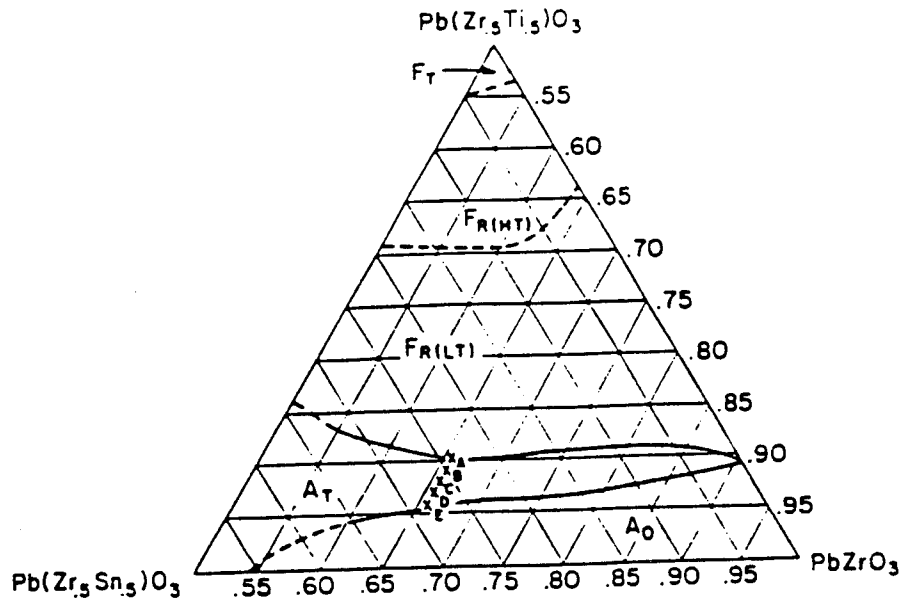
Figure 1. Ternary phase diagram of Pb(Zr,Ti,Sn)O$_3$ system taken from reference 7. x indicates locations of selected compositions A, B, C, D, and E in the tetragonal antiferroelectric phase field.

2. EXPERIMENTAL PROCEDURE

2.1. Sample Preparation

The compositions described as A to E in Table 1 were prepared according to the formula (Pb$_{0.97}$La$_{0.02}$)(Zr$_{0.66}$Ti$_{0.11-x}$Sn$_{0.23+x}$)O$_3$ (hereafter designated PLZTS) x=0, 0.01, 0.02, 0.03, 0.04. Figure 1 shows the location of these compositions in the ternary phase diagram. Polycrystalline ceramic materials investigated in this study were prepared by solid state reaction, using the appropriate amount of reagent grade raw materials of lead carbonate (PbCO$_3$), lanthanum oxide (La$_2$O$_3$), zirconium dioxide (ZrO$_2$), titanium dioxide (TiO$_2$),and tin oxide (SnO$_2$). The chemical purity of each of the raw materials was greater than 99%. The processing flow chart used to prepare the various ceramic samples is described in Figure 2. The sintering process was performed in a PbO rich atmosphere to minimize weight loss.

To further enhace densification and subsequent dielectric breakdown, the pre-sintered specimens (~93% theoretical dense) were hot isostatically pressed for 2 hours at 1100°C in an air atmosphere under a pressure of 20 MPa.[8]

The disk samples were then prepared by polishing with silicon carbide and alumina polishing powders to achieve flat and parallel surfaces onto which gold sputtered electrodes were applied. An air-dried silver paste was overlaid as a top surface over the gold electrodes to improve electrical contact and reduce electrode abrasion problems during characterization and electromechanical testing.

Table 1. Composition of (PbLa)(ZrTiSn)O$_3$ (PLZTS) antiferroelectric ceramics investigated in this work.

Group A

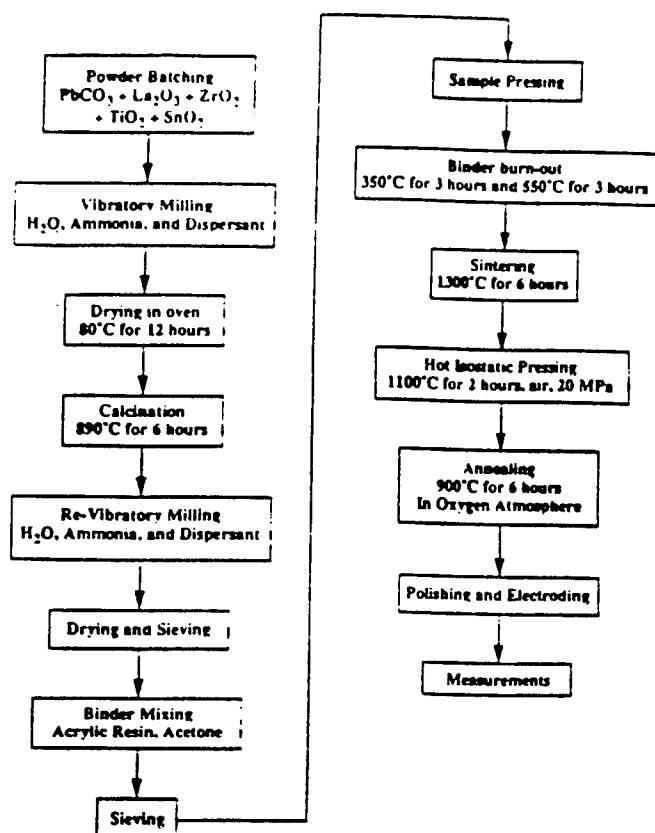| Notation	Composition
A	(Pb$_{0.97}$La$_{0.02}$)(Zr$_{0.66}$Ti$_{0.11}$Sn$_{0.23}$)O$_3$ Ti/Sn: 0.11/0.23
B	(Pb$_{0.97}$La$_{0.02}$)(Zr$_{0.66}$Ti$_{0.10}$Sn$_{0.24}$)O$_3$ Ti/Sn: 0.10/0.24
C	(Pb$_{0.97}$La$_{0.02}$)(Zr$_{0.66}$Ti$_{0.09}$Sn$_{0.25}$)O$_3$ Ti/Sn: 0.09/0.25
D	(Pb$_{0.97}$La$_{0.02}$)(Zr$_{0.66}$Ti$_{0.08}$Sn$_{0.26}$)O$_3$ Ti/Sn: 0.08/0.26
E	(Pb$_{0.97}$La$_{0.02}$)(Zr$_{0.66}$Ti$_{0.07}$Sn$_{0.27}$)O$_3$ Ti/Sn: 0.07/0.27

Figure 2. The processing flow chart for PLZTS ceramics.

2.2. Characterization

2.2.1. Phase, Density, and Microstructure

The powders were examined by x-ray diffraction (XRD) at each processing step to insure phase purity. Weight change, geometrical density, and grain size were determined for all the compositions and each firing stage. The average grain size was determined using the line intercept metal on fracture surfaces monitored by Scanning Electron Microscope (SEM).

2.2.2. Dielectric Properties

Dielectric measurements were performed on representative samples using an LCR meter Hewlett-Packard No. 4274A. The capacitance and dielectric loss were measured at 1 kHz. The dielectric constant (K) was calculated from capacitance and sample geometries.

The field-induced dielectric constant (K) was determined from the following two methods:

(i)   low field capacitance under DC bias field (0 to 150 kV/cm)[9,10], and

(ii)   calculated from the slope of the polarization-electric field (P-E) hysteresis loop[10,11].

The dielectric properties described above (i) were measured with an HP 4274A Multi-frequency LCR meter at a frequency of 1 kHz and an AC signal of 1 V. The DC bias was supplied by a Keithley 246 High Voltage Supply having a maximum voltage of 3100 V and a current limit of 10 mA. Electric breakdown of the samples at a high voltage could damage or destroy the LCR meter, thus a DC blocking circuit was used to protect the instrument. The blocking circuit introduced errors of ± 1% capacitance and ± 0.005 dielectric loss in measurements at 1 kHz. The samples were immersed in Fluorinert insulating liquid (FC-40, 3M) to prevent arcing under high voltage application.

In the second method (ii), the dielectric constant was calculated from electric field-polarization hysteresis curves and resulting polarization-electric field polynomial function. The induced dielectric constant K_{ind} could be derived from differentiating the polynomial function and through the following equation:

$$K_{ind} = 1 + \frac{1}{\varepsilon_o} \frac{\partial P}{\partial E}$$

where P is the polarization (C/m^2), K_{ind}, the induced dielectric constant, and E, the electric field (V/m).

2.2.3. Polarization and Strain

Relevant parameters in polarization and strain hysteresis loops are defined and are designated in Figure 3. The polarization electric field (P-E) measurements were performed on representative samples using a computer controlled modified Sawyer-Tower circuit. The field-induced strains (longitudinal and transverse) associated with antiferroelectric-to-ferroelectric phase switching were simultaneously determined using an LVDT (Linear Variable Differential Transformer) sensor driven by a lock-in amplifier (Stanford Research Systems, Model SR830 DSP). Through an LVDT sensor, the longitudinal and transverse strains of the samples were measured in parallel and perpendicular directions with the applied electric field, respectively, as shown in Figure 4(B). The volume strain was then calculated from the longitudinal and transverse strains. An AC signal frequency of 0.1–1 Hz was employed and the data obtained after several cycles at an appropriate field. The frequency was increased up to 20 Hz to ensure thermal expansion effects due to self-heating of the sample did not affect the displacement data. A Fluorinert liquid was employed to prevent arcing under high field application. In general, the electric field was slowly increased up to 100 ~ 200 kV/cm until the sample(s) experienced breakdown. All of the polarization and strain measurements were performed at room temperature.

3. RESULTS AND DISCUSSION

3.1. Phase Purity, Density, Grain Size, and Microstructure

XRD analysis revealed that all of the samples except composition A were tetragonal with no second phases observed within the detection limit (< 2%). XRD data of Sample A showed mixture of tetragonal and rhombohedral phase. Ceramics sintered at 1300°C resulted in a density range of 7.70–7.86 g/cm^3 while minimal weight loss (< 1 wt%). Further improvement in densification (7.78–7.94 g/cm^3) was achieved through hot isostatic pressing (HIP) of pre-sintered samples. Similar microstructures with grain sizes on the order of 4 to 5 μm and transgranular and intergranular mixed fracture surfaces were found for all the compositions.
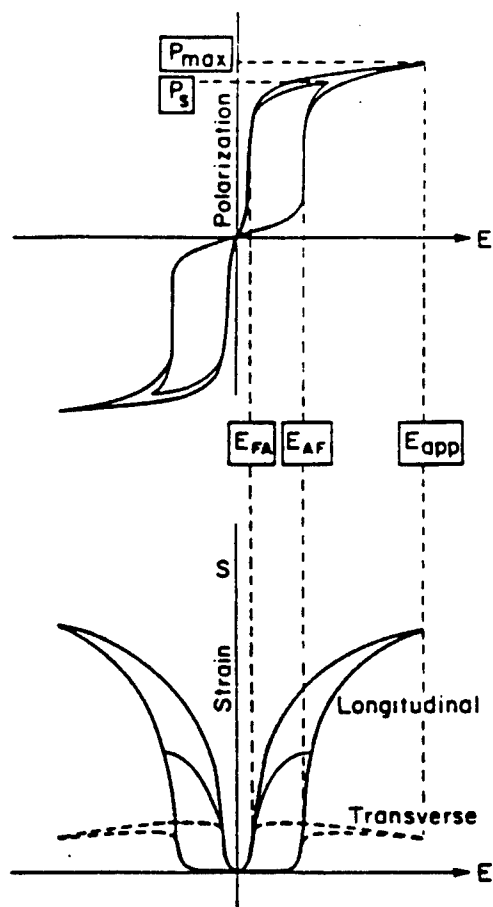
Figure 3. Typical polarization, strain loops, and some illustrated parameters, E_{FA}, E_{AF}, E_{app}, P_s, and P_{max}.
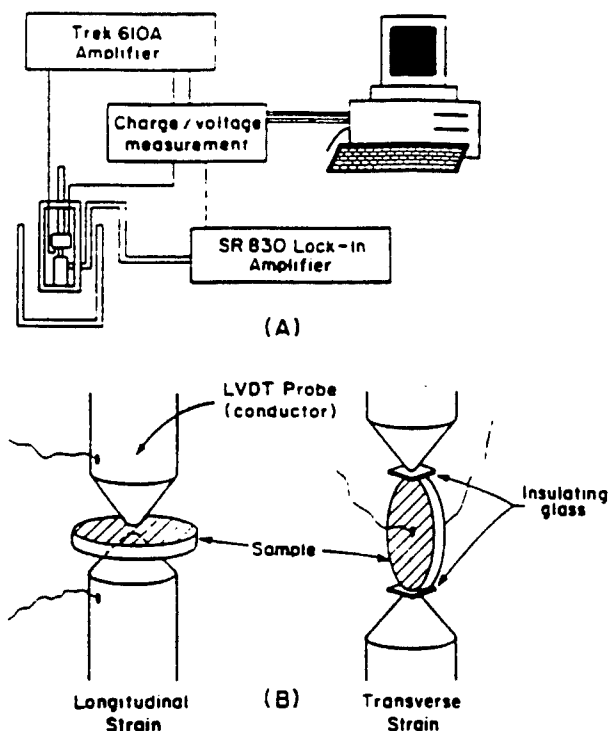

Figure 4. (A) Schematic drawing of polarization and strain measurement set-up, and (B) Schematic drawing of a sample configuration in LVDT probe for longitudinal and transverse strain measurement.

3.2. Dielectric Properties

The dielectric constant and loss at room temperature decreased ($K=860\rightarrow500$, $\tan\delta = 0.72\%\rightarrow0.18\%$) with increasing Sn^{4+} (or decreasing Ti^{4+}) as listed in Table 2 (compositions A-E). Figure 5 typifies the dielectric constant and loss behavior of an anti-ferroelectric under DC bias field for composition B. When the DC field was applied to the ceramic sample, the dielectric constant increased slightly, then dropped abruptly at a certain bias level, which is the switching field (E_{AF}) from the AFE to FE phase transition. A peak in dielectric loss was found to occur at the switching field, E_{AF}. Dielectric constant and loss peaks were also observed with decreasing bias at the FE-to-AFE switching field (E_{FA}). It should be noted that the dielectric constant of the samples, which have been switched to the ferroelectric phase, exhibited higher values than that for the virgin samples (sample which has not been exposed to a bias field). This behavior is due to the oriented-antiferroelectric state which exists after a cycled process (AFE-FE-AFE) compared with the initially random antiferroelectric state[3].

Table 2. Dielectric property, field-induced polarization and strain of antiferroelectric $(Pb,La)(Zr,Ti,Sn)O_3$(PLZTS) ceramics.

Comp.	Dielectric Parameters 1 kHz (Low Field)				Electric Field-induced Polarization and Strain					
					At switching field			At max. applied field		
	K_{RT}	tanδ (%)	T_c (°C)	K_{max}	E_{AF} (kV/cm)	P_s ($\mu C/cm^2$)	S_3 (%)	$E_{app.}$ (E_{app}/E_{AF}) (kV/cm)	$P_{max.}$ ($\mu C/cm^2$)	S_3 (%)
A†	860	0.72	177	2800	26	27	0.16	80 (3.1)	35	0.38
B	730	0.51	178	2500	37	32	0.18	111 (3.0)	38	0.42
C	620	0.30	178	2100	51	32	0.18	153 (93.0)	40	0.53
D	560	0.18	182	1700	71	32	0.16	133 (1.9)	41	0.48
E	500	0.18	189	1400	94	32	0.17	120 (1.3)	40	0.37

† Composition A is a mixed phase of antiferroelectric and ferroelectric. The switching field (26 kV/cm) is determined from the strain measurements.
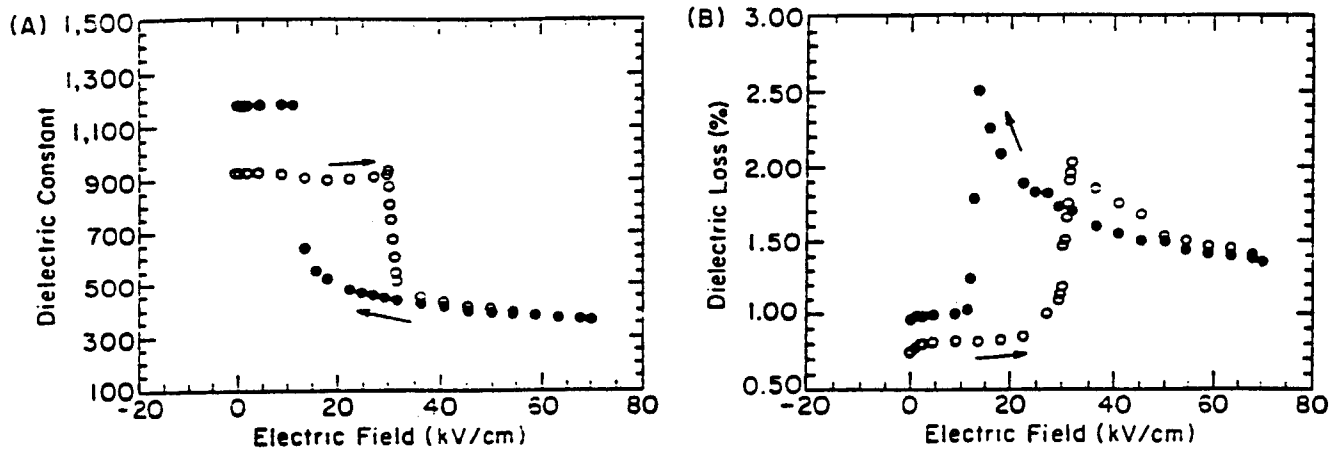

Figure 5. Electric field biased dielectric constant (A) and loss (B) for composition B. (white circle: increasing bias field, black circle: decreasing bias field).

Figure 6 shows the differential dielectric constant (described earlier in section 2.2.2, (ii)) behavior of antiferroelectric ceramic composition B calculated from P-E hysteresis loops. Peaks in dielectric constant of more than 10^5 are observed at the switching fields E_{AF} and E_{FA}. The discrepancy of the dielectric constants values between measurements methods (i) and (ii) is believed to be due to a sub-lattice-reorientation process for the antiferroelectric-to-ferroelectric phase. Actually, the AC dielectric constant under DC bias (case (i)) is the incremental dielectric constant, which measures the change of polarization due to a weak AC field superimposed on the DC field. Thus, this measurement is not concerned with the time-dependent domain (sub-lattice) reversal but only with slight changes in the polarization of the ceramics. The step increase of biasing field is hardly coincident with the switching field at which the re-orientation of sub-lattice in antiferroelectric-to-ferroelectric occurs. In the case of the differential dielectric constants, the P-E hysteresis continuously measures the phase change between AFE and FE. Thus, the differential of the P-E curve could include the sublattice reversal at a finite time, giving rise to peaks of dielectric constant at the switching fields (E_{AF} and E_{FA}).
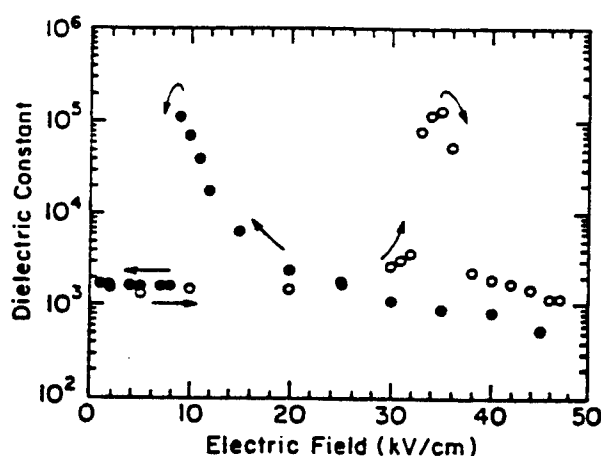

Figure 6.   Dielectric constant of composition B calculated from polarization-electric field hysteresis loop.

3.3.   Field-Enforced Polarization and Strain Behavior

Polarization and induced strains were determined with changing the applied field in a step-wise manner. It was quite apparent that the hot-isostatically-pressed (HIP) samples exhibited higher breakdown field than those only conventionally fired. A representative antiferroelectric hysteresis loop for the composition B is shown in Figure 7, with increasing bias field. It shows typical AFE-FE-AFE double-hysteresis loops associated with the application of positive and negative E-field, as pictorially given in Figure 3.

As presented in Table 2, the maximum polarization in the ferroelectric region was found to increase by only about 19% from the switching field (37 kV/cm) to 111 kV/cm. However, the accompanying longitudinal strain increased greatly from 0.18% at the switching field to 0.42% at 111 kV/cm. Figure 8 describes the transverse, longitudinal and calculated volumetric strain, as a function of applied field. As shown, the transverse strain starts to decrease above a certain field level, which indicates the completion of the AF-FE phase change. As expected, the increase in
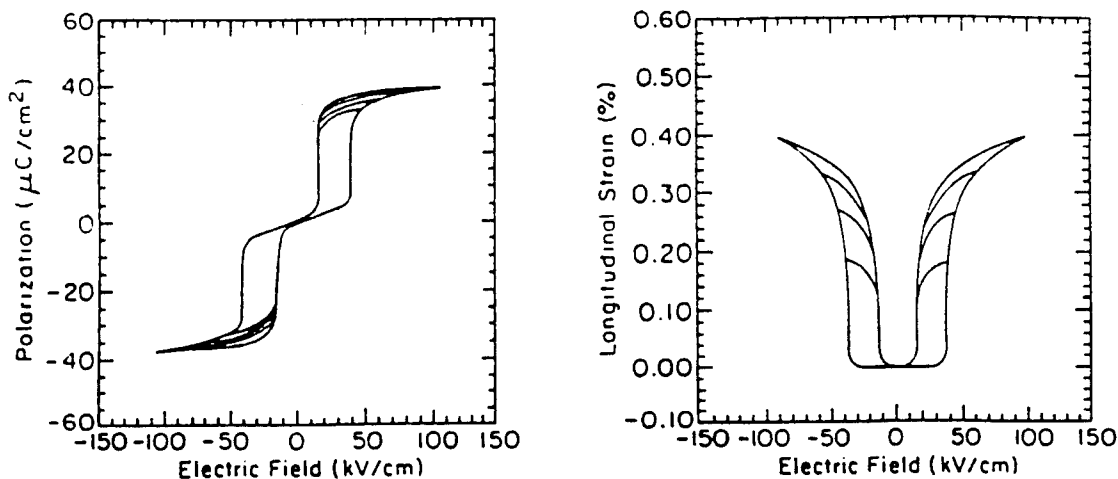
Figure 7.   Polarization (A) and longitudinal strain (B) of composition B under various electric fields.

volume associated with the phase switching from the tetragonal antiferroelectric to rhombohedral ferroelectric structure is clearly observed. However, the volumetric strain continued to increase with applied E-field, which was not anticipated.

The polarization electric field hysteresis loops and the accompanying longitudinal strains of all of the samples are shown in Figure 9. Except for composition A, all the compositions exhibited a classic antiferroelectric double-hysteresis loop. Composition A revealed a hysteresis loop shape between that of a ferroelectric and antiferroelectric owing to the proximity of the ferroelecric rhombohedral phase boundary. Both the forward and reverse switching fields (E_{AF} and E_{FA}) increased with decreasing Ti/Sn ratio as the compositions moved away from the phase boundary into the antiferroelectric phase A_T. Interestingly, the E-field hysteresis ($\Delta E = E_{AF} - E_{FA}$) was found to be constant in this group of PLZTS ceramics.
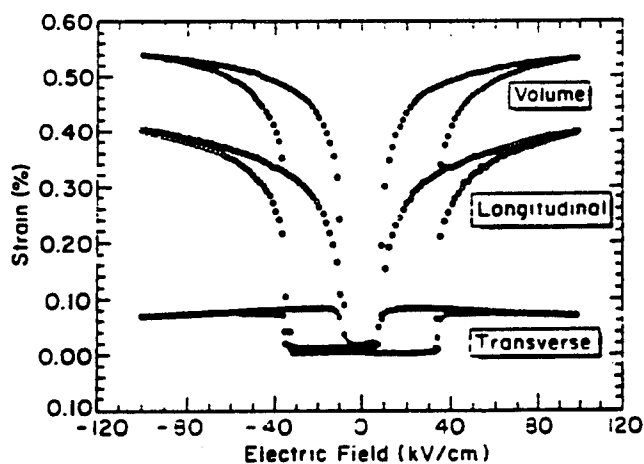

Figure 8.   Field-induced longitudinal, transverse, and volume strain at maximum electric field level for composition B.
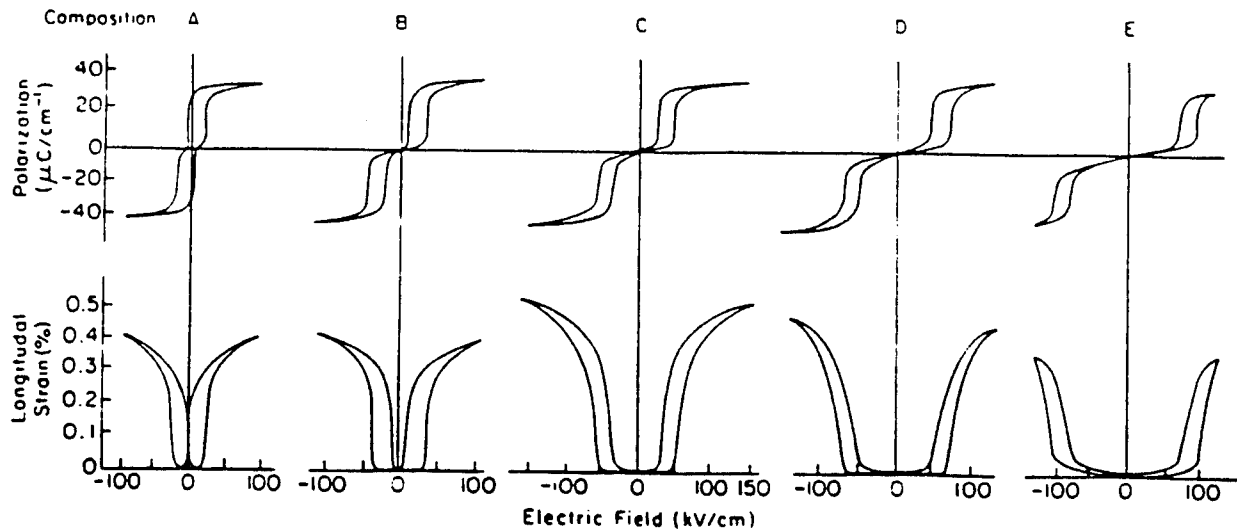
Figure 9. Field-induced polarization and longitudinal strain of composition A, B, C, D, and E at the maximum applied electric field.

The field-induced polarization and strain of the five compositions studied in this work are plotted as functions of electric field (kV/cm) in Figure 10. The changes in polarization under bias field show similar behavior among the examined compositions, as indicated in Figure 10(A), whereas the strains are compositionally-dependent at the same field level (Figure 10(B)). The magnitude of strain, however, approach a similar range of 0.4–0.5% for fields greater than 130 kV/cm. As shown in previous research[2,4,5], compositions closer to phase boundary show higher strains at lower electric field.
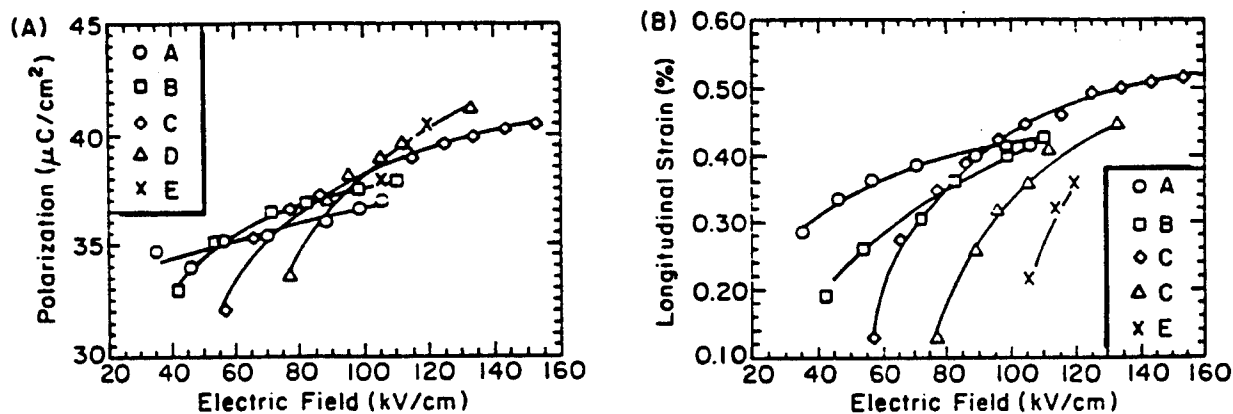

Figure 10. Polarization (A) and longitudinal strain (B) of composition A-E as a function of applied electric field.

4. CONCLUSION

Compositions with varying Ti/Sn ratio in PLZTS antiferroelectric ceramics were prepared by solid state reaction. Hot isostatic pressing was used to enhance the density of the ceramics resulting in higher field-related breakdown strength allowing for the high field measurements.

The dielectric behavior as a function of field induced state was determined using the following methods: (i) low field capacitance under DC bias and (ii) the slope of the polarization–E-field hysteresis. Both methods indicated similar phase switching field levels E_{AF} as indicated by drastic changes in K and loss, though the level of K peak dielectric constants were quite different depending on the method used.

The high field longitudinal strain behavior revealed somewhat unexpected results, increasing continuously with applied field without a clear indication of the completion of the AF to FE phase change. The longitudinal strains of the phase switching field E_{AF}, defined by the dielectric measurement methods, were all less than 0.2%, increasing to more than 0.5% without substantial increase in polarization. A large increase in volume strain was expected at E_{AF} owing to the larger unit cell of the FE rhombohedral phase relative to the AF tetragonal one. The volume strain, however, continued to increase substantially even in the FE phase.

5. ACKNOWLEDGMENTS

6. REFERENCES

1. B. Jaffe, "Antiferroelectric Ceramics with Field-Enforced Transitions: A New Nonlinear Circuit Element," The Proceedings of the IRE, Vol. 49[8], 1264–1267, 1961.
2. D. Berlincourt, H.H.A. Krueger, and B. Jaffe, "Stability of Phases in Modified Lead Zirconate with Variation in Pressure, Electric Field, Temperature and Composition," J. Phys. Chem. Solids, Vol. 25, 659–674, 1964.
3. K. Uchino and S. Nomura, "Electrostriction in PZT-Family Antiferroelectrics," Ferroelectrics, Vol. 50, 191–196, 1983.
4. A Furuta, K-Y. Oh, and K. Uchino, "Shape Memory Ceramics and Their Application to Latching Relays," Sensors and Materials, 3.4, 205–215, 1992.
5. W.Y. Pan, Q. Zhang, A. Bhalla, and L.E. Cross, "Field-Forced Antiferroelectric-to-Ferroelectric Switching in Modified Lead Zirconate Titanate Stannate Ceramics," J. Am. Ceram. Soc., Vol. 72[4], 571–578 1989.
6. W.Y. Pan, C.Q. Dam, Q.M. Zhang, and L.E. Cross, "Large Displacement Transducers Based on Electric Field Forced Phase Transitions in the Tetragonal $(Pb_{0.77}La_{0.02})(Ti,Zr,Sn)O_3$ Family of Ceramics," J. Appl. Phys., 66[12], 6014–6023 1989.
7. D. Berlincourt, "Transducers Using Forced Transitions Between Ferroelectric and Antiferroelectric States," IEEE Trans. on Sonics and Ultrasonics, SU-13, 4, 116-125 1966.
8. N.C. Kim, D.A. McHenry, S.J. Jang, and T.R. Shrout, "Fabrication of Optically Transparent Lanthanum Modified $Pb(Mg_{1/3}Nb_{2/3})O_3$ Using Hot Isostatic Pressing," J. Am. Ceram. Soc., 7[4], 923–928 (1990).
9. G. Love, "Energy Storage in Ceramic Dielectrics," J. Am. Ceram. Soc. 73, 323-28 1990.
10. I. Burn, "Field-Enforced Ferroelectricity in Glass-Bonded Lead Zirconate," Ceram. Bull., Vol. 50[5], 501–505 1971.
11. N. Bar-Chaim, M. Brunstein, J. Grünberg, and A. Seidman, "Electric Field Dependence of the Dielectric Constant of PZT Ferroelectric Ceramics," J Appl. Phys., 45[6], 2398–2405 (1974).

APPENDIX 64

United States Patent [19]

Gururaja et al.

[54] **ELECTROSTRICTIVE ULTRASONIC PROBE HAVING EXPANDED OPERATING TEMPERATURE RANGE**

[75] Inventors: **Turuvekere R. Gururaja**, North Andover, Mass.; **Joseph Fielding**, State College, Pa.; **Thomas R. Shrout**, State College, Pa.; **Sei-Joo Jang**, State Collete, Pa.

[73] Assignee: **Hewlett-Packard Company**, Palo Alto, Calif.

[21] Appl. No.: **113,450**

[22] Filed: **Aug. 27, 1993**

[51] Int. Cl.^{5} H01L 41/87; C04B 35/46

[52] U.S. Cl. 310/358; 310/346; 252/62.9

[58] Field of Search .... 310/346, 357, 358; 252/62–69, 62.9 R, 62.9 PZT

[56] **References Cited**

U.S. PATENT DOCUMENTS

4,712,156	12/1987	Bardhan	361/321
4,736,631	4/1988	Takeuchi et al.	73/649
4,940,681	7/1990	Ushida et al.	252/62.9
5,032,558	7/1991	Bailey et al.	501/137
5,135,897	8/1992	Uchino et al.	252/62.9
5,188,992	2/1993	Nishimura et al.	252/62.9
5,210,455	5/1993	Takeuchi et al.	310/328
5,219,810	6/1993	Furuya et al.	501/136

FOREIGN PATENT DOCUMENTS

2094579	2/1990	Japan .	
2059716B	9/1980	United Kingdom	H04R 17/00

OTHER PUBLICATIONS

"Electrostrictive Materials For Ultrasonic Probes," Masuzawa et al., Japanese Journal of Applied Physics, vol. 28, (1989) Supplement 28–2, pp. 101–104.

"Dielectric And Piezoelectric Properties Of Lanthanum-Modified Lead Magnesium Niobium–Lead Titanate Ceramics," Huebner et al., Ferroelectrics, 1989, vol. 93, pp. 341–349.

"Relaxor Ferroelectric Transducers," Takeuchi et al., Central Research Laboratory, Hitachi, Ltd., Kokubunju, Tokyo 185, Japan.

Primary Examiner—Steven L. Stephan

[57] **ABSTRACT**

An ultrasonic electrostrictive transducer for transmitting and receiving ultrasonic energy and having an expanded operating temperature range, preferably about room temperature. The transducers may be made from PMN-PT solid solutions having select mole percentages of PT and being doped with La, whereby the operating temperature range about a given operating temperature may be effectively doubled.
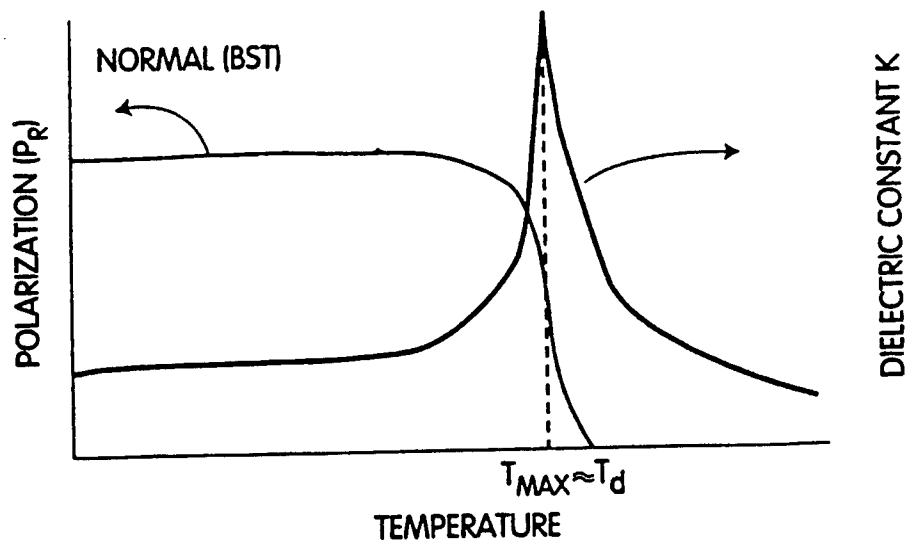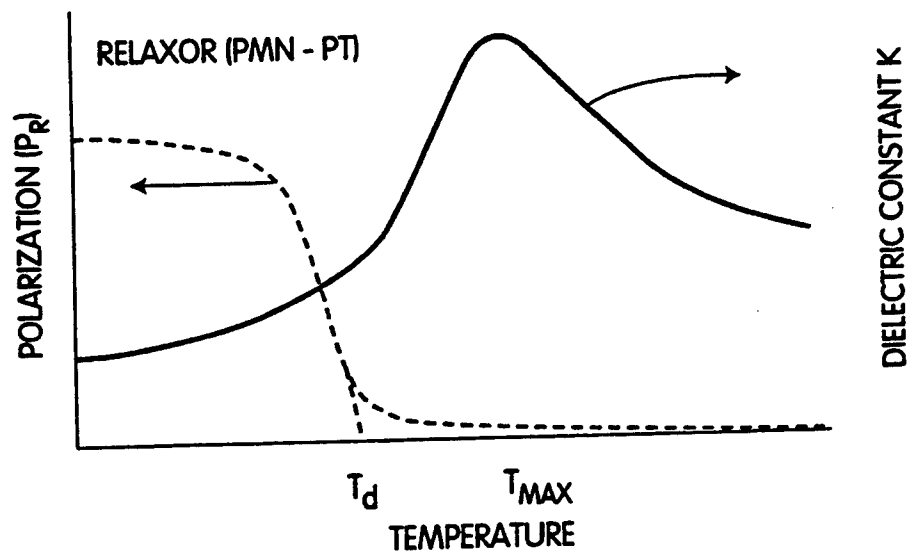
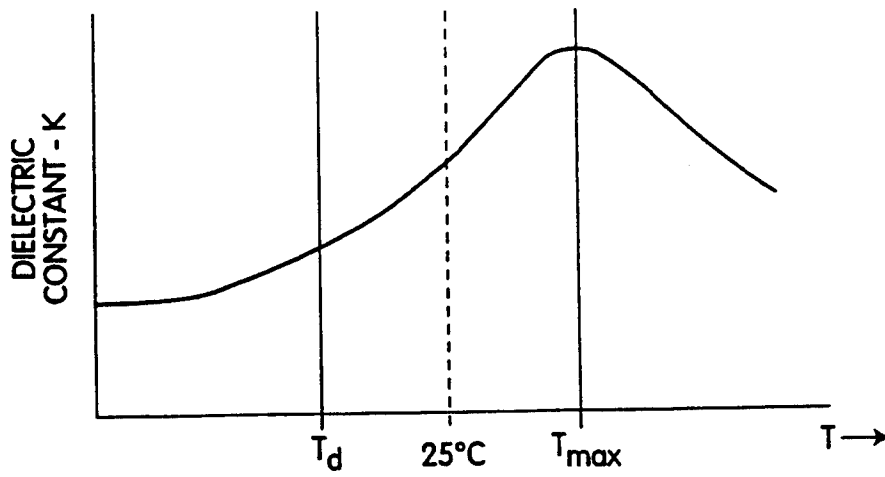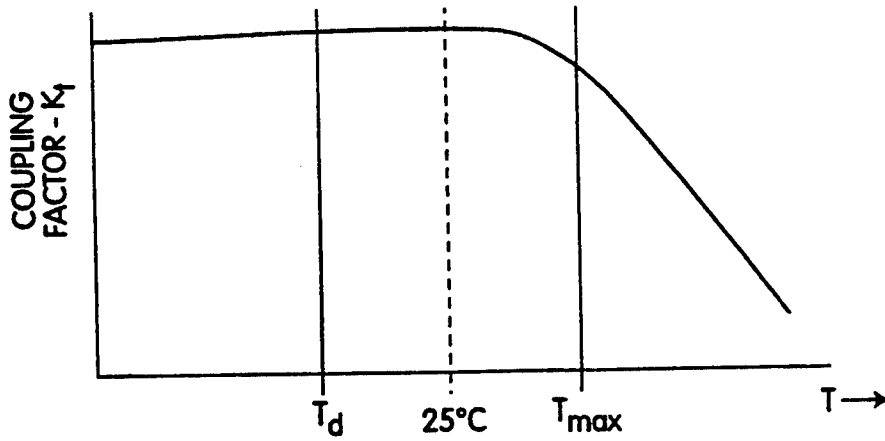**12 Claims, 9 Drawing Sheets**
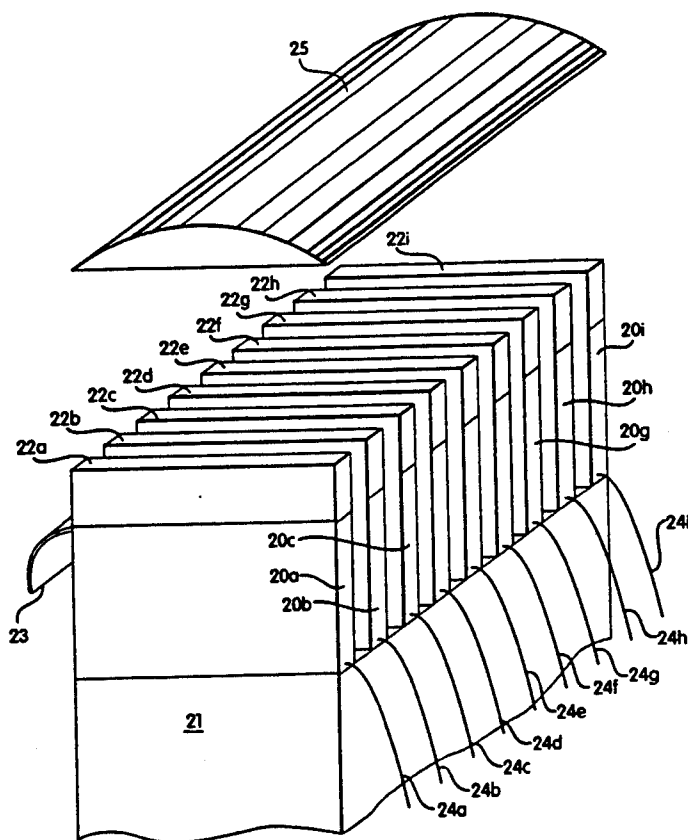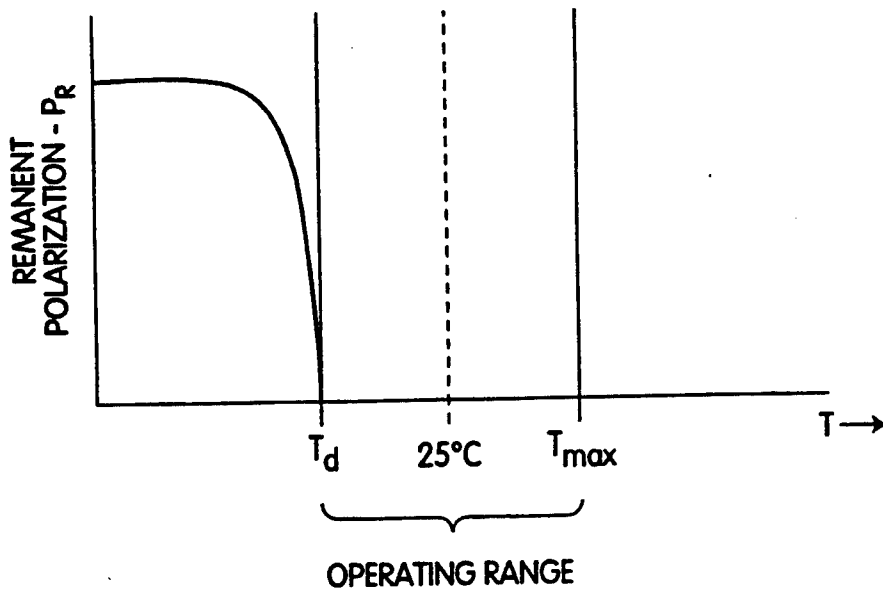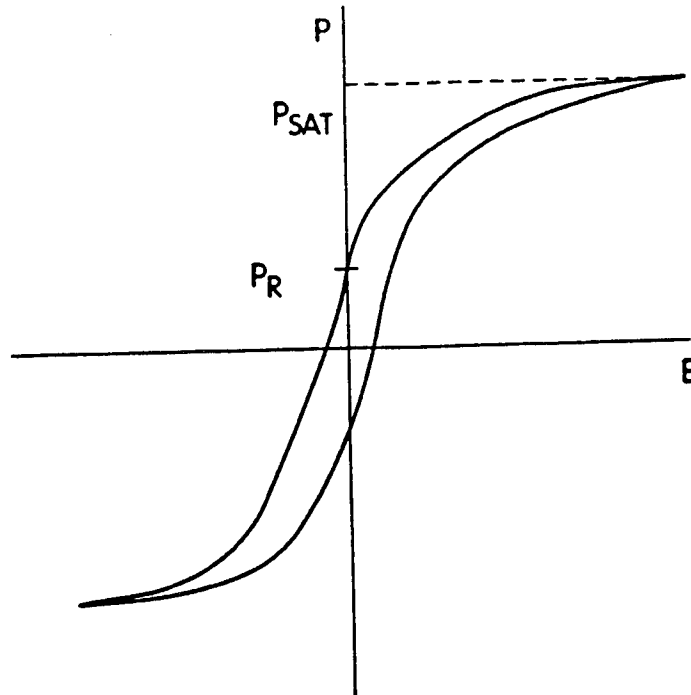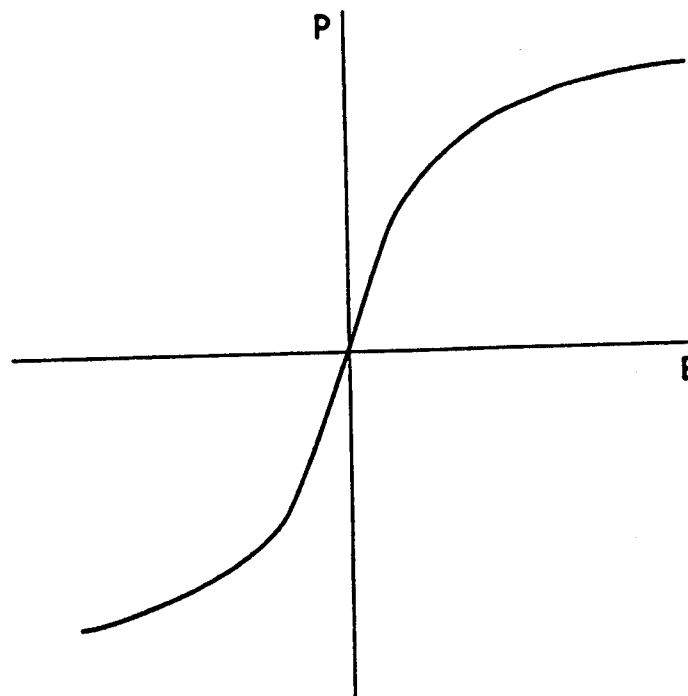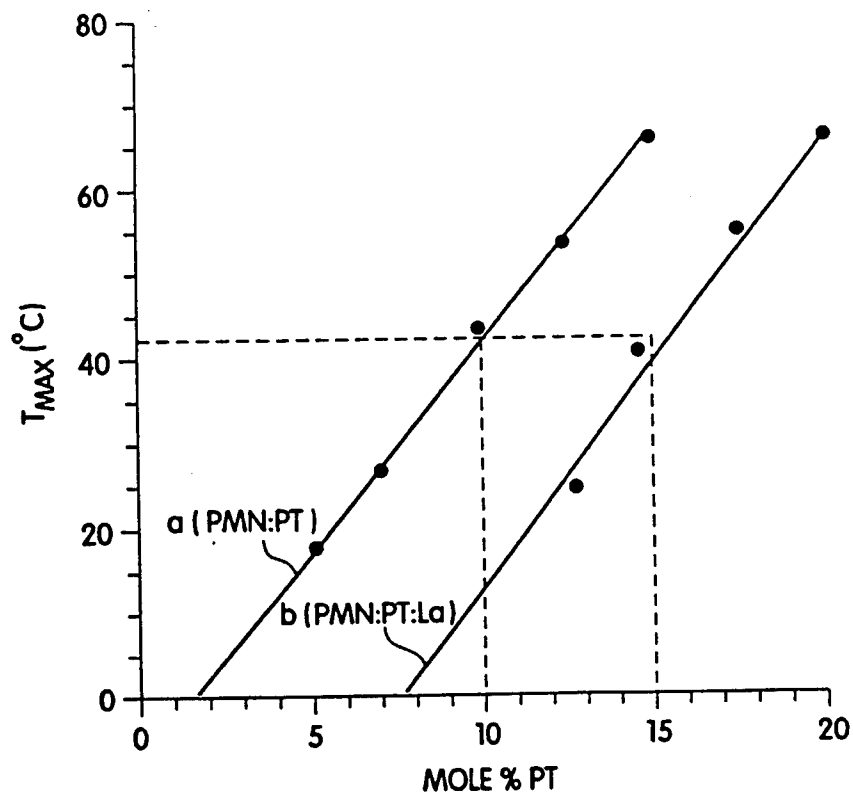
Fig. 1
(Prior Art)

Fig. 2
(Prior Art)

Fig. 3

Fig. 4

Fig. 5

Fig. 6

Fig. 7

Fig. 8

Fig. 9

Fig. 10

Fig. 14

- - - - - WITHOUT DC BIAS
———— WITH DC BIAS

Fig. 11
(Prior Art)

- - - - - WITHOUT DC BIAS
———— WITH DC BIAS

Fig. 12

Fig. 13

Fig. 15

PMN - PT RODS

POLYMER MATRIX

Fig. 16a

PMN - PT   POLYMER
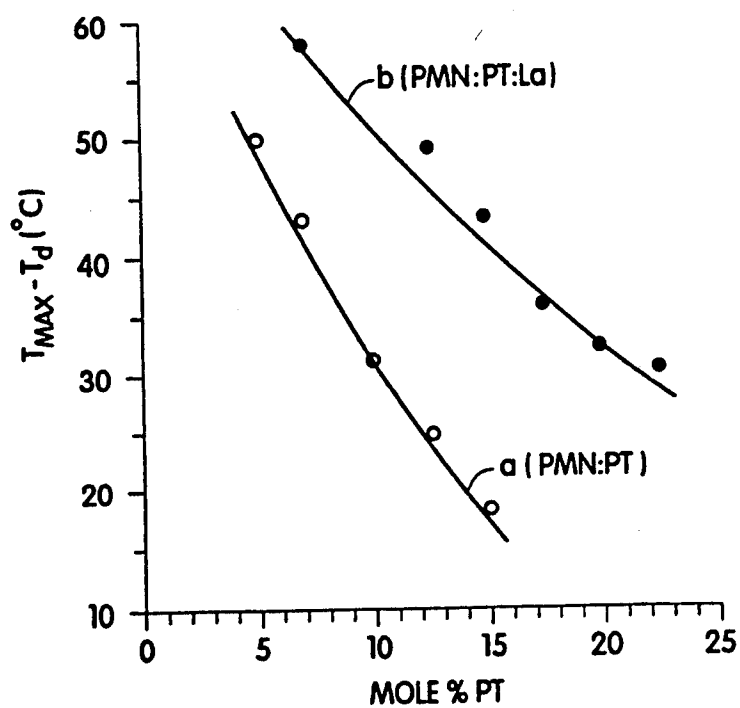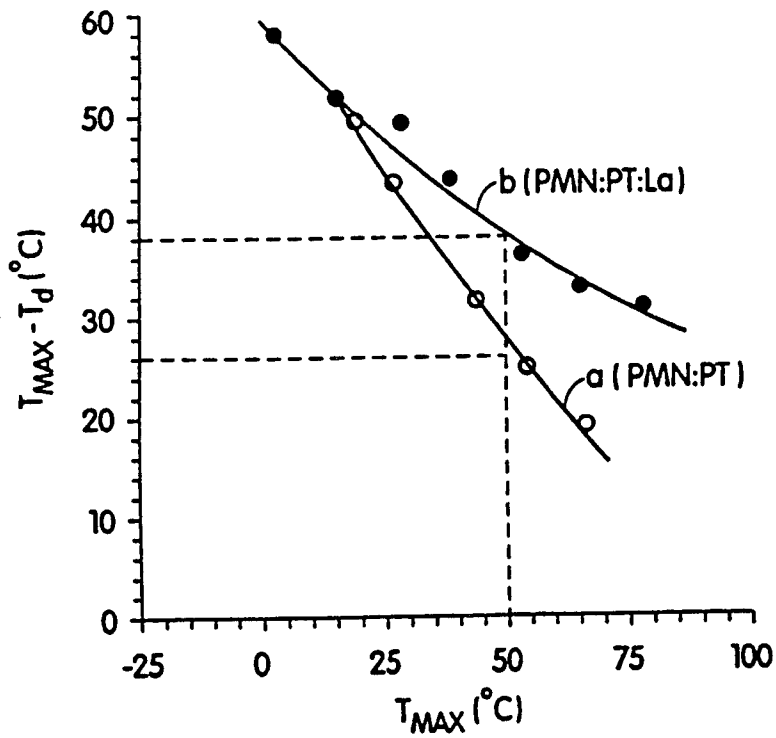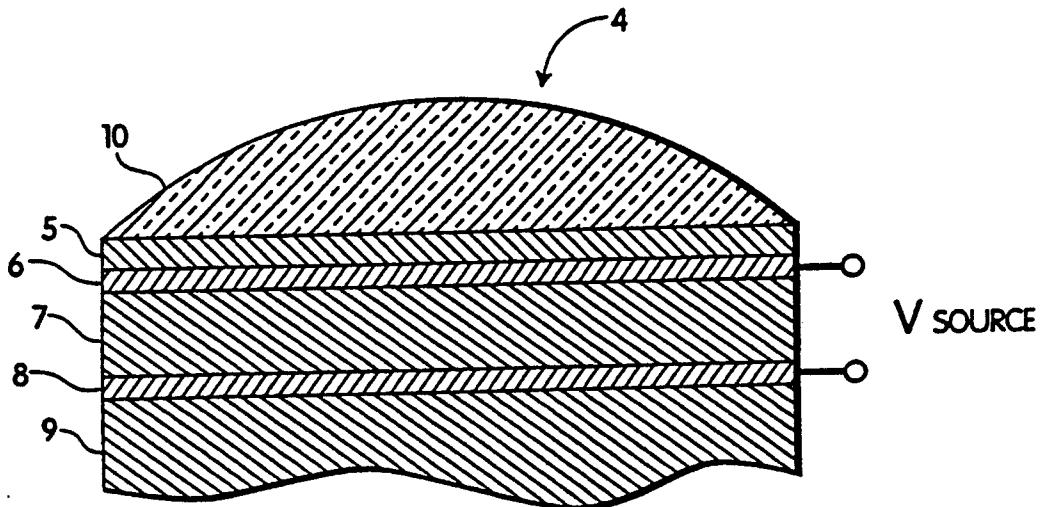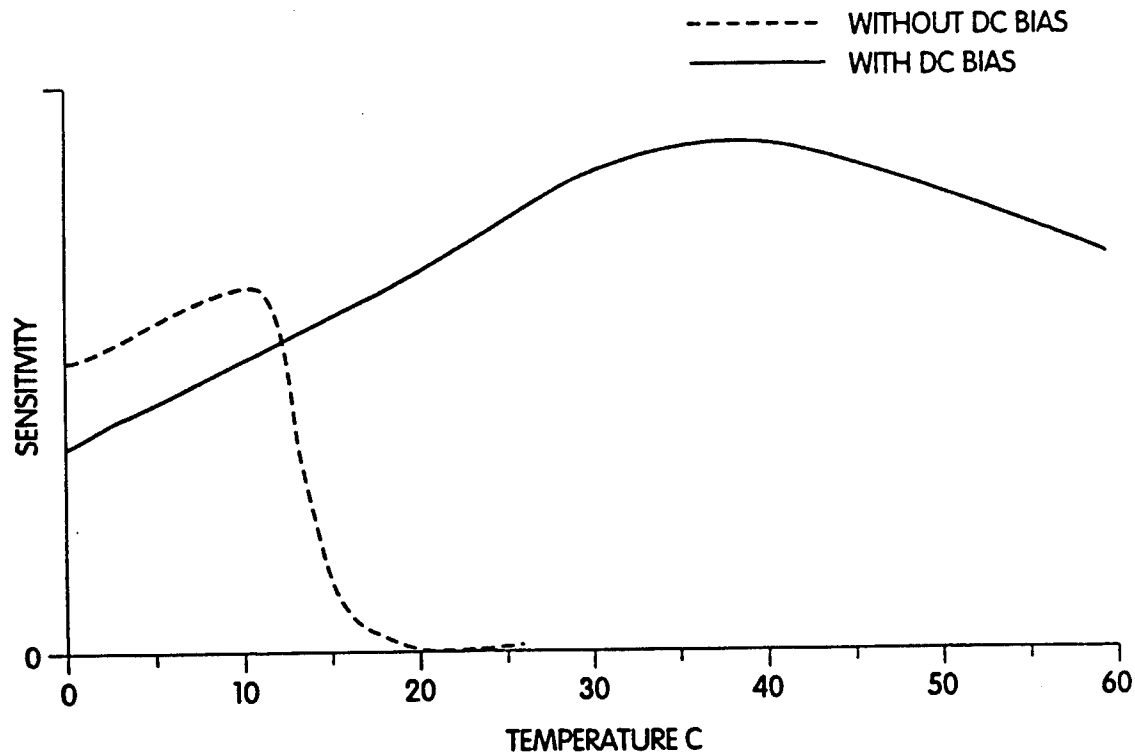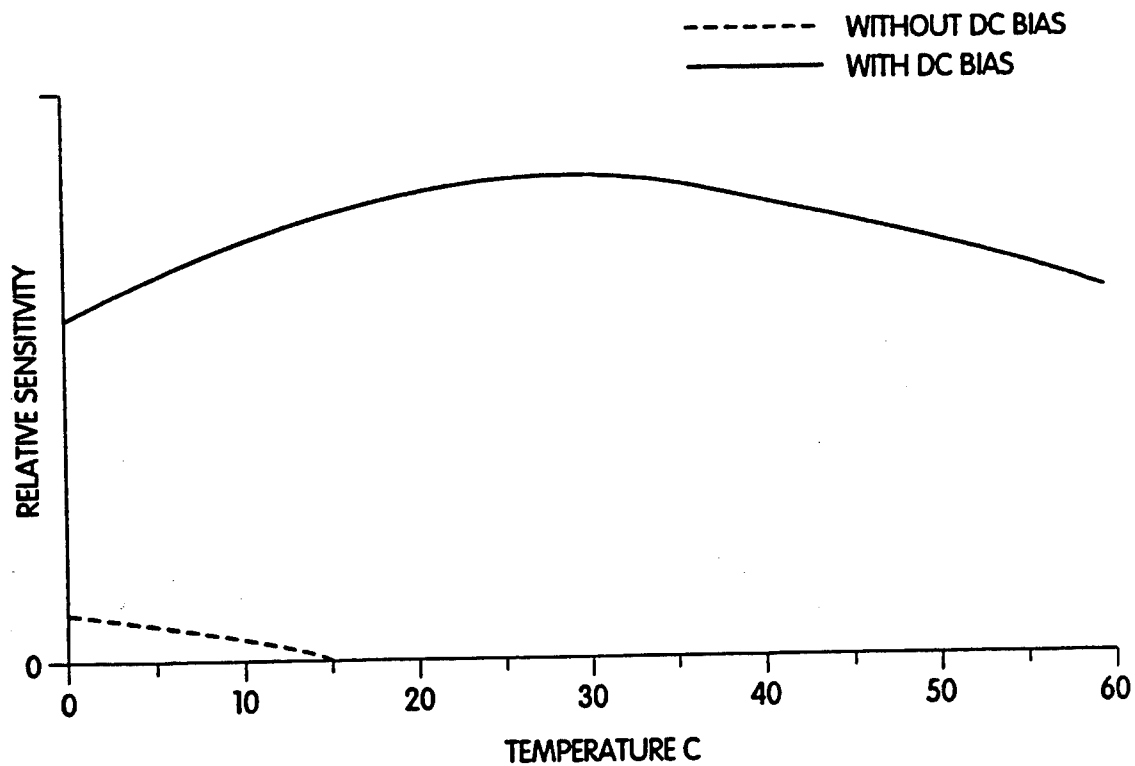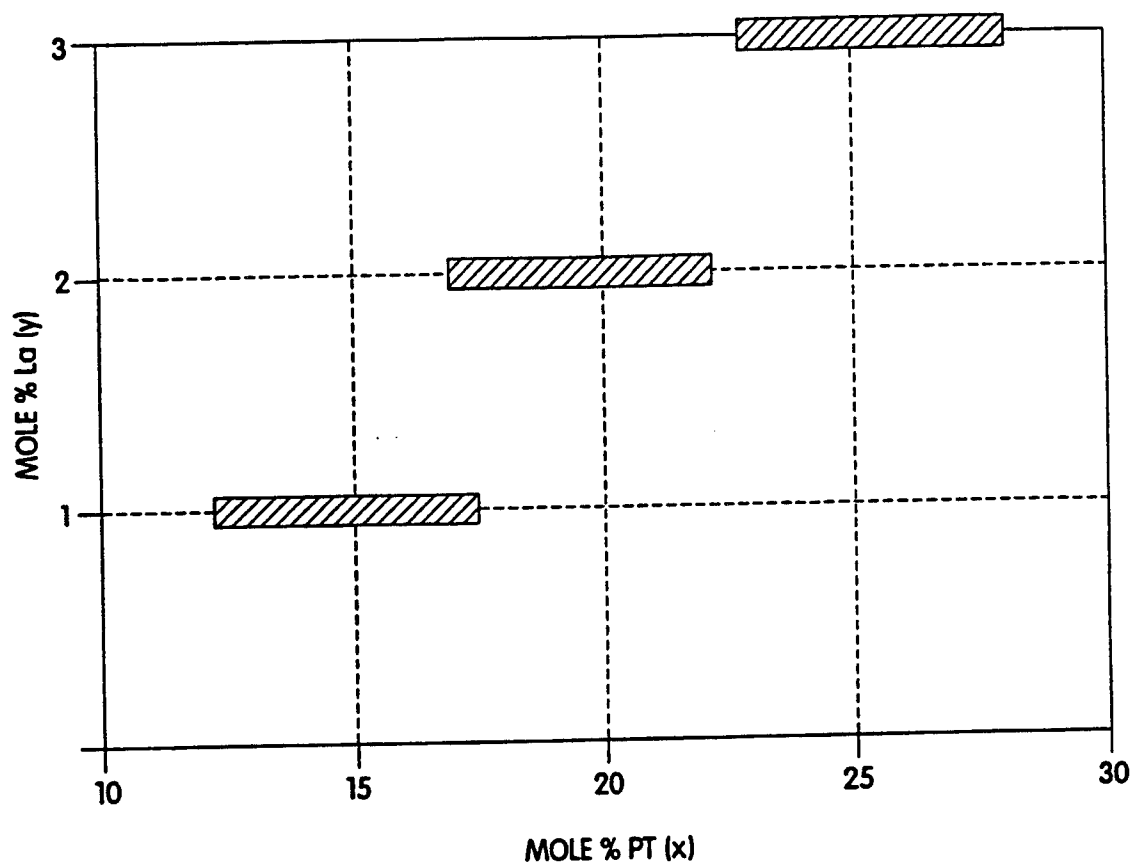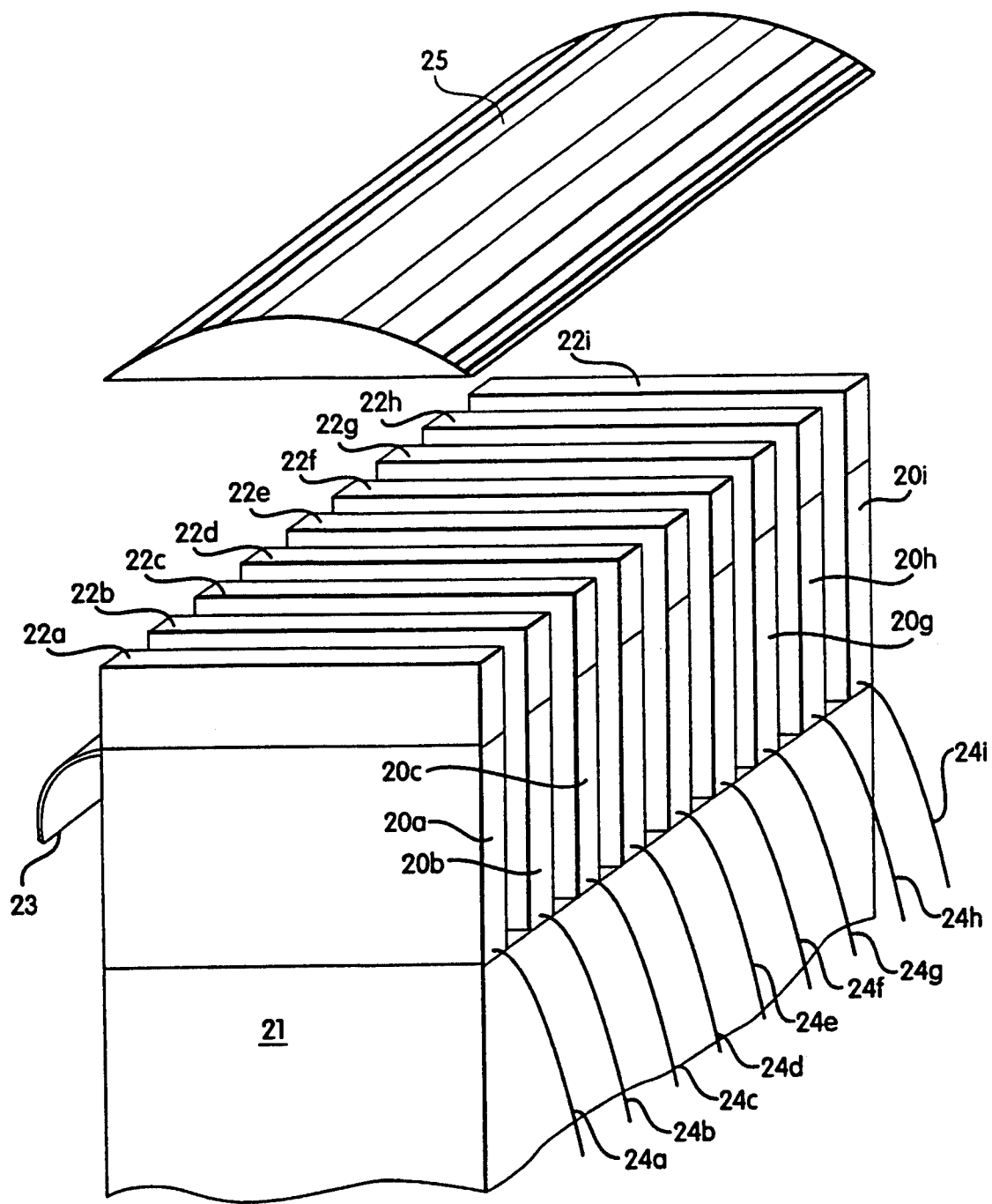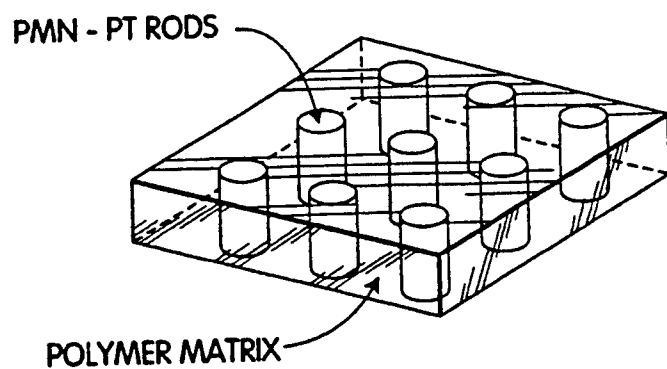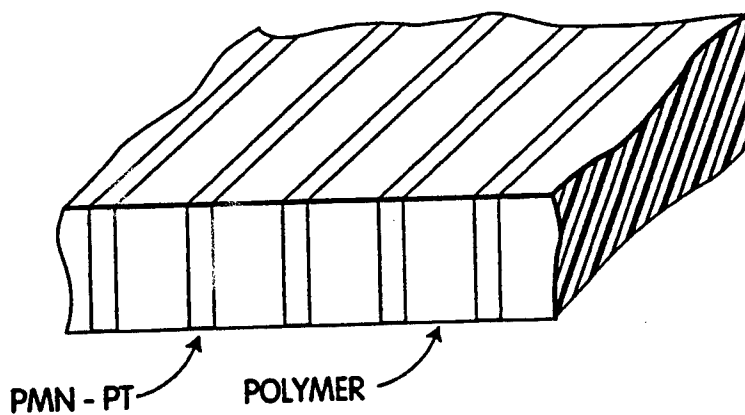
Fig. 16b

ELECTROSTRICTIVE ULTRASONIC PROBE HAVING EXPANDED OPERATING TEMPERATURE RANGE

FIELD OF THE INVENTION

This invention relates to ultrasonic transducers and, more particularly, to an ultrasonic transducer made from a relaxor ferroelectric solid solution which provides an expanded operating temperature range, preferably in the vicinity of room temperature.

BACKGROUND OF THE INVENTION

Ultrasonic transducers, which transmit and receive ultrasonic waves, enable one to view the interior of an object noninvasively. They have a wide variety of applications—a major use being ultrasonic imaging of the human body as a medical diagnostic tool.

Ultrasonic transducers utilize piezoelectric properties to convert electrical energy into mechanical energy (i.e., an electrical signal applied to the transducer generates a mechanical sound wave which is sent into the body), and vice versa, convert mechanical energy back into electrical energy (i.e., the sound wave reflected off an internal organ is converted back to an electrical signal and sent to an imaging device). The more efficiently the transducer performs This energy conversion, the stronger the signal. Two important measures of the strength and sensitivity of the transducer material are the electromechanical coupling factor k_t and dielectric constant K.

Another important factor in medical ultrasonic imaging is the stability and reproducability of the response over the operating temperature range. Medical transducers are intended to operate at room temperature (i.e., about 25° C.). However, in practice the temperature in the room may actually be much lower (e.g., 15° C. or lower), and the probe may heat up during normal use to a much higher temperature (e.g., 40° C. and above). These temperature variations can have a substantial effect on the transducer output for materials whose electromechanical properties are temperature dependent.

Ultrasonic transducers for medical applications have been fabricated from piezoelectric materials such as lead zirconate titanate (PZT) ceramics. It is also known to fabricate transducers from a material which is highly polarizable by application of a D.C. bias voltage, the material thereby exhibiting piezoelectric properties. The material loses its polarization upon removal of the D.C. bias voltage and no longer exhibits piezoelectric properties. This property of tuning the piezoelectric effect ON or OFF by the presence or absence of a D.C. bias voltage can be observed, for example, in materials which are preferably maintained in the vicinity of their ferroelectric to paraelectric phase transition temperatures. The ferroelectric phase exhibits piezoelectric properties whereas the paraelectric phase does not. Materials having the above described D.C. bias voltage dependent properties are referred to herein as "electrostrictive" materials.

Conventional ultrasonic transducers use piezoelectric materials which exhibit a remanence in polarization after the applied D.C. bias is removed. Thus the piezoelectric activity and consequently the sensitivity of the transducer is a constant, and does not change appreciably with temperature. However, using an electrostrictive material, one can provide a transducer with controllable sensitivity which makes it suitable for such applications as a variable aperture probe, e.g., wherein an ultrasonic beam is electronically scanned in the X-direction and controlled in the Y-direction by a bias voltage. Another application is a two-dimensional array, e.g., a crossed-array electrode type 2D probe, wherein the piezo-active region can be selected in space and in time by D.C. bias field switching and a selected region is mechanically isolated by a passive polymer.

Several material families have been evaluated as potential candidates for electro-strictire transducer application. Two examples of such materials include lead-magnesium-niobate modified with lead titanate (PMN-PT), and barium-strontium-titanate (BST). The temperature dependence of polarization and dielectric constant for these different electrostrictive materials is illustrated in FIGS. 1-2.

The temperature dependent behavior of BST is illustrated in FIG. 1. This is a material having "normal" ferroelectric behavior, that is, the temperature of the dielectic maxima T_{max} substantially coincides with disappearance of polarization T_d. Thus below T_{max}, BST exhibits a stable remanent polarization after the applied D.C. bias is removed. Such remanence in polarization defeats the goal of providing a transducer with controllable sensitivity. To operate above T_{max}, BST requires a relatively large electric field to achieve the required polarization and is thus difficult to make into a practical device where the goal is to minimize the field applied to the transducer from the consideration of patient safety.

Another type of electrostrictive material is a "relaxor" ferroelectric, e.g., PMN—PT. In relaxor ferroelectric materials, the temperature of the dielectric maxima T_{max} is substantially higher than the temperature corresponding to the disappearance of polarization T_d. Thus, the operating temperature range for a PMN—PT type of material is between T_d and T_{max} as illustrated in FIG. 2. PMN is a relaxor material having a diffuse phase transition, which produces a broadened dielectric maxima. PT, a normal ferroelectric, forms a solid solution with the relaxor PMN; the amount of PT can be increased to increase T_{max}. However, this does not increase the operating temperature range, but simply shifts it upwardly. A PMN—PT solid solution having approximately 90 mole % PMN and 10 mole % PT has been proposed for use as an ultrasonic transducer, having an operating temperature range of about 25° C. around room temperature (i.e., a T_d of 15° C. and T_{max} of 40° C.). However, this may not be sufficient for use in a much cooler room, or when the device heats up.

It is an object of this invention to provide an electrostrictive transducer material having an expanded operating temperature range, and relatively small variations of sensitivity with temperature.

SUMMARY OF THE INVENTION

An electrostrictive material has been found having a broad operating temperature range, which range may be in the vicinity of room temperature, making it very suitable for ultrasonic transducer applications. The material comprises a select composition range of lanthanum doped PMN-PT solid solutions, and the resulting operating range may be effectively doubled to about 48° C. The doping will provide an ample margin on each side of a desired operating temperature, for example room temperature (25° C.). This select composition range also provides lower variations in transducer sensi-

tivity with temperature than prior art materials used in the fabrication of electrostrictive transducers.

Compositions suitable for use in practicing this invention include a solid solution of lead magnesium niobate PMN and lead titanate PT which is doped with lanthanum La in accordance with the following formula I:
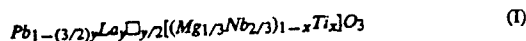
$$Pb_{1-(3/2)y}La_y\square_{y/2}[(Mg_{1/3}Nb_{2/3})_{1-x}Ti_x]O_3 \qquad (I)$$

wherein x and y are on the order of

$10 \leqq x \leqq 30$ mole %

$0.5 \leqq y \leqq 3$ mole %

and $\square$ represents a vacancy at the Pb site.

By varying x, which represents the PMN:PT ratio within formula I, there is a resulting change in temperature T_{max}, and a change in the optimum amount of lanthanum doping and resulting operating range. For transducers having an expanded operating temperature range around room temperature, (i.e., about 25° C.) the preferred ranges are selected from the following:

(a) y on the order of 1 mole % and x is on the order of 12.5–17.5 mole %;

(b) y on the order of 2 mole % and x is on the order of 17–22 mole %; and

(c) y on the order of 3 mole % and x is on the order of 23–28 mole %.

A specific preferred composition described in this application has on the order of x = 15 mole % PT and on the order of y = 1 mole % La, and exhibits a 48° C. operating range of from −7° C. to 41° C.

Another specific composition, having a lower temperature limit, has on the order of x = 13.5 mole % PT and on the order of y = 1 mole % La, and exhibits a 46° C. operating range of from −15° C. to 31° C.

Still another specific composition, having a higher temperature limit, has on the order of x = 17.5 mole % PT and on the order of y = 1 mole % La, and exhibits a 33° C. operation range of from 18° C. to 55° C.

In another aspect of the invention there is provided a method of expanding the operating temperature range of an electrostrictive transducer, wherein the mole % of PT and mole % of La are selected to produce the combined lower and upper limits of a broadened operating temperature range for a particular transducer application.

BRIEF DESCRIPTION OF THE DRAWINGS

FIG. 1 is a graph showing the temperature dependence of the remanent polarization P_R and dielectric constant K for a "normal" ferroelectric material (BST);

FIG. 2 is a graph showing the temperature dependence of the remanent polarization P_R and dielectric constant K for a "relaxor" ferroelectric material (PMN—PT);

FIG. 3 is a graph of the dielectric constant K versus temperature for PMN—PT;

FIG. 4 is a graph of the thickness coupling coefficient k_t versus temperature for PMN—PT at a given D.C. bias;

FIG. 5 is a graph of the remanent polarization P_R versus temperature for PMN—PT;

FIG. 6 is a graph showing hystersis (remanent polarization) in PMN—PT when the electric field is withdrawn;

FIG. 7 is a graph showing substantially no hysteresis in PMN—PT when the electric field is withdrawn;

FIG. 8 is a graph showing the change in T_{max} measured at 1 kHz for a PMN—PT system with increasing mole % PT, with and without 1 mole % La; to achieve

a given T_{max}—e.g., about 40° C., compound (a) will have 90:10 of PMN:PT, and compound (b) will have 85:15 of PMN:PT and 1 mole % La;

FIG. 9 is a graph showing the operating temperature range $(T_{max}-T_d)$ for PMN—PT with and without 1 mole % La;

FIG. 10 is a graph of T_{max} vs. $T_{max}-T_d$ for PMN—PT with and without 1 mole % La, showing that for a given T_{max}, say 50° C., there is a significant difference in $T_{max}-T_d$;

FIG. 11 is a graph showing the sensitivity change with temperature for a prior art PMN—PT composition with and without D.C. bias; note that the remanence in sensitivity exists up to 20° C.;

FIG. 12 is a graph showing the greatly reduced sensitivity change with temperature for a PMN—PT composition of this invention with and without D.C. bias; note that the remanance in sensitivity (w/o D.C. bias) is pushed to a lower temperature;

FIG. 13 is a graph showing the preferred PMN—PT composition ranges of this invention;

FIG. 14 is a cross-sectional view of an ultrasonic probe incorporating the PMN—PT composition of this invention;

FIG. 15 is a perspective view of an ultrasonic probe having an array of transducer elements made from the PMN—PT composition of this invention;

FIG. 16a is a schematic representation of a 1:3 PMN—PT rod:polymer composite made from the PMN—PT composition of this invention; and

FIG. 16b is a schematic representation of a 2:2 PMN—PT:polymer composite.

DETAILED DESCRIPTION

According to the present invention, an electrostrictive material is provided consisting of a select range of lanthanum doped PMN—PT solid solutions which enable the production of an ultrasonic probe having an expanded operating temperature range and reduced temperature sensitivity. In order to illustrate the problem of temperature sensitivity, FIGS. 3–5 show the temperature dependence of various properties of a PMN—PT system.

FIG. 3 shows the variation of dielectric constant K with temperature T. Note that K has a relatively broad (diffuse) peak centered at T_{max}.

FIG. 4 shows the variation in thickness coupling coefficient k_t at a given D.C. bias with temperature T. The coupling coefficient is relatively constant at lower temperatures, and then drops off near T_{max}. For optimum coupling efficiency and highest sensitivity, it would be desirable to operate below T_{max}.

FIG. 5 shows the remanent polarization P_R as a function of temperature. The remanent polarization drops off at T_d. Zero remanent polarization is desired for a transducer which can be switched ON and OFF without hysteresis. Thus, it would be desirable to operate above T_d to utilize the tunable sensitivity in an electrostrictive transducer.

From the above considerations, it is clear that the operating temperature range for an electrostrictive material is between T_{max} and T_d.

FIG. 6, a plot of polarization P versus electric field E, shows a material having undesirable hysteresis (remanent polarization) at the operating temperature. As the electric field is increased, the domains are organized and the polarization increases until it saturates at P_{sat}.

When the electric field is removed, the polarization does not return to zero but rather a remanent polarization P_R remains, i.e., the transducer cannot be fully turned off. In contrast with FIG. 6, the desired non-hysteresis behavior is shown in FIG. 7. Here when the electric field is turned off, the polarization returns to zero. There is complete control (and reproducibility) over the polarization by changing the applied field.

It would be desirable to expand the operating temperature range $(T_{max} - T_d)$ where the material exhibits a fully controllable and reproducible polarization (between ON, OFF and a variable amplitude therebetween). It has been suggested to raise T_{max} by increasing the mole % of PT. However, this just shifts the operating range higher, without expanding it.

In accordance with this invention it has been found that the operating temperature range of an electrostrictive ultrasonic transducer can be expanded by fabricating the transducer from a PMN—PT solid solution that has been doped with lanthanum. In a specific embodiment, 1 mole % La is added to various PMN:PT compositions as set forth in the following Table 1, to provide the designated increase in operating temperature range (i.e., $T_{max} - T_d$). The thickness coupling coefficient k_t as set forth in Table 1 was measured at two applied field strengths (5 kV/cm and 10 kV/cm), and at three operating temperatures (0°, 25° and 50° C.). The remanent coupling factor k_{trem} (with zero applied field) was also measured, along with the saturation field E_{sat}. The data from Table 1 is plotted in FIGS. 8–10.

FIG. 10 compares the operating temperature range $(T_{max} - T_d)$ to T_{max} for the same prior art and inventive compositions (curves a and b respectively). For a defined T_{max} of 50° C. as shown, the operating range of the composition of this invention (curve b) is substantially greater than that of curve a.

FIG. 11 is a graph showing the sensitivity change with temperature for the same prior art PMN—PT composition (PMN:PT of 90:10) with and without D.C. bias. There is an undesirable remanence in sensitivity up to about 20° C. Also, there is a significant undesirable variation in sensitivity with temperature (with D.C. bias).

FIG. 12 illustrates the significant improvement in performance, compared to the compound described in FIG. 11, of a preferred composition of this invention (PMN:PT:La of 85:15:1) in the vicinity of room temperature. The remanence (without D.C. bias) is pushed to a lower temperature (about 15° C.). The level of remanence relative to sensitivity with DC bias is substantially small even at 0° C. For the prior art composition (FIG. 11), the sensitivity without DC bias (remanant sensitivity) is higher than the sensitivity with DC bias up to approximately 13° C. In contrast, for the composition of this invention (FIG. 12) the sensitivity curve (with D.C. bias) is substantially flatter, signifying a more constant relative pulse-echo sensitivity over an expanded operating temperature range in the vicinity of room temperature.

The compositions were made and tested as substan-

TABLE 1

Field-Induced Thickness Coupling Factor k_t Data for PMN-PT Compositions With 0 and 1 Mole % La at 0, 25 and 50° C.

Sample	y mole % La	x mole % PT	T_d °C.	T_{max} °C.	$T_{max} - T_d$ °C.	k_t 5 kV/cm (0°)	k_t 10 kV/cm (0°)	k_{trem} (0°)	E_{sat} (kV/cm) (0°)	k_t 5 kV/cm (25°)	k_t 10 kV/cm (25°)	k_{trem} (25°)	E_{sat} (kV/cm) (25°)	k_t 5 kV/cm (50°)	k_t 10 kV/cm (50°)	k_{trem} (50°)	E_{sat} (kV/cm) (50°)
a)	0	0.10	15	40	25	0.43	0.45	0.40	2–3	0.48	0.48	0	3–4	0.37	0.44	0	5–6
b)	0	0.125	30	52	22	0.41	0.43	0.40	2–3	0.46	0.45	0.37	3–4	0.47	0.48	0	6
c)	0	0.15	48	68	20	0.45	0.46	0.42	3	0.46	0.47	0.42	3	0.47	0.48	0	3–4
d)	1	0.125	−20	24	44	0.35	0.44	0	5–6	0.34	0.45	0	8–9	0.3	0.39	0	9–1
e) •	1	0.135	−15	30	45	—	—	—	—	—	—	—	—	—	—	—	7
f)	1	0.15	−7	41	48	0.43	0.45	0	4–5	0.41	0.47	0	7–8	0.34	0.44	0	8–9
g)	1	0.175	18	55	33	0.43	0.46	0.41	4–5	0.47	0.46	0.05	5–6	0.45	0.46	0	7–8
h)	1	0.20	34	66	32	0.44	0.46	0.40	3–4	0.46	0.47	0.31	5–6	0.46	0.47	0	7–8
i)	1	0.225	49	78	29	0.45	0.48	0.41	3–4	0.47	0.48	0.37	4–5	0.47	0.48	0.15	5–6

• Interpolated

Compositions e and f of this invention exhibited zero remanent polarization at all three temperatures. Composition f (85% PMN, 15% PT, 1% La) had the broadest operating range (48° C.), with an ample allowance on each side of room temperature, i.e., −7° to 41° C. Composition e had the lowest T_d (−20° C.), while still having a sufficient margin above 25° C., for a total range of 44° C. Composition g had the highest T_{max} (55° C.), while still having a sufficient margin below 25° C., for a total operating temperature range of 33° C.

FIG. 8 compares the effect of mole % PT on T_{max} (at 1 KHZ), for the prior art composition without La (curve a: PMN:PT of 90:10), and for the composition of this invention (curve b: PMN:PT:La of 85:15:1). For a defined T_{max}, as shown, the optimum mole % PT differs between curves a and b.

FIG. 9 compares the effect of mole % PT on the operating temperature range $(T_{max} - T_d)$, for the prior art composition without La (curve a: PMN:PT of 90:10) and for the composition of this invention (curve b: PMN:PT:La of 85:15:1).

tially described in N. Kim et al., "Dielectric and Piezoelectric Properties of Lanthanum-Modified Lead Magnesium Niobium-Lead Titanate Ceramics," *Ferroelectrics*, 1989, Vol. 93, pp. 341–349, which is incorporated herein by reference.

Other preferred compositions of this invention are shown in FIG. 13, within the desired ranges of x on the order of 10–30 mole % and y on the order of 0.5–3 mole %. The three preferred room temperature operating range compositions are:

(a) y on the order of 1 mole % and x on the order of 12.5–17.5 mole %;

(b) y on the order of 2 mole % and x on the order of 17–22 mole %; and

(c) y on the order of 3 mole % and x on the order of 23–28 mole %.

FIG. 14 shows one embodiment of a medical ultrasonic imaging probe 4 for transmitting and receiving ultrasonic energy incorporating the transducer material of this invention. The probe has a relatively thick, impedance-matching backing layer 9, i,e., a damping

layer with an appropriate acoustic impedance to optimize the sensitivity, bandwidth or pulse length of the transducer. The transducer 7 has electrical conducting contact layers 6 and 8 on its opposing sides, and the composite is mounted on top of the backing layer 9. The bias and excitation voltages are applied across the transducer layer 7 as shown. An impedance matching layer (or layers) 5 may be provided above the transducer and finally a lens 10 above layer 5 for focussing the acoustic beam. Acoustic energy generated in the transducer array is transmitted through the impedance matching layer 5, focussed by lens 10 and sent into the object under examination, i.e., the human body.

Alternatively, the probe may include an array of tens or hundreds of transducer elements arranged on a backing layer, each element being physically separated so it can be individually energized (FIG. 15). In this embodiment, separate parallel and spaced transducer elements 20a et seq. are arranged between backing material 21 and separate acoustic matching layers 22a et seq. The field is applied by common electrode 23 and a plurality of connections 24a et seq. for poling in the designated thickness direction. An acoustic lens 25 is provided above acoustic matching layers 22.

The transducer of this type may have applications other than as a probe with controllable sensitivity, as previously described. Other applications include use as a variable aperture probe, e.g., an ultrasonic beam is electronically scanned in the X-direction and controlled in the Y-direction by a bias voltage. Another application is as a two-dimensional array, e.g., a crossed-array electrode type 2D probe, wherein the piezo-active region can be selected in space and in time by a DC bias field switching and a selected region is mechanically isolated by a passive polymer. It may also be desirable to utilize the lanthanum doped PMN—PT compositions of this invention as a composite material (i.e., mixed with a polymer such as epoxy or polyurethane) in order to, for example, improve coupling of acoustic energy from the transducer to the body, or to reduce unwanted lateral vibrations when used in array ultrasonic transducers. Such a composite configuration is shown in FIGS. 16a and 16b, wherein the PMN—PT composition of this invention is provided as rods in a 1:3 rod:-polymer composite (FIG. 16a), or as layers in a 2:2 PMN—PT:polymer composite (FIG. 16b).

While there have been shown and described what are presently considered the preferred embodiments of the present invention, it will be obvious to those skilled in the art that various changes may be made therein without departing from the scope of the invention as defined by the appended claims. For example, while the preferred embodiment was directed towards increasing the stability and sensitivity with temperature of an electrostrictive ultrasonic transducer operated in the vicinity of room temperature (25° C.), similar benefits may be realized for operating temperatures above or below room temperature through modifications of the ratios of PMN, PT and lanthanum.

What is claimed is:

1. In an ultrasonic probe having an electrostrictive transducer for transmitting and receiving ultrasonic energy, and having electrical contacts attached to the transducer for connection to a source that selectively applies an electric field to the transducer, the improvement comprising:

the transducer being fabricated from a material comprising a solid solution of lead magnesium niobate

PMN and lead titanate PT and being doped with lanthanum La according to the formula:
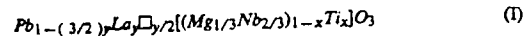
$$Pb_{1-(3/2)y}La_y\square_{y/2}[(Mg_{1/3}Nb_{2/3})_{1-x}Ti_x]O_3 \qquad (I)$$

wherein x and y are on the order of

$10 \leqq x \leqq 30$ mole %

$0.5 \leqq y \leqq 3$ mole %.

and $\square$ represents a vacancy at the Pb site, wherein the transducer provides an expanded operating temperature range.

2. The probe of claim 1, wherein the transducer provides an expanded operating temperature range around room temperature and includes a solid solution selected from the group consisting of:

(a) y on the order of 1 mole % and x on the order of 12.5–17.5 mole %;

(b) y on the order of 2 mole % and x on the order of 17–22 mole %; and

(c) y on the order of 3 mole % and x on the order of 23–28 mole %.

3. The probe of claim 2, wherein x is on the order of 15% and y is on the order of 1%.

4. The probe of claim 2, wherein x is on the order of 17.5% and y is on the order of 1%.

5. The probe of claim 2, wherein x is on the order of 13.5% and y is on the order of 1%.

6. The probe of claim 1, wherein the transducer comprises a composite of polymer and the PMN:PT:La solid solution.

7. An electrostrictive transducer for transmitting and receiving ultrasonic energy, comprising:

a backing layer;

at least one electrostrictive transducer element disposed on the backing layer; and

electrical contacts attached to the transducer element and connectable to a source for selectively producing electric fields in the transducer element,

wherein the transducer is fabricated from a material comprising a solid solution of lead magnesium niobate PMN and lead titanate PT and is doped with lanthanum La according to the formula:
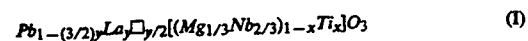
$$Pb_{1-(3/2)y}La_y\square_{y/2}[(Mg_{1/3}Nb_{2/3})_{1-x}Ti_x]O_3 \qquad (I)$$

wherein x and y are on the order of

$10 \leqq x \leqq 30$ mole %

$0.5 \rightarrow y \leqq 3$ mole %.

and $\square$ represents a vacancy at the Pb site, wherein the transducer provides an expanded operating temperature range.

8. The transducer of claim 7, wherein the transducer provides an expanded operating temperature range around room temperature and includes a solid solution selected from the group consisting of:

(a) y on the order of 1 mole % and x on the order of 12.5–17.5 mole %;

(b) y on the order of 2 mole % and x on the order of 17–22 mole %; and

(c) y on the order of 3 mole % and x on the order of 23–28 mole %.

9. The transducer of claim 8, wherein x is on the order of 13.5 to 17.5 mole % and y is on the order of 1 mole %.

10. A method of expanding the operating temperature range of an ultrasonic probe comprising:

providing an electrostrictive transducer for transmitting and receiving ultrasonic energy, and electrical

9

contacts attached to the transducer for connection to a source that selectively applies an electric field to the transducer, wherein the transducer comprises a solid solution of lead magnesium niobate PMN and lead titanate PT; and

selecting the relative mole % of PMN and PT and doping with a mole % lanthanum La according to the formula:

$$Pb_{1-(3/2)y}La_y\square_{y/2}[(Mg_{1/3}Nb_{2/3})_{1-x}Ti_x]O_3 \quad (I)$$

wherein x and y are on the order of
$10 \leq x \leq 30$ mole %
$0.5 \leq y \leq 3$ mole %.

10

and $\square$ represents a vacancy at the Pb site, in order to expand the operating temperature range.

11. The method of claim 10, wherein the transducer provides an expanded operating temperature range around room temperature and includes solid solutions selected from the group consisting of:

(a) y on the order of 1 mole % and x on the order of 12.5–17.5 mole %;

(b) y on the order of 2 mole % and x on the order of 17–22 mole %; and

(c) y on the order of 3 mole % and x on the order of 23–28 mole %.

12. The method of claim 11, wherein x is on the order of 13.5 to 17.5 mole % and y is on the order of 1 mole %.

* * * * *

APPENDIX 65

EFFECT OF EUTECTIC LITHIUM SULFATE-SODIUM SULFATE FLUX ON THE SYNTHESIS OF LEAD MAGNESIUM NIOBATE

K. H. YOON, Y. S. CHO and D. H. KANG†

Department of Ceramic Engineering, Yonsei University, Seoul 120-749, Korea

and

K. UCHINO and K. Y. OH

*Materials Research Laboratory, Pennsylvania State University,
University Park, Pennsylvania 16802 USA*

The effect of the amount of sulfate flux (Li_2SO_4-Na_2SO_4) on the phase stability and dielectric properties of lead magnesium niobate ceramics prepared by molten salt synthesis, has been studied as a function of calcining and sintering temperatures. The percentage of perovskite phase tended to increase with increasing the amount of flux and calcination temperature. When powders containing the same amount of flux with respect to starting oxides were calcined at 750°C for 2 h, the pyrochlore phase was about 2%. Above 800°C, the perovskite phase was stable at about 97% regardless of the amount of flux. However, the increase of the amount of sulfate flux resulted in an increase of the average particle size and a decrease of dielectric constant. These results can be explained by the sinterability and microstructure analysis.

*Keywords: molten salt, particle size, perovskite phase, dielectrics, microstructure,
$Pb(Mg_{1/3}Nb_{2/3})O_3$*

INTRODUCTION

There have been many studies in $Pb(Mg_{1/3}Nb_{2/3})O_3$ (PMN) and PMN based materials because of their high dielectric constant and electrostrictive strain coefficient.[1,2] Many processing methods for various applications, e.g., multilayer capacitors and electrostrictive devices, have been introduced.[3-6] Molten salt synthesis (MSS) process is one of the preparation processes for obtaining high purity powders at a relatively low temperature with the control of powder morphology. The reaction between oxides can be accelerated by adding a proper salt which behaves as a flux at its melting point. A number of salts such as KCl, NaCl-KCl and Li_2SO_4-Na_2SO_4 have been used in various ferrite systems.[7] In addition, molten salt synthesis using chloride flux has recently been used to form single phase complex perovskite compounds which include $PbNb_2O_6$, $BaTiO_3$, PMN and PFN etc.[8-11]

In this study, an eutectic composition, $0.635Li_2SO_4$-$0.365Na_2SO_4$ is used because of a lower melting point, 594°C compared to the melting point of chloride salt.

---

†Permanent address: Department of Electronic Materials Engineering, The University of Suwon, Suwon, Korea.

This paper describes the effects of the amount of the flux on perovskite phase and powder morphology in molten salt synthesis using Li_2SO_4-Na_2SO_4. Also, the influences of particle size on sinterability and dielectric properties of PMN ceramics are investigated.

EXPERIMENTAL PROCEDURE

Lead magnesium niobate ceramics were prepared by molten salt synthesis (MSS) method using sulfate flux.[10] The eutectic composition of $0.635Li_2SO_4$-$0.365Na_2SO_4$ salts was prepared and mixed with reagent grade starting oxides, PbO, MgO and Nb_2O_5 according to W (wt. of salts/wt. of oxides). After milling the mixture in ethanol for 15 h with zirconia balls, the slurry was dried at 120°C. The dried powders in covered alumina crucibles were fired at temperatures from 650°C to 850°C for 2 h. The products were washed with deionized water several times until no free SO_4^{2-} ions were detected using a barium nitrate solution and then were dried at 120°C. The powders after washing were analyzed by atomic absorption spectroscopy and inductively coupled plasma (Labtest, Plasmascan 710) techniques in order to detect remaining impurities. Average particle size was determined by laser particle analyzer (Malvern S3.01). The powders were pressed into disks of 12 mm in diameter at a pressure of 1500 kg/cm² with the addition of a 1.5 wt% polyvinyl alcohol (PVA) solution as a binder. The pellets were buried in the powder of the same composition to minimize PbO loss during heating, and sintered in the air at temperatures ranging from 900°C to 1200°C for 4 h.

X-ray diffractometer (Rigaku, 290612 A14) with Cu-Kα radiation was used to determine the relative amount of the perovskite phase of calcined powders and sintered specimens as found in Reference 5. The microstructure of fracture surface for specimens was observed by SEM (ASI DS 130). Specimens for dielectric mea-

TABLE I

Percentage of perovskite phase synthesized in sulfate flux
(W = flux weight/PMN weight)

Calcination temp. \ W	0.2	1.0	2.0
650°C	3%	4%	3%
700°C	40%	39%	22%
750°C	93%	98%	97%
800°C	96%	97%	97%
850°C	97%	97%	97%

FIGURE 1 SEM photographs of PMN powders calcined at 800°C for 2 h in various sulfate fluxes, (A) W = 0.2, (B) W = 1.0 and (C) W = 2.0.

surement were prepared from sintered pellets by polishing the faces flat and by firing on silver electrodes at 750°C. The dielectric properties were measured at 100 Hz using a LCR meter (ANDO, AG4303) and a temperature controller cooling it from 100°C to −80°C.

TABLE II

Amount of impurities by AA and ICP analysis (wt%)

Impurity W	Li	Na	SO_4^{2-}
0.2	0.007	0.017	0.030
2.0	0.009	0.015	0.039

TABLE III

Characteristics of powders prepared at various conditions

Specimen Characteristics	SP	MP	LP
Calcination condition	800°C, 2h	800°C, 2h	800°C, 2h
Amount of flux(W)	0.2	1.0	2.0
Perovskite phase	96%	97%	97%
Average particle size	1.51 μm	1.98 μm	2.78 μm

RESULTS AND DISCUSSION

Table I shows the effect of the amount of flux on PMN phase synthesized in sulfate flux with calcination temperatures. In comparison to calcining of mixed oxides process,[3] molten salt synthesis (MSS) method made it possible to form a high purity PMN phase at a lower temperature such as 750°C. This is due to the small diffusion distances of constituent oxides and the high mobility of species in Li_2SO_4-Na_2SO_4 molten salts melted around ~600°C.[7] PMN phase having the pyrochlore phase of 2–3% was obtained above 750°C when W was over 1.0 and this pyrochlore phase was reduced to 1–2% for all specimens after sintering at 1200°C. However, for W = 0.2, the amount of PMN phase present was smaller compared to the case of the other amounts of flux. It is because the amount of flux was too small to promote the dispersibility and reactivity of the oxides effectively. No significant difference in perovskite phase was observed above 800°C regardless of the amount of flux. However, the perovskite phase of 100% was not obtained even with the increase of calcining temperature.

Figure 1 shows SEM photographs of PMN powders calcined at 800°C for 2 h with the variation of the amount of sulfate flux. With the increase of the amount of flux from W = 0.2 to W = 2.0, average particle size increased. This is attributed to the increase of spaces and rate for particle growth as the amount of sulfate flux
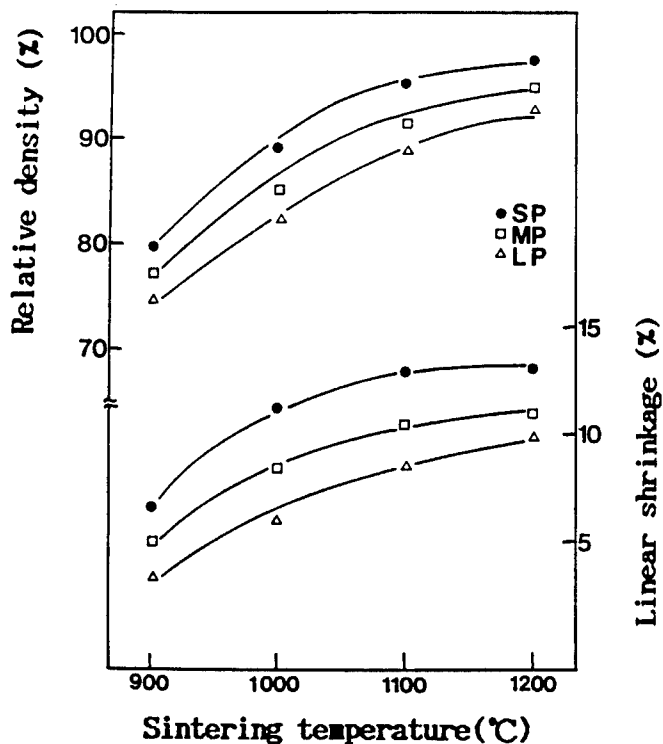
FIGURE 2   Relative density and linear shrinkage vs. sintering temperature for PMN specimens.

increases as well as the cases of Ni ferrite system studied by Kimura et al.[7] They reported that as the amount of sulfate flux increased the size of Ni-ferrite particles increased due to the increase of the reaction rate. But no significant differences in particle shape were observed with increasing the amount of flux. This suggests that the particle size of PMN was not determined by the growth process, but by the formation process regardless of the amount of flux.[8] Table II illustrates the results of AA and ICP analysis in order to investigate the effect of residual impurities after washing. It indicates that simple washing procedures did not eliminate Li^+, Na^+ and SO_4^{2-} completely as well as the study of PZN.[12] However, as the concentration of all impurities appeared to be independent of the amount of flux, it can be possible to disregard the effect of impurities owing to the variation of flux content on the microstructural and dielectric properties.

Table III represents the characteristics of PMN powders by MSS method in order to study the effects of particle size on sinterability and dielectric properties. With variations of the amount of flux $W = 0.2$ to $W = 2.0$, particle size was controlled as shown in Figure 1(A), (B) and (C). Hereafter, these powders will be designated as SP, MP and LP. respectively. The perovskite phase of 96–97% was obtained for all powders calcined at 800°C for 2 h. The average particle sizes of SP, MP and LP by laser particle analyzer were 1.51 μm. 1.98 μm and 2.78 μm, respectively. The green densities of SP, MP and LP specimens were 69.3, 67.5 and 64.2%, respectively.

Figure 2 shows the relative densities and linear shrinkages of the SP, MP and LP specimens as a function of sintering temperature. As sintering temperature increased. the relative densities of all specimens increased. The SP specimens were

FIGURE 3   SEM photographs of PMN specimens sintered at 1000°C for 4 h with various particle sizes. (A) SP. (B) MP and (C) LP.

more densified than the MP or LP specimens at ..... temperature. Linear shrinkage variations showed similar tendencies. In case of sintering at 1200°C for 4 h, the SP specimens had the relative density of 97%, whereas the LP specimens had that of about 93%. This indicates that the difference of particle size influences densification. Figure 3 shows the SEM photographs for the fracture surfaces of the
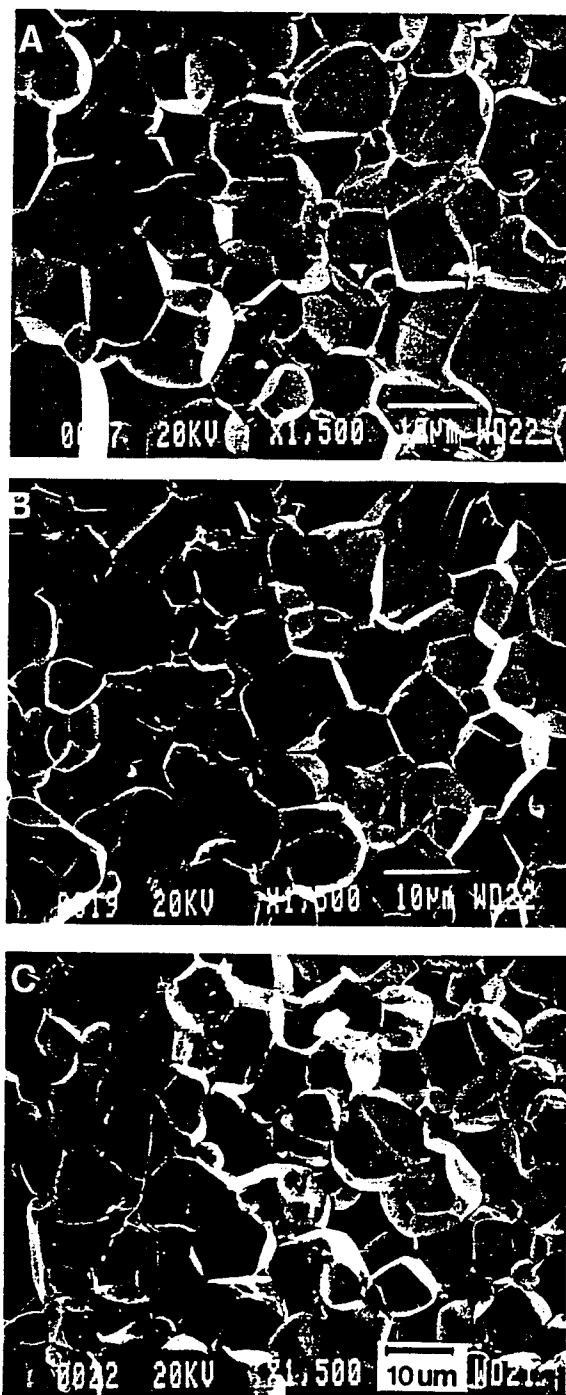
FIGURE 4 SEM photographs of PMN specimens sintered at 1200°C for 4 h with various particle sizes. (A) SP, (B) MP and (C) LP.

SP, MP and LP specimens sintered at 1000°C. Intergranular fracture surfaces were observed for all specimens probably due to a weak PbO grain boundary phase.[4] The LP specimens were barely densified compared to the SP specimens in agreement with the trend of the values of relative density (Figure 2). However, sintering was nearly completed at 1200°C for the SP, MP and LP specimens as shown in
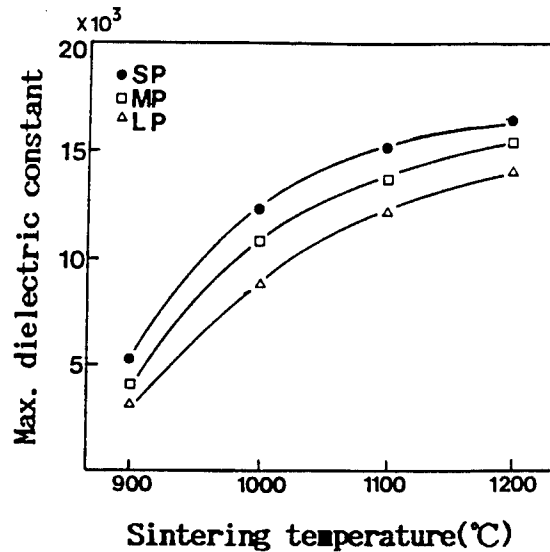
FIGURE 5   Maximum dielectric constant vs. sintering temperature for PMN specimens.
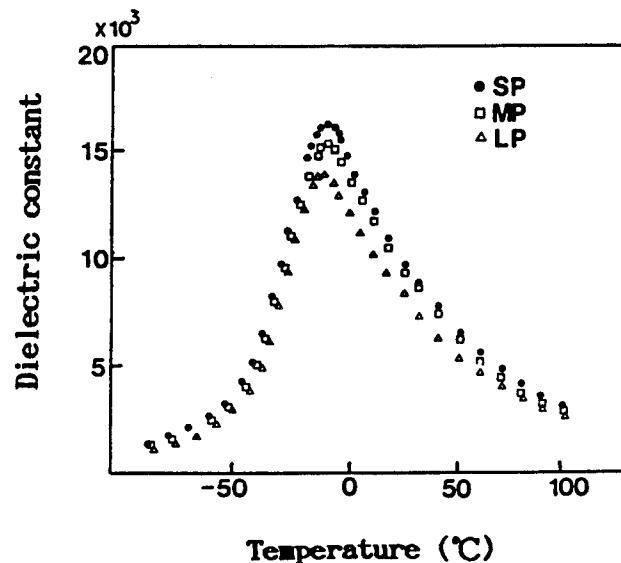

FIGURE 6   Dielectric constant vs. temperature for PMN specimens sintered at 1200°C for 4 h.

Figure 4. The average grain sizes (determined by a linear intercept method) of the SP, MP and LP specimens were 10.2 μm, 9.6 μm and 8.7 μm, respectively. At a lower temperature such as 1000°C (Figure 3) the grain sizes in the SP specimens were smaller than that in the LP specimens, while at 1200°C grain sizes in the SP specimens were larger. It is suggested that the smaller particle size the higher the densification rate is in PMN ceramics.

Figure 5 shows the maximum dielectric constants for the SP, MP and LP specimens sintered at various temperatures for 4 h. Also temperature dependences of dielectric constant and dielectric loss for the specimens sintered at 1200°C for 4 h were shown in Figures 6 and 7. All of these properties were measured at 100 Hz. Maximum dielectric constant of the SP specimens sintered at 1200°C was 16500,
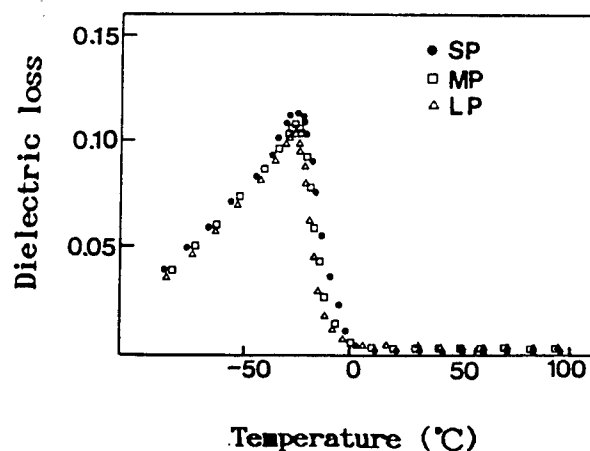
FIGURE 7 Dielectric loss vs. temperature for PMN specimens sintered at 1200°C for 4 h.

which is higher than those reported in the literatures for stoichiometric PMN ceramics.[13,14] It can be explained by the different processes used, i.e., molten salt synthesis and solid state (columbite) method. In Figure 5, with the increase of sintering temperature, the dielectric constant increased and the SP specimens had higher values than those of the MP, LP specimens at each sintering temperature. Generally, relating to microstructure, the dielectric constant has a dependency on grain size, density and tends to increase with grain size in the Pb based ferro-electrics.[5,13] This work also had the same tendency at 1200°C in that the SP specimens with large grains had a higher dielectric constant than the LP specimens with small grains. However, at a lower temperature, such as 1000°C, the dielectric constant of SP specimens were higher despite the smaller grain of the SP specimens. This suggests that the effects of density on dielectric properties were greater than those of the grain sizes at a low firing temperature. Apparent porosity of the SP specimens was about 7% at 1000°C whereas that of the LP specimens, was about 14%. The trend of dielectric loss agrees with that of dielectric constant. The values of maximum dielectric loss was relatively low in comparison to those by solid state synthesis and increased with the increasing of sintering temperature.

CONCLUSIONS

1. In PMN prepared by molten salt synthesis method, the percentages of per-ovskite phase was different with the variations of the amount of flux. When the ratio of salt weight to oxides weight is over 1.0, the perovskite phase of 97–98% was obtained with calcining above 750°C for 2 h.

2. The increase of the amount of sulfate flux resulted in the increase of particle size and correspondingly, the decrease of grain size at a saturated sintering temperature of 1200°C.

3. Relating to microstructure, dielectric properties depended on grain size, density and showed greater dependency on density rather than grain size at a relatively low firing temperature.

ACKNOWLEDGEMENT

REFERENCES

1. G. A. Smolenskii and A. I. Agranovskaya, *Sov. Phys.—Solid State*, **1**, 1429 (1959).
2. K. Uchino, *Am. Ceram. Soc. Bull.*, **65**, 647 (1986).
3. S. L. Swartz and T. R. Shrout, *Mater. Res. Bull.*, **17**, 1245 (1982).
4. T. R. Shrout and A. Halliyal, *Am. Ceram. Soc. Bull.*, **66**, 704 (1987).
5. D. H. Kang and K. H. Yoon, *Ferroelectrics*, **87**, 255 (1988).
6. M. Lejeune and J. P. Boilot, *Am. Ceram. Soc. Bull.*, **64**, 679 (1983).
7. T. Kimura, T. Takahashi and T. Yamaguchi, *J. Mater. Sci.*, **15**, 1491 (1980).
8. T. Kimura and T. Yamaguchi, pp. 169 in *Advances in Ceramics*, **21**, "Ceramic Powder Science," Edited by G. L. Messing *et al.*, *Am. Ceram. Soc.*, (1987).
9. K. H. Yoon, K. Y. Oh and S. O. Yoon, *Mater. Res. Bull.*, **21**, 1429 (1986).
10. K. H. Yoon, C. K. Kwak and D. H. Kang, *Ferroelectrics*, **116**, 231 (1991).
11. C. C. Chiu, C. C. Li and S. B. Desu, *J. Am. Ceram. Soc.*, **74**, 38 (1991).
12. F. Kojima and S. Nomura, *Jpn. J. Appl. Phys.*, **14**, 1255 (1975).
13. S. L. Swartz, T. R. Shrout, W. A. Schulze and L. E. Cross, *J. Am. Ceram. Soc.*, **67**, 311 (1984).
14. H-C. Wang and W. A. Schulze, *J. Am. Ceram. Soc.*, **73**, 825 (1990).

THIN FILM
FERROELECTRICS

APPENDIX 66

Electric field forced phase switching in La-modified lead zirconate titanate stannate thin films

K. G. Brooks, J. Chen, K. R. Udayakumar, and L. E. Cross

Materials Research Laboratory, The Pennsylvania State University, University Park, Pennsylvania 16802

Electric field forced antiferroelectric to ferroelectric phase switching has been demonstrated in thin films of $Pb_{0.97}La_{0.02}(Zr,Ti,Sn)O_3$ perovskites for the first time. Several compositions in the tetragonal antiferroelectric phase field of this system were prepared in thin film form by a sol-gel technique. Forward and reverse switching threshold fields of 27–103 kV/cm and 18–62 kV/cm, respectively, were determined from polarization-electric field hysteresis and incremental capacitance data. Switching times as fast as 300 ns were recorded for one of the antiferroelectric compositions. An electric field induced longitudinal strain of 0.16% was measured for a film of composition $(Pb_{0.97}La_{0.02})(Zr_{0.60}Ti_{0.10}Sn_{0.30})O_3$ using a laser ultradilatometer. These films are candidate materials for high charge storage integrated capacitors and microelectromechanical devices requiring large nonlinear strain response.

I. INTRODUCTION

Research in the area of ferroelectric thin films is being driven by the market potential of nonvolatile memory devices.[1-3] Due to the piezoelectric and pyroelectric properties of these thin films, applications are also emerging in the field of microelectromechanical systems (MEMS).[4-6] Ultrasonic micromotors utilizing lead zirconate titanate (PZT) thin films[7,8] and pyroelectric sensors using micromachined $PbTiO_3$ (PT)[9] have been fabricated. Thin film materials capable of large strains are being sought for a range of MEMS applications including micromotors, microvalves, and micropumps. Such devices will be utilized in compact medical, automotive, and space systems. Candidate materials include tetragonal antiferroelectric perovskites in the $Pb_{0.97}La_{0.02}(Zr,Ti,Sn)O_3$ (PLZTSn) and $Pb_{0.99}(Zr,Ti,Sn,)_{0.98}Nb_{0.02}O_3$ (PZTSnN) systems.

Tetragonal antiferroelectric (AFE) PLZTSn and PZTSnN ceramics of compositional proximity to the morphotropic phase boundary with the rhombohedral ferroelectric phase can be phase switched by application of an electric field from the AFE to FE states. The small free energy difference between the two phases make such switching possible.[10] The large volume difference between the AFE and FE phases dictates that large strains accompany such field induced phase switching.[11] Irreversible or field assisted switching (shape memory effect) occurs when the AFE composition is sufficiently close to the AFE-FE phase boundary that the electric field induced FE phase is metastable, with the free energy difference being less than the reverse switching threshold field energy.[12] The AFE phase can be recovered by thermal annealing or application of a reverse bias field.[13] Reversible or field forced switching occurs in compositions outside the region of metastability.

PLZTSn and PZTSnN ceramics have been investigated for several applications over the past 40 years including energy storage,[14] high strain actuators,[10,13,15,16] and shape memory devices.[17] Recent papers have focused on the thermodynamics of phase switching,[12,15] and transmission electron microscopy investigations of domain structures.[18,19]

Utilization of these ceramics has been limited due to high switching fields, being of the order of the electrical breakdown strength.[14] Degradation of the ceramics under an ac field excitation, with average life cycles of $\approx 10^7$, was reported by Pan *et al.*[16]

Synthesis of thin films in the PLZTSn system was motivated by the large strain values reported for the bulk ceramic materials. The largest longitudinal strain reported to date is 0.87% for a bulk ceramic of composition $(Pb_{0.97}La_{0.02})(Zr_{0.66}Ti_{0.11}Sn_{0.23})O_3$.[15] Thin films offer the possibility of integrated manufacturing of microsensors, microactuators, and high charge storage capacitors. In this article, we report the synthesis, characterization, polarization-electric field (P-E), and capacitance-voltage (C-V) response of sol-gel derived thin films in the PLZTSn perovskite system. The P-E and C-V data allow delineation of the forward AFE-FE, and reverse FE-AFE, electric field induced switching thresholds. Electric field induced strain and field induced AFE-FE switching speeds are also reported for select compositions.

II. THIN FILM SYNTHESIS AND COMPOSITION SELECTION

Several compositions in the $Pb_{0.97}La_{0.02}(Zr,Ti,Sn)O_3$ system were chosen based on an earlier paper which focused on bulk ceramic materials for large displacement transducers.[16] The pertinent area of the $PbZrO_3$-$PbTiO_3$-$PbO:SnO_2$ ternary phase diagram is shown in Fig. 1; compositions studied are indicated in the figure, and the corresponding chemical formula listed explicitly in Table I. This choice of compositions allowed comparison of phase switching parameters between bulk and thin films.

Thin films of the desired compositions were prepared by the sol-gel spin-on technique. Silicon wafers with titanium bonded platinum electrodes served as substrates. Precursors used for preparation of the sol-gel solutions included lead acetate trihydrate, tin[IV] acetate (anhydrous), lanthanum isopropoxide, zirconium *n*-propoxide, and tita-
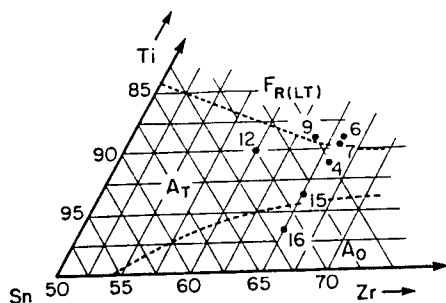
FIG. 1. The $PbTiO_3$-$PbZrO_3$-$PbO:SnO_2$ ternary phase diagram showing the orthorhombic antiferroelectric (A_O), tetragonal antiferroelectric (A_T), and low temperature rhombohedral ferroelectric ($F_{R(LT)}$) phase fields. Compositions studied are indicated (from Berlincourt, see Ref. 10).

nium isopropoxide. Details of the sol-gel precursor solution synthesis have been described previously,[20] and are summarized in the flow diagram, Fig. 2.

Films were annealed by rapid thermal processing, typically at 700 °C for 20 s, unless noted otherwise. For films annealed under these conditions, only perovskite reflections were observed by grazing angle x-ray diffraction. Films annealed at 600 °C were also phase pure but required extended annealing times to achieve equivalent properties. Films annealed above 750 °C exhibited hysteresis loop degradation which can be attributed to loss of Pb from the film. Film thicknesses were in the range of 0.3–0.4 μm.

Microstructures of the films were characterized by scanning electron microscopy (SEM). The films were found to be very uniform, with microstructures being dependent upon composition. Grain sizes of approximately 0.5 μm were observed for films of composition 4 (Fig. 3). Larger grain sizes, of the order of 1.0 μm were observed for films of compositions 6, 7, and 9.
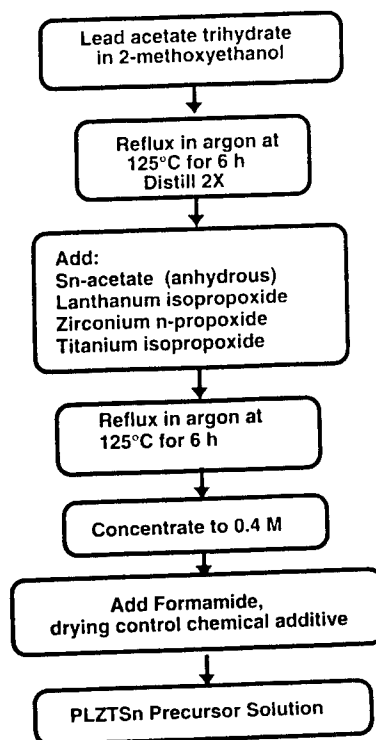

FIG. 2. Flow diagram of the sol-gel synthesis of PLZTSn thin films.

III. FIELD INDUCED AFE-FE PHASE SWITCHING

A. Measurements

Polarization-electric field hysteresis was measured using a modified Sawyer–Tower circuit. Electrical contact with the film surface was achieved with a Hg-probe test fixture. The effective electrode area was 4.3×10^{-3} cm^2. Samples were driven with a 10–15 V, 60 Hz signal (10 V ≈ 300 kV/cm for film thickness studied). Scanning elec-

TABLE I. Compositions studied and summary of thin film and bulk ceramic electric field induced switching data.

| No. | Composition | Thin film | | | | Bulk ceramic[a] | | |
		E_{APP} (kV/cm)	$E_{AFE\text{-}FE}$ (kV/cm)	$E_{FE\text{-}AFE}$ (kV/cm)	P_{max} (μC/cm^2)	E_{APP} (kV/cm)	$E_{AFE\text{-}FE}$ (kV/cm)	P_{max} (μC/cm^2)
4	$(Pb_{0.97}La_{0.02})(Zr_{0.66}Ti_{0.09}Sn_{0.25})O_3$	300	103	53	32	75	50	43
6	$(Pb_{0.97}La_{0.02})(Zr_{0.66}Ti_{0.11}Sn_{0.23})O_3$	300	85[b]	23[c]	33	46	21	40
7	$(Pb_{0.97}La_{0.02})(Zr_{0.66}Ti_{0.105}Sn_{0.235})O_3$	300	81[b]	47[c]	26	58	22	36
9	$(Pb_{0.97}La_{0.02})(Zr_{0.64}Ti_{0.11}Sn_{0.25})O_3$	300	27[b]	...[d]	11	60	24	36
12	$(Pb_{0.97}La_{0.02})(Zr_{0.60}Ti_{0.10}Sn_{0.30})O_3$	200	44	18	26	59	49	32
		300	40	20	28			
15	$(Pb_{0.97}La_{0.02})(Zr_{0.65}Ti_{0.07}Sn_{0.28})O_3$	200	89	62	21			
		300	87	59	24			
		400	87	54	26			
16	$(Pb_{0.97}La_{0.02})(Zr_{0.65}Ti_{0.038}Sn_{0.312})O_3$	800	233	134	31			

[a]Data from Ref.
[b]Determined from C-V data, initial cycle.
[c]Determined from C-V data.
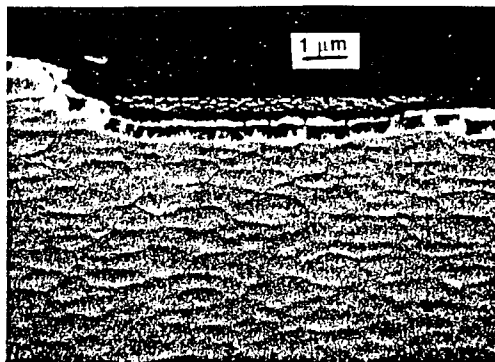[d]Metastable FE phase formation.

Brooks et al.

FIG. 3. Typical SEM microstructure of PLZTSn thin films. Shown above is the photomicrograph of a film of composition 4 annealed at 700 °C for 20 s.
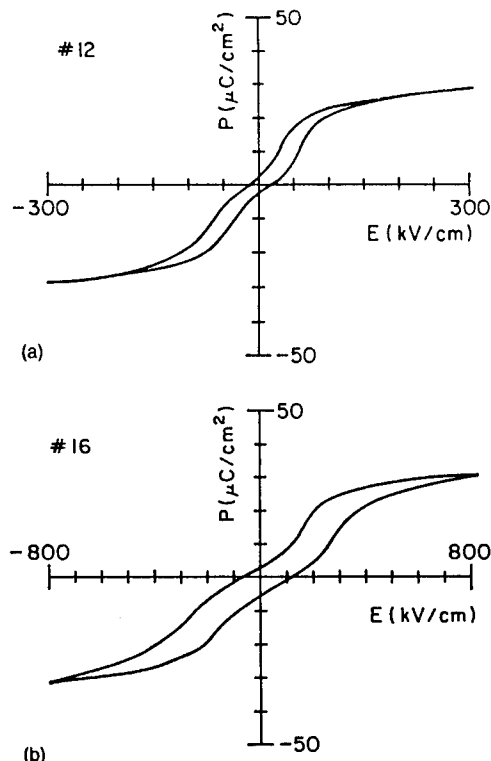

FIG. 4. Polarization-electric field hysteresis loop for thin films of composition (a) 12, (b) 16. Forward switching (AFE-FE) and backward switching (FE-AFE) fields were determined by taking the intersections of two lines representing the steepest and flattest sections of the hysteresis loops.

tron microscopy was used to determine film thickness. All measurements described were carried out at 25 °C.

Capacitance data as a function of slowly varying bias field was collected with a computer interfaced impedance analyzer (HP 4192A). Sputtered Au electrodes approximately 1000 Å thick and 2.8×10^{-3} cm^2 in area were used. Capacitance was determined using a 10 mV, 10 kHz test signal. Under these conditions, the dielectric loss was always less than 0.08. The dc bias was slowly stepped through 0.2 V increments in a cyclic manner between -10 and $+10$ V.

Electric field induced strain was measured using a laser interferometer with a film surface displacement resolution of 10^{-2} Å.[21] Phase switching was induced with a 500 Hz electric field of varying magnitude and under different bias conditions.

The switching current was measured as a function of time by the square pulse technique. The signal pick-up resistor was 5 Ω to reduce the RC constant. A parallel resistor of 50 Ω was used to reduce the signal reflection during the measurements.

B. Results and discussion

Dynamic polarization-electric field (P-E) hysteresis curves were recorded for all the compositions, and the switching field data tabulated in Table I. The P-E traces for compositions 12 and 16, exemplifying phase switching, are shown in Fig. 4. Forward switching (AFE-FE) and backward switching (FE-AFE) fields were determined by taking the intersections of two lines representing the steepest and flattest sections of the hysteresis loops. For compositions in close proximity to the AFE-FE phase boundary (6,7,9), switching threshold fields could not be determined from P-E hysteresis data. The remanence observed for these boundary compositions indicates that some fraction of the film is retained in the FE state at zero field. The switching data obtained is summarized in Table I. For films of composition 15, switching parameters were investigated as a function of applied field. The forward switch-

ing threshold was constant as a function of increasing field from 200 to 400 kV/cm. However, the reverse switching threshold was found to decrease and the maximum polarization increase as applied field increased. The ability to switch films of composition 16, which lies in the orthorhombic AFE phase field, was an interesting result. The forward switching threshold of 233 kV/cm under an applied field of 800 kV/cm is indicative of the large free energy difference between this and the FE phase.

Phase switching thresholds can also be derived from capacitance as a function of slowly varying bias field. The relationship between the P-E hysteresis and C-V data is shown schematically in Fig. 5. Phase switching thresholds can be estimated from the C-V curves by defining switching as the bias at maximum capacitance. This definition, however, yields forward and reverse thresholds slightly larger than those obtained from analogous P-E hysteresis data. The incremental capacitance data for compositions 12 and 16 is shown in Fig. 6 (compare with the corresponding P-E curves of Fig. 4). This data made it possible to measure the threshold fields when the P-E curves were ambiguous, particularly in the case of boundary compositions (6,7,9). In the case of composition 9, only forward switching could be positively determined. The P-E and C-V data indicate that a metastable FE phase is induced upon application of field to the virgin sample, and is re-

J. Appl. Phys., Vol. 75, No. 3, 1 February 1994

Brooks et al.   1701

[13] B. Jaffe, Proc. Inst. Radio Engineers **49**, 1264 (1961).

[14] W. Y. Pan, C. Q. Dam, Q. M. Zhang, and L. E. Cross, J. Appl. Phys. **66**, 6014 (1989).

[15] Y. Sugawara and K. Uchino, in *Proceedings of the 7th IEEE International Symposium on Applications of Ferroelectrics*, edited by S. B. Krupanidhi and S. K. Kurtz (IEEE, New York, 1991), pp. 328–329.

[16] W. Y. Pan, Q. M. Zhang, A. S. Bhalla, and L. E. Cross, J. Am. Ceram. Soc. **72**, 571 (1989).

[17] A. Furata, K. Oh, and K. Uchino, in *Proceedings of the 7th IEEE International Symposium on Applications of Ferroelectrics*, edited by S.

B. Krupanidhi and S. K. Kurtz (IEEE, New York, 1991), pp. 528–529.

[18] C. Zhiming, L. Jingyu, and W. Yongling, Ferroelectrics **101**, 225 (1990).

[19] M. De Graef, J. S. Speck, D. R. Clarke, and D. Dimos, Mater. Res. Soc. Symp. Proc. **243**, 1 (1992).

[20] K. G. Brooks, J. Chen, K. R. Udayakumar, and L. Eric Cross, Mater. Res. Soc. Symp. Proc. **243**, 443 (1992).

[21] Q. M. Zhang, W. Y. Pan, and L. E. Cross, J. Appl. Phys. **63**, 2492 (1988).

[22] W. Y. Pan, W. Y. Gu, and L. E. Cross, Ferroelectrics **99**, 185 (1989).

Brooks *et al.*

. . . I Phys. Vol. 75, No. 3, 1 February 1994

APPENDIX 67

Surface morphology of r.f. sputtered bismuth titanate thin films

P. K. GHOSH
Department of Electrical and Computer Engineering, Syracuse University, Syracuse, NY 13244, USA

A. S. BHALLA, L. E. CROSS
Materials Research Larboratory, The Pennsylvania State University, University Park, PA 16802, USA

Bismuth titanate ($Bi_4Ti_3O_{12}$) thin films were prepared by the r.f. sputtering technique. A bismuth-rich target was used to compensate for the loss of bismuth during deposition. Studies on many films, deposited under various conditions, showed that existence of non-uniform erosion leads to many surface morphological features. This varying surface structure is a consequence of the resputtering process. Because the microstructure has a significant effect on the films electrical/optical response, a knowledge of its dependency on process parameters is an important step towards device development.

1. Introduction

Ferroelectric bismuth titanate ($Bi_4Ti_3O_{12}$) with a mica-like morphology belongs to the large family of layer structure oxide compounds. With its high electrical breakdown property, $Bi_4Ti_3O_{12}$ is a good candidate for thin-film capacitors. Device applications using its switching and optical properties were reported by Cummins [1, 2]. $Bi_4Ti_3O_{12}$ also has potential as a non-volatile high-density memory. For all of these applications it is important to have a knowledge of the microstructural behaviour of bismuth titanate thin film. This has been attempted in the present study by investigating the proclivity of the material for resputtering.

Epitaxial $Bi_4Ti_3O_{12}$ thin-film preparation on MgO and epitaxial platinum was reported by Takei et al. [3]. Films were prepared using both reactive triode and r.f. sputtering with various target compositions. Preparation of bismuth titanate thin films, on various substrates, with a dielectric constant comparable to its single crystal value, was also reported by Ghosh et al. [4]. The r.f. sputtering technique with a hot-pressed ceramic target of composition $0.8 Bi_4Ti_3O_{12} + 0.2 Bi_{12}TiO_{20}$ was used for deposition.

During the process of film preparation, several morphological variations in the films were observed. The observed profound effects of preparation parameters on the film microstructure are reported. The effects of microstructure on the dielectric properties of the film were significant and have been reported elsewhere [4]. Bismuth titanate was deposited under various deposition conditions and resputtering effects were investigated. The results obtained were compared with the prediction of the model developed by Cuomo et al. [5, 6].

2. Experimental procedure

Bismuth titanate thin films were deposited by r.f. sputtering a 2 in. diameter target in an argon:oxygen mixture atmosphere. $Bi_4Ti_3O_{12}$ films were prepared using a wide range of sputtering parameters. Deposition time, r.f. power level, partial gas pressure, and substrate temperature were all varied. After mounting clean substrates, the system was pumped down to an initial background pressure of 1.2×10^{-6} torr. In a hot deposition scheme (i.e. increased substrate temperature) this process was followed by heating the substrates to the desired temperature (maximum temperature 552 °C). The system chamber pressure was also stablized at 20 mtorr by the introduction of sputtering gas into the system. Three methods of film characterization were used. A profilometer (Talysurf 10) was used for measuring variations in film thickness as a function of radial distance from the centre of the target, by measuring the step height from the film to an area that had been covered by a thin glass wafer during deposition. In the second method, the development of surface morphology due to resputtering was studied using a scanning electron microscope (SEM). The third method of characterization was a visual observation of the sputtered films. As reported [7], any texturing of the film surface due to resputtering could often be observed visually.

3. Results and discussion

Substrates directly under the target, especially in a ring-shaped area under the edge of the target, are generally affected by resputtering. The development of surface morphology features and variation in film thickness was observed in substrates placed in this area.

The intensity and type of effect, resulting from resputtering, were found to vary as functions of the sputtering parameters as well as the location of the substrate. Fig. 1 shows the electron micrographs in which the range of micro-effects (i.e. the development of surface morphology features) observed in bismuth titanate films can be seen. All three films were prepared at 100 W with 20 mtorr gas pressure (50:50, O_2:Ar) for 5 h. As indicated in Fig. 1, the only variable was the relative position of the substrates (preparation geometry) with respect to the centre-line of the target. The change of substrate temperature also induced a wide range of micro-effects as shown in Fig. 2. These films were deposited under similar deposition conditions (mentioned above) but this time the variable was substrate temperature.

In addition to the substrate position and substrate temperature, a change in the microstructure resulting from a change in r.f. power as depicted in Fig. 3, and from a change in partial gas pressure (Fig. 4) was also observed. The change in partial gas pressure also induces nonstoichiometry and is evident in the black

Figure 1 Effect of preparation geometry on the microstructure of $Bi_4Ti_3O_{12}$ thin films.

colour of the film, compared to light yellow for stoichiometric bismuth titanate.

A significant variation in film thickness (macro-effect) was observed, as shown in Fig. 5, caused both by the change of substrate temperature and the relative position of the substrates.

The judgment on the presence of resputtering, its intensity and type of effects was made based on the three methods of observation: scanning electron micrographs, thickness profiles, and visual observation. On the micrographs evidence of resputtering would be seen through the formation of surface morphology features such as etch pits. For the thickness profile graphs, drops in thickness under the edge of the target indicated resputtering. Visual observation of the substrate indicate a change of colour in the resputtered area. These areas where resputtering had occurred also agree with the results of profilometer and/or scanning electron micrographs.

Resputtering of a growing film can occur due to a number of bombardment processes, e.g. bombardment of the material by energetic positive ions extracted from the discharge by a negative bias at the substrate [8, 9], high-energy elastically back-scattered particles [10], and bombardment by negative ions originating near the target surface, generally at a high negative potential, and accelerated across the dark space [8]. In particular, under certain conditions, the growing film can be resputtered at the same rate by which it grows and can even lead to resputtering of the substrate [11]. Among the various processes the bombardment by negative ions appears to be the main cause of resputtering. Cuomo *et al.* [5, 6], developed a model which states that ionization potential, I_A, and electron affinity, EA_B, of target elements, A and B, can be used in the form $I_A - EA_B$ as a useful measure to predict negative ion production. According to their results, at about 3.4 eV or less, the probability of negative-ion formation is higher, resulting in a noticeable resputtering effect.

Negative-ion resputtering does not lead to uniform film erosion but rather results in isolated etch pits on the growing films. If the etch pits remain isolated they may not be seen optically and can easily go undetected unless explicitly sought. However, under high doses of ion bombardment the etch pits overlap and can lead to a variety of morphological structures such as ripples, dimples, needles, etc., which usually scatter light and are readily noticed [12, 13]. These etch pits have been observed in WO_3 films [14], although $I_A - EA_B$ for WO_3 is 6.5 eV, which is considerably higher than the threshold value of 3.4 eV proposed by Cuomo *et al.* [5, 6]. The reason for this, as explained by Giri and Messier [14], is that the resputtering rate is not large enough to prevent the film growth, but it is sufficient to cause localized structural defects, such as isolated etch pits. The value of $I_A - EA_B$ for bismuth titanate is 5.35 eV, lower than the $I_A - EA_B$ value of WO_3. Because resputtering has been observed in WO_3, it is probable that resputtering will occur during the deposition of $Bi_4Ti_3O_{12}$. Kester [7], also reported the probability of resputtering in bismuth titanate. Our current observations on various films, prepared
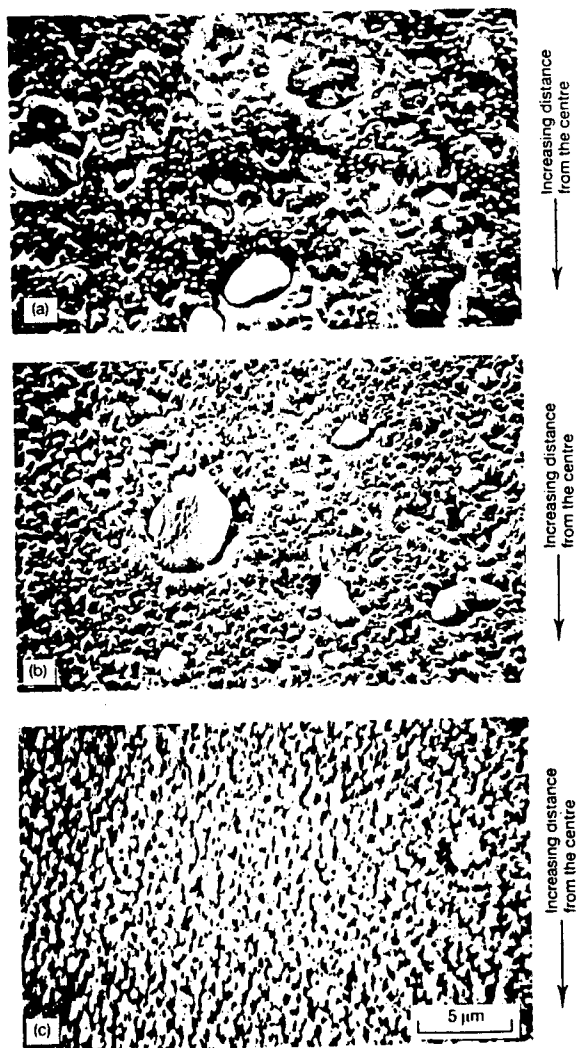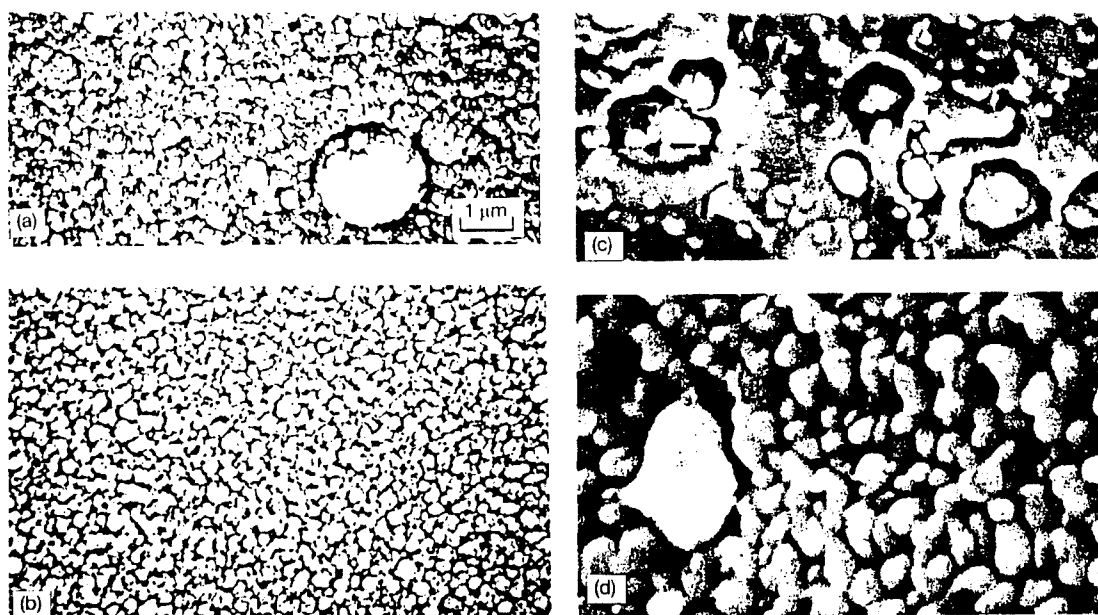
Figure 2 The microstructure of $Bi_4Ti_3O_{12}$ thin films deposited at different substrate temperature. (a) 325 °C, (b) 356 °C, (c) 414 °C, (d) 461 °C.

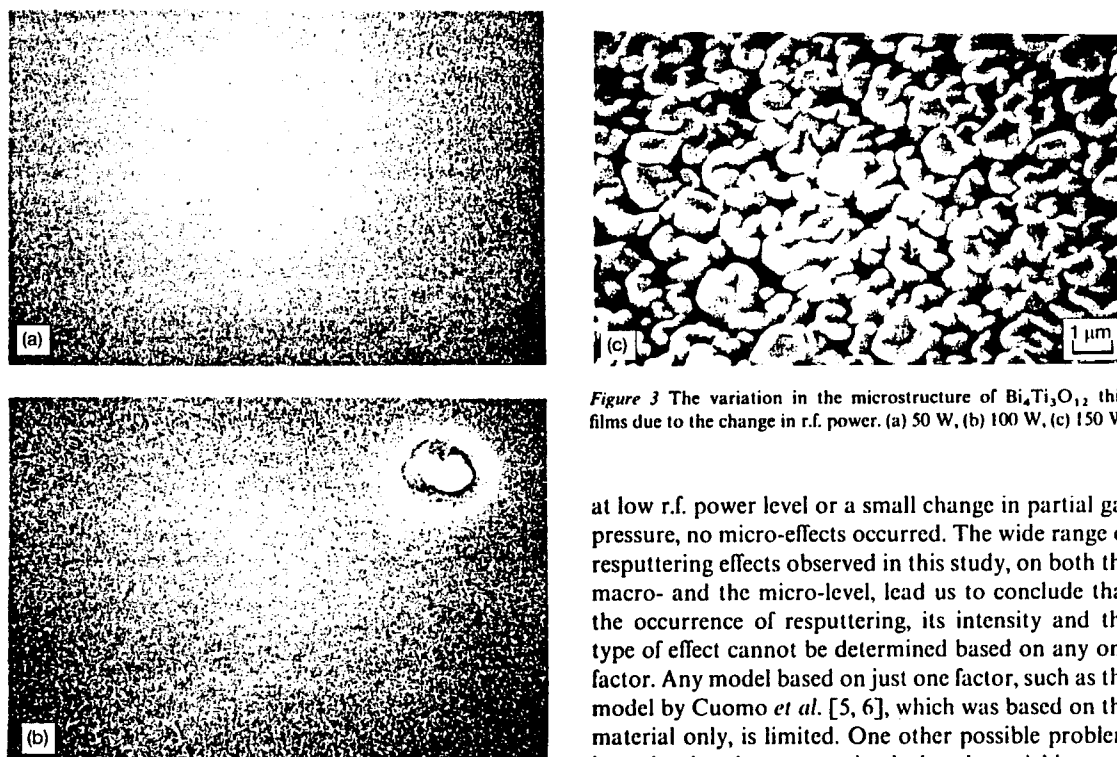*Figure 3* The variation in the microstructure of $Bi_4Ti_3O_{12}$ thin films due to the change in r.f. power. (a) 50 W, (b) 100 W, (c) 150 W.

at low r.f. power level or a small change in partial gas pressure, no micro-effects occurred. The wide range of resputtering effects observed in this study, on both the macro- and the micro-level, lead us to conclude that the occurrence of resputtering, its intensity and the type of effect cannot be determined based on any one factor. Any model based on just one factor, such as the model by Cuomo *et al.* [5, 6], which was based on the material only, is limited. One other possible problem in evaluating the resputtering is that the stoichiometry of the material should be taken into account.

under different conditions, confirm resputtering in $Bi_4Ti_3O_{12}$.

Our study indicates a significant effect of deposition parameters on resputtering, leading to various morphological surface features. In some cases, for example

4. Conclusion

Bismuth titanate thin film prepared by the r.f. sputtering method exhibits various surface morphological features, resulting from non-uniform erosion of
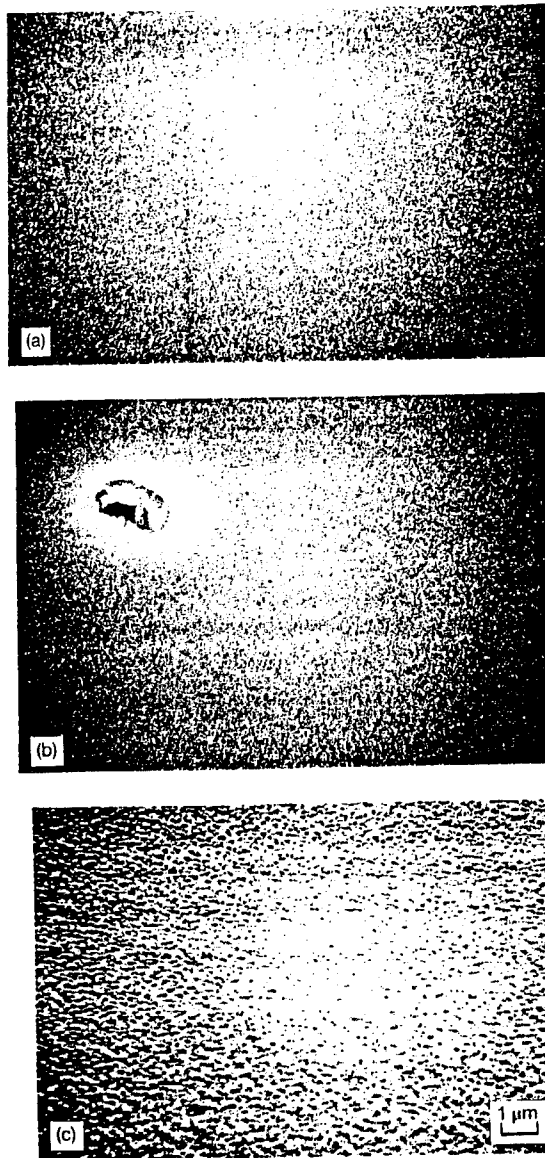
4661

Figure 4 Effect of percentage change in argon pressure on the microstructure of Bi₄Ti₃O₁₂ thin films. (a) 10 mtorr, (b) 15 mtorr, (c) 20 mtorr.

the film due to the resputtering process. The effect of resputtering depends significantly on the deposition parameters. Results also indicate that many factors influence resputtering and that a model based on one factor, such as $I_A - EA_B$ value, cannot always predict the occurrence of resputtering.
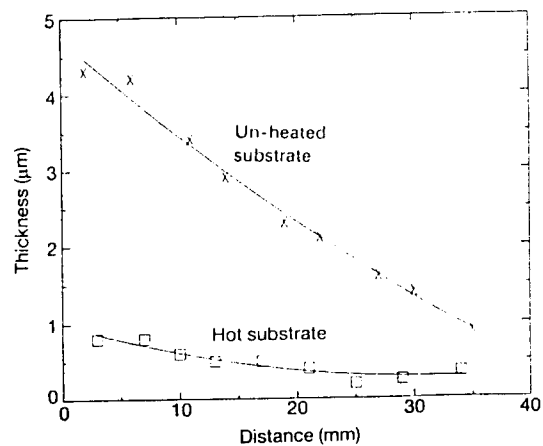

Figure 5 Thickness profile of Bi₄Ti₃O₁₂ thin films deposited on (X) unheated and (⬜) hot substrates. The thicker film is at the centre and the thinner film is near the edge.

Acknowledgement

References

1. S. E. CUMMINS. *Proc. IEEE* 55 (1967) 1536.
2. *Idem, ibid.* 55 (1967) 1537.
3. W. J. TAKEI, N. P. FORMINGONI and M. H. FRANCOMBE. *J. Vac. Sci. Technol.* 7 (1970) 442.
4. P. K. GHOSH, A. S. BHALLA and L. E. CROSS, in "1986 IEEE", ISAF, Lehigh University, PA, 8-11 June 1986.
5. J. J. CUOMO, R. J. GAMBINO, J. M. E. HARPER and J. D. KUPTSIS, *IBM J. Res. Dev.* 21 (1977) 580.
6. J. J. CUOMO, R. J. GAMBINO, J. M. E. HARPER, J. D. KUPTSIS and J. C. WEBBER. *J. Vac. Sci. Technol.* 15 (1978) 281.
7. D. J. KESTER. MS thesis, The Pennsylvania State University (1984).
8. L. I. MAISSEL, C.L. STANDLEY and L. V. GREGOR. *IBM J. Res. Dev.* 16 (1972) 67.
9. R. E. JONES, C. L. STANDLEY and L. I. MAISSEL. *J. Appl. Phys.* 38 (1970) 178.
10. D. W. HOFFMAN and J. A. THORTON. *J. Vac. Sci. Technol.* 16 (1979) 134.
11. L. R. GILBERT, R. MESSIER and S. V. KRISHNASWAMY, *ibid.* 17 (1980) 389.
12. D. J. KESTER and R. MESSIER, *ibid.* A4 (1986) 496.
13. R. MESSIER and D. J. KESTER, *Appl. Surf. Aci.* 22/23 (1985) 111.
14. A. P. GIRI and R. MESSIER, *Mater. Res. Symp. Proc.* 24 (1984) 221.

APPENDIX 68

Deposition Profile of RF-Magnetron-Sputtered BaTiO3 Thin Films

Nam-Yang LEE. Tomoyuki SEKINE. Yukio ITO[1] and Kenji UCHINO[2]

Department of Physics. Sophia University. 7-1 Kioi-cho. Chiyoda-ku. Tokyo 102
[1]*Central Research Laboratory. Hitachi. Ltd.. Kokubunji. Tokyo 185*
[2]*Materials Research Laboratory. Pennsylvania State University. University Park. PA 16802. USA*

BaTiO3 thin films were fabricated using an rf-magnetron sputtering technique and an oxide target. In spite of depositing on an amorphous fused quartz substrate. the preferentially oriented thin films were obtained without any post-annealing process. The preferred orientation of the thin films changed with sputtering gas pressure, gas composition and substrate temperature. At a lower gas pressure. the thin films crystallized well and preferentially oriented to the [100] direction. With increasing gas pressure. the preferred orientation changed to (110). On the other hand. at a lower substrate temperature or higher argon partial pressure. the preferred orientation changed to (111). The variation of the preferred orientation. lattice constant. and crystallite size with sputtering conditions was explained by assuming a *thermal-vibration* model.

KEYWORDS: rf-magnetron sputtering, BaTiO3 film, thermalization, interionic distance, thermal vibration

1. Introduction

BaTiO3 thin films have been receiving the greatest attention during the past two decades because of their high dielectric constant. The applicability of epitaxially grown BaTiO3 thin films in the construction of nonvolatile random-access-memory capacitors, electrooptic devices, and pyroelectric detectors is of particular interest.[1-4] The requirements of the films for these applications are: (i) high crystallinity and preferential orientation, (ii) stoichiometric composition, (iii) smooth and perfect surface, especially for the optical devices, and (iv) *in situ* fabrication of the films at relatively low substrate temperature.

Various methods have been proposed and investigated to improve film properties.[5-10] Among them. rf-magnetron sputtering has been known as one of the most promising deposition techniques in view of reproducibility, uniformity and simplicity.

Although several studies have been reported on physical and electrical properties of rf-sputtered BaTiO3 thin films. crystal substrates were used to obtain highly oriented or epitaxially grown films. In these cases, it is difficult to clearly understand the intrinsic deposition profile of BaTiO3 thin films because the orientation of the films depends strongly on the crystal orientation of the substrate.

In this paper, we carried out rf-sputter deposition onto amorphous fused quartz substrates to investigate the intrinsic deposition behavior of BaTiO3 thin films. In spite of the use of an amorphous substrate, the crystal orientation of BaTiO3 thin films could be controlled by various sputtering conditions. It was also confirmed that the crystallized films can be obtained at a substrate temperature as low as 300°C. From the experimental results on preferred orientation, lattice constant and crystallite size. a thermal-vibration model is suggested in this paper as one of possible intrinsic deposition mechanisms for the rf-sputtered BaTiO3 thin films.

2. Experimental

BaTiO3 thin films were prepared with an rf-magne-

Table I. Sputtering conditions of BaTiO3 thin films.

Target	BaTiO3 ceramic disc
Substrate	Fused quartz
Substrate temperature	100–700°C
Gas pressure	0.1–4.0 Pa
Ar/(Ar+O2)	10–90%
Rf power	200 W
Target-Substrate (T-S) distance	50 mm

tron sputtering system (SPF-430HS, Anelva). The sputtering target was a BaTiO3 ceramic disk with 100 mm diameter and 5 mm thickness, having a stoichiometric composition with purity of 99.9%. An amorphous fused quartz plate with 10 mm × 10 mm × 1 mm dimensions was used as a substrate, after it was cleaned with trichloroethane and acetone. The sputtering conditions are summarized in Table I. The deposition rate of sputtered films was varied in a wide range from 15 to 100 Å/min with the sputtering conditions.

An X-ray diffractometer (Jeol. JDX-11PA) was employed to examine the crystallographic properties. The average crystallite size of as-grown films was estimated from the full width at half-maximum (FWHM) of the peaks using Scherrer's formula.[11] Scanning electron microscopy (SEM) was used to observe surface morphology and film thickness. The deposition rate was calculated from the film thickness and sputtering time.

3. Results

3.1 Orientation of the thin films

3.1.1 Effect of gas pressure

Figure 1 shows X-ray diffraction patterns of the as-grown thin films deposited under various sputtering gas pressures. At gas pressures below 0.3 Pa. only the (100)-equivalent peaks ((100). (001). (200). (002), etc.) are observed: this indicates that the film preferentially grows with the [100] direction perpendicular to the substrate. With increasing gas pressure, the (110) and (111) peaks appear gradually and the film exhibits random orientation. At gas pressures above 4.0 Pa. the orientation of the film is changed to the [110] direction.
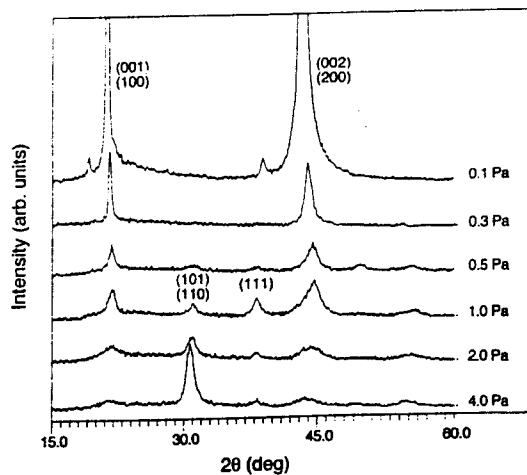
Fig. 1.   X-ray diffraction patterns of as-grown films sputtered under various gas pressures. (rf power: 200 W. Ar/(Ar+O₂): 70/100, substrate temperature: 700°C. T-S distance: 50 mm).

Fig. 3.   X-ray diffraction patterns of as-grown films sputtered at various substrate temperatures. (rf power: 200 W. Ar/(Ar+O₂): 70/100. sputtering gas pressure: 0.1 Pa. T-S distance: 50 mm).

3.1.2   Effect of gas composition

Figure 2 shows the changes of X-ray diffraction patterns for various sputtering gas compositions of Ar/(Ar+O₂) while keeping the total gas pressure at 1.0 Pa. Broad and low-intensity peaks appear at the lower argon content of 10%. At the argon content of 30%, preferentially oriented (100)-equivalent peaks with high intensity appear. However, this orientation of films is lost at higher argon contents (>50%), and the (111) orientation becomes dominant above 90%. The gas composition as well as the gas pressure play an important role in the preferred orientation of thin films. The deposition rate was increased linearly from 15 to 100 Å/min with increasing argon content.

3.1.3   Effect of substrate temperature

Figure 3 shows the dependence of X-ray diffraction

patterns of the films on the substrate temperature. The gas pressure and the gas composition were fixed at 0.1 Pa and at the argon content of 70%, respectively. At a substrate temperature of 700°C, only two peaks due to the (100) and (200) reflections appear. Upon reducing the temperature. the films show random orientation, and at a temperature of 300°C, the preferred orientation along (111) appears. The substrate temperature below 100°C cannot provide a crystallized phase. It is noteworthy from a practical point of view that crystallized and preferentially oriented films can be fabricated at a substrate temperature as low as 300°C when the sputtering conditions are properly controlled.

3.2   Lattice constants

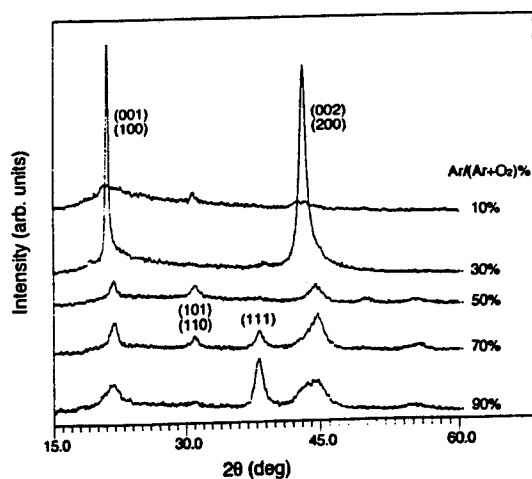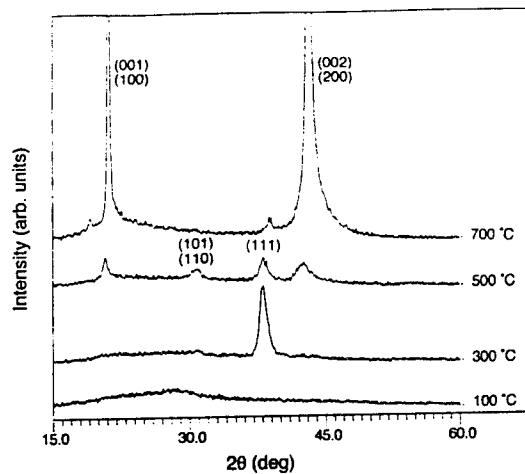Figure 4 shows the variation of the lattice constant

Fig. 2.   X-ray diffraction patterns of as-grown films sputtered at various gas compositions. (rf power: 200 W. substrate temperature: 700°C. sputtering gas pressure: 1.0 Pa. T-S distance: 50 mm).
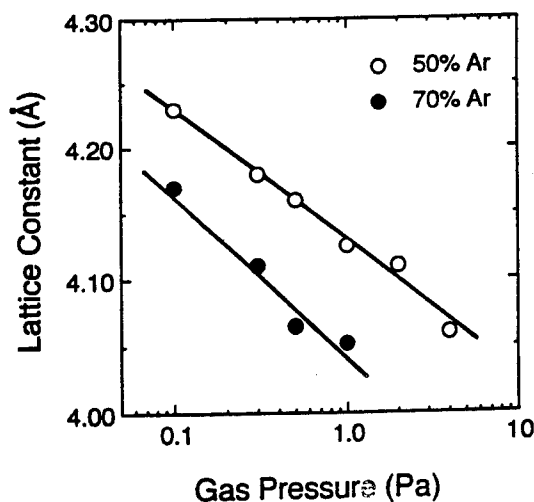

Fig. 4.   Gas pressure dependence of lattice constant. (rf power: 200 W. Ar/(Ar+O₂): 70/100 and 50/100. substrate temperature: 700°C. T-S distance: 50 mm).

with sputtering gas pressure. As the gas pressure increases, the lattice constant of as-grown films decreases linearly. Over the entire range of gas pressures applied in this study, the lattice constant was relatively larger than that of $BaTiO_3$ single crystal ($a = 3.989$ Å, $c = 4.029$ Å). The lattice constant is also affected by the gas composition. With increasing argon content, the lattice constant decreases. Nagatomo and Omoto[12] and Schäfer[13] have reported that the lattice constant of as-grown films is large compared with that of single crystal. They attributed the result to the stress caused by the difference in the thermal expansion coefficient between the film and the substrate. However, in our case, the difference of thermal expansion ($BaTiO_3$: 14 ppm/°C, fused quartz: 0.56 ppm/°C) does not exceed 1% for the temperature difference between room temperature and the deposition temperature of 700°C. Therefore, the deviation of lattice constant (maximum 5%) cannot be explained by the thermal expansion coefficient. The reason will be discussed in the next section.

Figure 5 shows the effect of annealing temperature on the lattice constant. The lattice constant decreases markedly and approaches the value of single crystal above 1200°C. Although the peak intensity was increased by the annealing process, the preferred orientation did not change. On the other hand, above an annealing temperature of 700°C, microcracks were observed in most of the samples. These cracks are probably attributed to the volume contraction due to the crystallization and close packing of atoms. Figure 6 shows the surface morphologies of the films after annealing at 1100°C for 1 h. Although microcracks are observed in both films, the film deposited at 0.1 Pa shows finer cracks in comparison with the film at 1.0 Pa. This means that the larger the lattice constant, the more contraction occurs during the annealing process.

3.3 Crystallite size

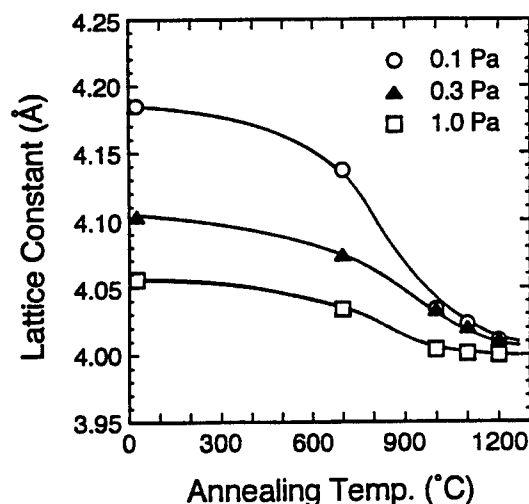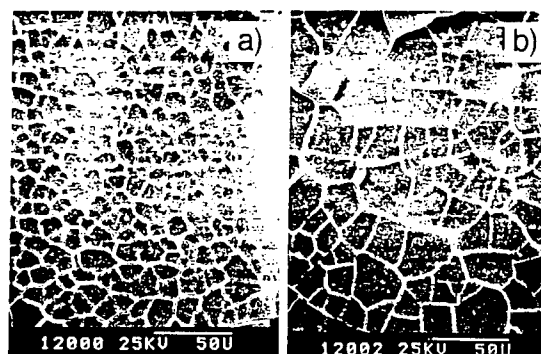Figure 7 plots the relationship between the crystal-

Fig. 6. Surface morphology of films with the sputtering gas pressure of 0.1 Pa (a) and of 1.0 Pa (b) after post-annealing process at 1100°C for 1 h.
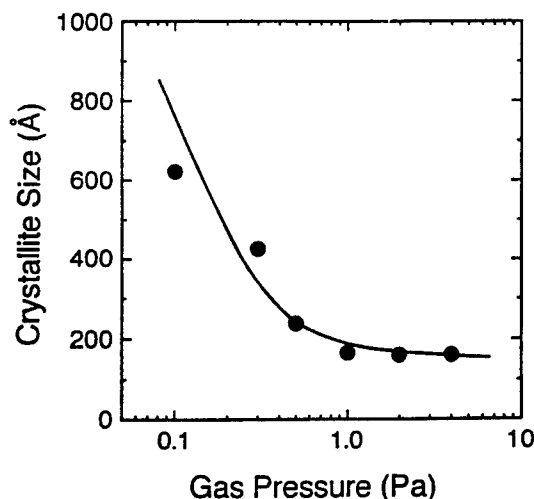

Fig. 7. Relationship between the crystallite size of as-grown films and the gas pressure.

lite size of as-grown films and the gas pressure. Because the crystallite size was too small to be observed by SEM, it was estimated from the full width at half-maximum (FWHM) of the X-ray peaks using Scherrer's formula.[11] The crystallite size of the films sputtered at 0.1 Pa is about 620 Å and it decreases with increasing gas pressure. However, it approaches the constant value of 160 Å above the gas pressure of 1.0 Pa. The crystallite size also decreased as the argon content increased.

4. Discussion

We find that the sputtering conditions affect not only the preferred orientation but also the lattice constant and crystallite size. These results can be explained partially by the existing mechanisms. For example, the variation of the film orientation in a gas pressure range of 0.1–2.0 Pa can be understood by the well-known particle bombardment mechanism.[14-16] That is, at a lower

Fig. 5. Lattice constant as a function of annealing temperature.

gas pressure. the film is bombarded by high-energy particles normal to its surface, resulting in the film with a certain primary orientation. At a higher gas pressure, particle scattering causes the film bombardment by low-energy particles at oblique angles, resulting in a randomly oriented film. However. this mechanism is insufficient to explain the reappearance of the (110) peak at a gas pressure higher than 4.0 Pa. Moreover, the variation of the lattice constant and crystallite size with sputtering conditions has not been discussed systematically. We will discuss the relationship between the sputtering conditions and the deposition profile in detail in this section.

4.1 Energy of sputtered particles

The sputtered particles suffer collisions during their transport through the plasma to the substrate and lose their initial energy continuously.[17,18] The initial energy of sputtered particles is known to be on the order of eV, corresponding to the temperature on the order of 10^4–10^5 K (1 eV $= 11600$ K).[17] After a finite number of collisions, the energy of sputtered particles is reduced to the thermal energy $(k_B T)$, and the sputtered particles are said to be "thermalized", where k_B is the Boltzmann constant.

The thermalization distance is expressed as a product of the number of collisions and the mean free path of sputtered particles. Thus the distance depends on i) sputtering gas pressure, ii) mass of sputtered particles and sputtering gas atoms, and iii) initial energy of sputtered particles. For example, as the sputtering gas pressure increases, the thermalization distance of sputtered particles is decreased by an increase of collision.

The thermalization distance of sputtered particles was calculated by Westwood using argon gas as the sputtering medium.[19] The thermalization distance of Ba or Ti atoms is approximately 40 to 60 cm at a gas pressure of 0.1 Pa, even though there is some difference between the values for Ba and Ti. However, the distance is reduced to less than 1 cm at a gas pressure of 4.0 Pa, which is the maximum pressure of this study. Since the target-substrate distance is fixed at 5 cm in this study, it can be expected that most of the sputtered particles lose their initial energy before reaching the substrate at the gas pressure of 4.0 Pa. On the other hand, the particles sputtered at a lower gas pressure are expected to arrive at the substrate without significant energy loss.

Westwood[19] and Somekh[20] reported that the energy of sputtered particles is related to the mass of sputtering gas and sputtered atoms. They concluded that the energy loss of the sputtered particles increases with increase of the mass of sputtering gas atoms. Therefore, in our case, it can be expected that the sputtered particles lose their energy to a great extent with increasing argon content in the sputtering gas because argon is heavier than oxygen. Moreover, since the sputtering yield of argon is high compared with that of oxygen, the increase of argon content may result in the increase of sputtered atoms which are heavier than gas atoms in the chamber. Consequently, the sputtered particles

lose their initial energy faster by the collisions with previously sputtered ones as the argon content increases.

4.2 Thermal vibration and deposition profile

The thermal vibration model is suggested as one possible mechanism to understand the deposition profiles of sputtered $BaTiO_3$ thin films. such as preferred orientation, crystallization and lattice constant. This model is based on the thermal vibration of sputtered particles.

Since the perovskite $BaTiO_3$ has an ionic component of 82% for the barium-oxygen bond and of 63% for the titanium-oxygen bond.[21,22] the relationship between the binding energy and the mean interionic distance of component atoms can be expressed as shown in Fig. 8. When the sputtered particles are deposited with lower energy, E_1, the thermal vibration is weak, and the lattice is formed with a mean interionic distance X_1, because the atoms thermally vibrating are deposited and quenched on the substrate. On the contrary, as the energy of sputtered particles increases to E_2, the thermal vibration becomes intense and the anharmonicity will cause the increase of the mean interionic distance from X_1 to X_2. The variation of the lattice constant with gas pressure in Fig. 4 can be explained in this manner. When the particles sputtered at a low gas pressure arrive at the substrate, they will form a lattice having a larger lattice constant due to intense thermal vibration. However, if the thermal vibration becomes too intense, it becomes difficult to form a normal lattice and this leads to amorphous films (e.g., argon content less than 10%) as shown in Fig. 2. It is considered that the energy of sputtered particles also affects the crystallization and the growth of crystallites as shown in Figs. 1 and 7. The energy of sputtered particles probably promotes the crystallization and the growth of crystallites.

In the $BaTiO_3$ perovskite structure. the (111) plane has the highest packing density and is thermodynamically the most stable plane among the crystal planes with low Miller indices. Thus it is easy for the low-energy particles vibrating weakly to grow along the (111) plane, which is consistent with the grain growth
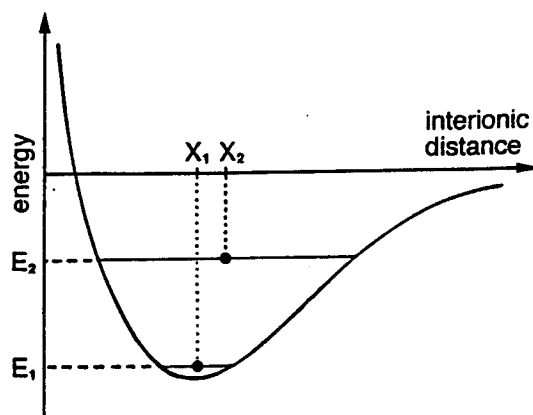

Fig. 8. Schematic diagram of the relationship between the energy of sputtered particles and the interionic distance.

in donor-doped BaTiO$_3$.[19] The appearance of the (111) peak at a high argon content (in Fig. 2) can be explained by this reason. However. the appearance of the (110) peak at a high gas pressure cannot be explained by the occupation density because the (110) plane has lower occupation density than (100) plane. It may be important to note that the (110) plane is a unique plane which has Ti–O bonding among the crystal planes with low indices; this plane will be thermodynamically more stable than the (100) plane. Although the deposition methods are different from each other, Nagatomo *et al.*[5] and Lee and Park[6] have also reported the preferential orientation of the (101) plane in BaTiO$_3$ thin films for rf-sputtering and sol-gel techniques. On the other hand, when the thermal vibration becomes intense with high energy, it may prevent the particles from aligning along the highest occupation density plane. That is, it is easier for the particles vibrating intensely to grow along a relatively lower occupation density plane, i.e., the (100) plane.

5. Conclusions

Oriented BaTiO$_3$ thin films were sputtered onto the amorphous fused quartz substrate without any post-annealing process. It was confirmed that the preferentially oriented thin films could be prepared at a substrate temperature as low as 300°C. The preferred crystal orientation of the films was changed systematically with sputtering gas pressure, gas composition and substrate temperature. As the energy of the sputtered particles increases, the (100) orientation is preferred over the (110) or (111) orientation, and the lattice constant increases. The thermal vibration due to the energy of the sputtered particles is considered as the origin of change in deposition profile, and the energy of the sput-

tered particles promotes the crystallization and the growth of crystallite.

1) K. Torii. T. Kaga. K. Kushida, H. Takeuchi and E. Takeda: Jpn. J. Appl. Phys. **30** (1991) 3562.
2) R. Takayama, Y. Tomita, K. Iijima and I. Ueda: J. Appl. Phys. **61** (1987) 411.
3) E. Yamaka, H. Watanabe, H. Kimura, H. Kanaya and H. Ohkuma: J. Vac. Sci. & Technol. A **6** (1988) 2921.
4) V. S. Dharmadhikari and W. W. Grannemann: J. Appl. Phys. **53** (1982) 8988.
5) T. Nagatomo. T. Kosaka, S. Omori and O. Omoto: Ferroelectrics **37** (1981) 681.
6) C. H. Lee and S. J. Park: J. Mater. Sci., Mater. Electron. **1** (1990) 219.
7) T. Katayama. M. Fujimoto. M. Shimizu and T. Shiosaki: Jpn. J. Appl. Phys. **30** (1991) 2189.
8) K. Iijima, T. Terashima, K. Yamamoto, K. Hirata and Y. Bando: Appl. Phys. Lett. **56** (1990) 527.
9) J. Kang, T. Yuko and S. Sakka: Jpn. J. Appl. Phys. **30** (1991) 2182.
10) M. G. Norton, K. P. B. Cracknell and C. B. Carter: J. Am. Ceram. Soc. **75** (1992) 1999.
11) B. D. Cullity: *Elements of X-ray Diffraction* (Addison-Wesley. Reading, 1978) 2nd ed., p. 102.
12) T. Nagatomo and O. Omoto: *6th Meet. Ferroelectric Materials and Their Applications*, Jpn. J. Appl. Phys. **26** (1987) Suppl. 26-2, p. 11.
13) H. Schäfer: Ferroelectrics **22** (1978) 775.
14) J. A. Thornton: J. Vac. Sci. & Technol. A **4** (1986) 3059.
15) G. Este, R. Surridge and W. D. Westwood: J. Vac. Sci. & Technol. A **4** (1986) 989.
16) G. Este and W. D. Westwood: J. Vac. Sci. & Technol. A **5** (1987) 1892.
17) A. Gras-Marti and J. A. Valles-Abarca: J. Appl. Phys. **54** (1983) 1071.
18) A. R. Nyaiesh: Vacuum **36** (1986) 307.
19) W. D. Westwood: J. Vac. Sci. & Technol. **15** (1978) 1.
20) R. E. Somekh: J. Vac. Sci. & Technol. A **2** (1984) 1285.
21) M. Drofenik: J. Am. Ceram. Soc. **76** (1993) 123.
22) H. Thomann: Ferroelectrics **73** (1987) 183.

GRADUATING STUDENTS IN THE PROGRAM

APPENDIX 69

The Pennsylvania State University

The Graduate School

FLEXTENSIONAL
"MOONIE AND CYMBAL" ACTUATORS

A Thesis in

Materials Program

By
Aydin Dogan

Submitted in Partial Fulfillment

of the Requirements

for the Degree of

Doctor of Philosophy

December 1994

ABSTRACT

The flextensional composite moonie transducer was invented by Xu and Newnham in 1989. The moonie transducer can be used as hydrophone, transceiver, or actuator. The moonie transducer consists of a piezoelectric or electrostrictive ceramic disc (either in single layer or multilayer form) sandwiched between two metal endcaps, each having a crescent shaped cavity on its inner surface. These metal endcaps serve as a mechanical transformer for converting and amplifying the lateral displacement of the ceramic into an axial motion of the endcaps. Both the d_{33} and d_{31} piezoelectric coefficients contribute to the axial displacement of the composite.

There are two common types of solid state ceramic actuator designs: multilayer ceramic actuators and cantilever bimorph actuators. Multilayer ceramic actuators exhibit large generative force (> 3000 N), but their displacement values are low (around 10 μm). Cantilever bimorph actuators produce large displacement (> 100 μm), but their generative force are low (around 0.5 N). The moonie actuator can fill the gap between the two common types of actuator design.

The aim of the present work was to investigate the actuator characteristics of the moonie transducer. Important actuator properties including displacement, generative force, and response time were used to characterize the moonie actuator. An intensive investigation of the cavity size of the endcaps was carried out to understand their effect on the actuator characteristics of the moonie. Displacement increases exponentially with increasing cavity diameter and increases linearly with increasing cavity depth. Displacement is inversely proportional to the endcap thickness. For the dimensions evaluated in this study, it was found that a maximum displacement of 22 μm can be achieved with 0.3 mm thick endcaps at 1.0 kV/mm. Using the multilayer ceramic in the moonie design, the applied voltage was decreased to 100 V, even though the applied field was constant at 1.0 kV/mm. Higher displacement values were obtained by stacking the

multilayer moonie actuators together (for 5 layers the displacement was around 105 μm at 100 V). The maximum generative force of the moonie actuator with a 0.3 mm brass endcap thickness was around 3 N at the center of the sample. Displacement and generative force show a position dependent behavior. The fastest response time of the moonie actuator varies between 5-50 μsec depending on the cavity size.

As a part of this thesis a new endcap was developed. The new flextensional actuator was called the "Cymbal". The cavity of the cymbal endcap has a truncated conical shape. A punch and die were designed to fabricate identical endcaps with minimal cost. Cymbal actuators show higher displacement values of about 40 μm, with less position-dependent behavior. They also have higher generative forces (15 N) due to the enlarged active surface, and reduced metal content.

The reliability of the moonie actuator depends on the mechanical, electrical and chemical stability of the bonding layer. The characteristics of the bonding layer of the moonie actuator were tested with destructive (peel-up), and nondestructive (Scanning Acoustic Microscopy and resonance spectrum) techniques. Eccobond-45 was selected as the bonding agent. Fatigue tests of multilayer moonie actuators were performed under a cyclic electric field 1 kV/mm with a triangular wave form at 100 Hz at room temperature. Deviations of less than ± 0.1 % from the original displacement value were observed for up to 10^7 cycles. Maximum deviations in the displacement of ± 15 % from the room temperature value were observed in the range -20 to +70 °C.

Outstanding actuator properties can easily be achieved with flextensional moonie and cymbal designs by changing the cavity size, endcap thickness, and endcap material. With its unique design, moonie actuators cover a wide performance range between multilayer and bimorph actuators.

APPENDIX 70

The Pennsylvania State University

The Graduate School

ELECTROMECHANICAL EFFECTS IN POLYMERIC MATERIALS

A Thesis in

Materials

by

Hong Wang

Submitted in Partial Fulfillment
of the Requirements
for the Degree of

Doctor of Philosophy

August 1994

ABSTRACT

Electromechanical coupling effects such as piezoelectricity and electrostriction have been widely applied in transducers and sensors. Conventional transducer materials include ceramics such as lead zirconate titanate (PZT) and lead magnesium niobate-lead titanate (PMN-PT) and single crystals such as quartz. During the last two decades, electromechanical polymers have drawn much attention because they have high mechanical flexibility, low acoustic impedance, and can be easily molded into desirable shapes. Piezoelectric polyvinylidene fluoride (PVDF) and its copolymer with trifluoroethylene (TrFE) and trtrafluoroethylene (TFE) have already been used in various transducers. The recently discovered large electric-field-induced strains of polyurethane elastomers manifest the potential utilization of the materials in transducers and sensors. However, compared with electromechanical ceramics, the property characterization and basic understanding of electromechanical polymers are far from complete. The purposes of this research are to carry out a comprehensive investigation of the electromechanical properties of a P(VDF-TrFE) (75/25) copolymer and polyurethane elastomers and to obtain a better understanding of the mechanisms of electromechanical effects of these materials. The main results of this research are of great significance in the smart materials engineering and molecular modeling of these materials.

For P(VDF-TrFE) (75/25) copolymer, all matrix elements of complex piezoelectric strain coefficient, dielectric constant under constant stress, and elastic compliance under constant electric field have been measured. All other coefficients in the constitutive equations of piezoelectricity have been calculated based on the measured properties. The temperature and frequency dependencies of each of the complex piezoelectric d coefficients and complex dielectric constants have been measured. These results, as the most complete experimental data set currently available for any PVDF and

its copolymers, provide a wealth of information for device designing in applications and for theoretical modeling in basic understanding of the materials.

A high-sensitivity, phase-sensitive d_{33} meter, which is suitable for the routine measurement of complex d_{33} constant, has been developed during this research work. The setup together with the laser interferometer in this laboratory provides a unique facility for characterizing complex d constants of piezoelectric materials.

The studies of dielectric and piezoelectric relaxation are important in the understanding of property-structure relationships of materials. The experimental results of this research reveal that piezoelectric relaxation also occurs near the glass transition of the P(VDF-TrFE) copolymer, but the relaxation temperature is different from that of the dielectric constants. A two-phase-composite-structure model, in which the interaction between crystalline and amorphous regions was taken into account, has been developed to explain the experimental results. The expressions of the effective dielectric constant, piezoelectric d constant from the direct and the converse effect and elastic compliance were derived as functions of the properties of the constituent phases. The numerical calculations of these properties indicate that the amorphous phase in PVDF and its copolymer plays an important role in the piezoelectric response of the materials, and different relaxation frequencies (or temperatures) of piezoelectric and dielectric constants are caused by the interaction between the crystalline and amorphous regions. The results of this model can be also applied to a 0-3 ceramic/polymer composite structure.

As one of the applications, PVDF and its copolymers can be used as hydrophone materials. The improvement of the hydrostatic properties by mechanical clamping, such as piezoelectric constants g_h and figure of merit $d_h g_h$, was studied experimentally. The results are in good agreement with the theoretical calculations.

For soft polyurethane elastomers, the strain coefficients including both longitudinal and transverse constants were precisely determined from single layer, free-

standing film samples. A strain level of 2.2% was achieved for cast samples under a driving field 490 kV/cm. The induced d_{33} constant is -890 pC/N under the same level of bias field. The dielectric and elastic properties were also studied. The results of hydrostatic measurements indicate that the electrostriction contribution is less than 2% of the total strain response. Therefore, it is concluded that Maxwell stress effect is one of the major contributions to the field induced strain response of the materials. It is also found that non uniformity exists in these materials, which greatly enhances the strain response.

APPENDIX 71

The Pennsylvania State University

The Graduate School

SMART CERAMIC-METAL COMPOSITES
for
ACTIVE VIBRATION CONTROL

A Thesis in

Ceramic Science

by

James F. Tressler

Submitted in Partial Fulfillment
of the Requirements
for the Degree of

Master of Science

December 1993

ABSTRACT

The ceramic-metal composite actuator, or "moonie", has been successfully modified in design so as to integrate both sensing and actuating functions into a single device. The prototype design consists of a thin (0.1mm) piezoceramic sensor imbedded within the surface of a standard 3mm thick, 11mm diameter moonie actuator. This "smart" composite, in combination with a simple feedback circuit, was used to actively control low-level sinusoidal external vibrations coming from a multilayer actuator with known vibration frequency and amplitude. The sensor/actuator/feedback system is capable of detecting and suppressing in real time small (<1µm) vibration displacements with low (<100gf) forces. The dynamic frequency range of this device ranges from 100Hz to about 6000Hz.

It is also shown that by replacing the piezoceramic in the actuator with an electrostrictive ceramic (PMN-PT), the sensitivity of the sensor can be tuned by changing the applied bias field.